Thesis

Void Cosmology in the SKA Era

SKA時代のボイド宇宙論

Takao ENDO

Graduate School of Science
Division of Particle and Astrophysical Science
Nagoya University

Contents

Abstract

We investigate the possibility to apply the cosmic voids properties to evaluate the cosmological models. Cosmic voids are defined as low matter density regions, such that they seem to be affected by the nature of the dark energy which accelerates the expansion of the universe. Even though the ΛCDM model is regarded as a standard model in which dark energy is considered to be a cosmological constant that is characterized by the equation of state parameter, w, corresponding to -1, there would be some possibilities that dark energy is not the cosmological constant. If $w = -1$, the energy density of dark energy varies as time passed, and could be possible to have inhomogeneities. In order to probe the clustering nature of dark energy, we parameterized its speed of sound and equation of state. Using the spherical model and excursion set approach for the void abundance, we find that even though the clustering of dark energy affects each void formation by sub percent level, the abundance of voids is modified significantly when there is a dark energy clustering.

We also investigate the application of void shapes to distinguish the energy density or the equation of state of dark energy. The Alcock-Paczynski test is an evolution model-free cosmological test and it demands only the isotropy of observed objects. The Alcock-Paczynski test has been applied to averaged shapes of voids found in the galaxy surveys, but the constraint on the cosmological parameters are not tight enough. The reason is the insufficient number of void samples so that the shape noise is significant. In order to obtain a lot of voids, we try to identify voids in the future HI intensity mapping surveys, in which we trace the large scale matter distribution based on the emissions from the neutral hydrogen atoms. We also expand our strategy to conduct the Alcock-Paczynski test with averaged shapes of voids into the averaged shapes of intensity contour which surrounds void regions. We analyze the result of the state of the art cosmological magnetohydrodynamic simulation, IllstrisTNG, in order to simulate the 21cm signal map. We produce particle distributions based on the 21cm intensity fields to find voids by using the VIDE code which estimates the density field based on the Voronoi tessellation and identifies voids by the watershed method. The shape of the stacked void in the 21cm field is flattened along the line of sight due to the peculiar velocities in redshift-space although it is spherical without the effect of the peculiar velocities. The shape distortion seems to be independent of the redshift and void sizes so that we estimate the preferable cosmological parameters by the Markov chain Monte Carlo methods. We find that the estimations of matter density parameter and equation of state parameter of dark energy are biased by the effect of the peculiar velocities. However, we can estimate these parameters with a few percent accuracies only by the test if we can remove the effect properly.

Chapter 1

Introduction

1.1 Large Scale Structure of the Universe

The large-scale matter distribution provides us much insight into the Universe. In 1926, Hubble pointed out that the distribution of galaxies is close to being homogeneous (Hubble, 1926). The general relativity theory with the isotropic and uniform matter distribution has a solution that the Universe would expand. The expansion of the Universe yields the galaxy redshifts and that is confirmed by Lemaître in 1927 and Hubble in 1929 (Hubble, 1929) independently. After that, people considered that the matter uniformly distributes in the universe and this idea had not changed for some decades.

The turning point was in the 1960s. Zwicky, as well as Shane and Wirtanen, observed the galaxy distribution on the sky and their catalogs showed the different forms of distribution from the uniform one. One of which was mapped on the celestial sphere by Seldner et al. (1977) and we show it in Figure 1.1. From this figure, one can see the evidence of the inhomogeneous distribution of the galaxies.

Even though their galaxy catalogs had only 2-dimensional information on the sky, namely only the angular positions, the two-point analysis of the catalog such as Totsuji & Kihara (1969) or Groth & Peebles (1977) indicated the inhomogeneity in the galaxy distribution because the two-point angular correlation function shows a power law which can never be seen in the random distribution. In order to ensure the inhomogeneity of the matter distribution, it is necessary to get the 3-dimensional distribution of galaxies. The location of galaxies along the line of sight is determined by the cosmological redshift of their spectrum. For example, the distance can be obtained by the Hubble-Lemaître law $cz = H_0 r$ for relatively nearby galaxies. For highly redshifted galaxies, the relation is different due to the expansion of the Universe. Although it was needed to observe the galaxy distribution in the 3-dimensional survey, it took a significant time to measure the spectrum of galaxies in those days.

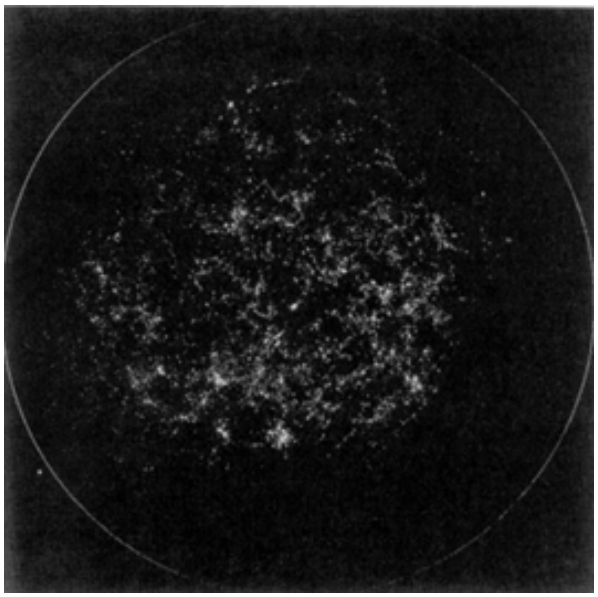

Figure 1.1: The map of the galaxy distribution of the Shane and Wirtanen's galaxy catalogs made by Seldner et al. (1977) Even though the position of the galaxies are only two dimensional, we can see the inhomogeneity in the galaxy distribution.

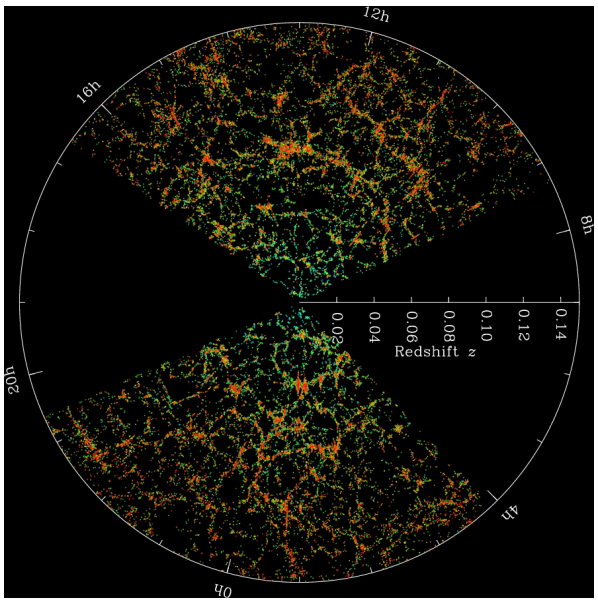

Figure 1.2: The three dimensional galaxy distribution observed by the SDSS. The observer locates at the center of the map and the radial coordinate corresponds to the distance to the galaxies. Filaments, clusters of galaxies and voids are seen. This Figure is credited to "www.sdss.org".

In the 1970s, the galaxy redshift survey was promoted by the appearance of the image intensifier in the astronomical field. One of the early redshift surveys was conducted by Gregory & Thompson (1978) and they found that there are large empty regions in the nearby Universe, so-called "*cosmic voids*". In the same period, Jõeveer et al. (1978) observed a different region and reached the same finding. However, at that time, because of the immatureness in the survey technology, it was ambiguous whether voids really exist or not.

Several years later, the redshift survey conducted at the Center for Astrophysics in the U.S.A. revealed that such large empty regions are surely located in the Universe (de Lapparent et al., 1986; Geller et al., 1987). In the survey, the distribution of galaxies over 100 Mpc/h scales was illustrated and then, we have recognized that galaxies form filament or wall structures and voids locate surrounded by these galaxies, which is called the "*cosmic web*". After the CfA survey and with a development of the observational instruments, larger-scale surveys have been conducted (Colless, 1998; York et al., 2000; Dawson et al., 2013) and we can see the rich structures of the Universe (see Figure 1.2).

1.2 Revealing accelerating expansion

While Hubble had revealed that the Universe is expanding, it was not unclear how the Universe expands. While the deep surveys of the Universe have revealed the structure of the matter distribution, they have also revealed the existence of a mysterious substance in the Universe has come to light, so-called dark energy. In the 1990s, two groups initiated to open the expansion history of the universe by observing the recession velocities of the distant type Ia supernovae (Riess et al., 1998; Perlmutter et al., 1999). Both groups have reached the same answer that our Universe acceleratingly expands (see Figure 1.3), which indicates that there is a mechanism to vanish the gravity on large scales. Even now, the type Ia supernovae show the evidence of the acceleration without combining other observations (Scolnic et al., 2018). The accelerating expansion of the Universe can be satisfied by introducing a substance which has a negative pressure into the right-hand side of the Einstein equation with the isotropic and homogeneous universe. Historically, the cosmological constant is one of the candidates for the unknown energy which was originally introduced to keep the dynamics of the universe stable. As described in the next chapter, the candidates for causing the accelerating expansion are not only the cosmological constant but also any energy fluid with the equation of state parameter less than negative one-third. In general, such energy is called "*dark energy*".

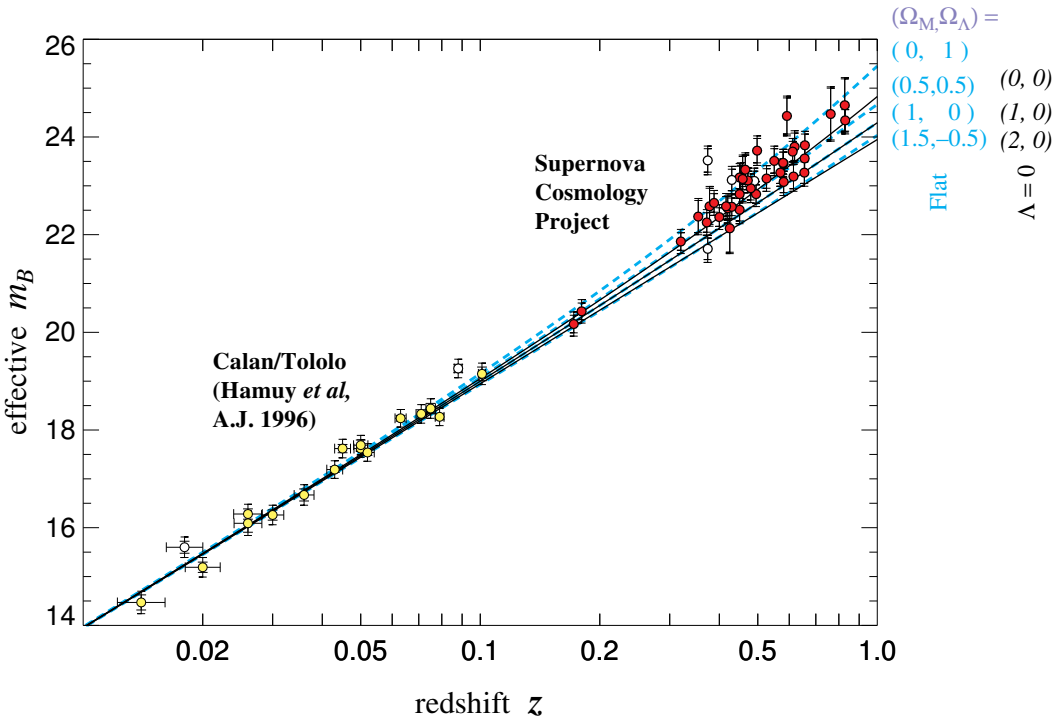

Figure 1.3: The obsevational evidence of dark energy. It is seen that the universe including a cosmological constant explain the data points rather than matter dominant universe. This figure is from Perlmutter et al. (1999).

1.3 Observational probe of Dark Energy

Although we have known that there is a surely unknown substance which accelerates the expansion of the Universe, we have not identified itself. It is difficult to find out dark energy itself since it has not been directly observed and then, a significant number of dark energy models have been proposed (Yoo & Watanabe, 2012). Then what we can do is to constrain the nature of dark energy through observations. The nature of dark energy can be traced by the geometry or the expansion history of the Universe since its energy budget and equation of state affect the time evolution of the Universe. Otherwise, we can trace its nature by observing the growth of large scale structures in the Universe since the accelerating expansion suppresses the growth rate (see Capter 2.2.2). So far many observational probes have been proposed (Weinberg et al., 2013). Here we would like to introduce some representative observational targets.

Cosmic Microwave Background

The anisotropy in the Cosmic Microwave Background radiation (CMB) includes much cosmological information (Hu & Sugiyama, 1996; Bennett et al., 2003; Komatsu et al., 2011; Planck Collaboration et al., 2018). The effect of the accelerated expansion appears at large scales through the late-time Integrated Sachs-Wolfe (ISW) effect (Sachs & Wolfe, 1967). This effect is caused by the time evolution of the gravitational potential at cosmological scales. In other words, the CMB photons obtain more energy when they come into a gravitational potential than they spend to it to escape the potential (this is the case that they come into high-density region, but go through low-density region, they lose more energy after passing the regions) because the accelerating expansion reduces the amplitude of the potential. Since this effect is particular at very large scales such that the effect causes modification of the CMB angular power spectrum at low l sides. However, at those scales, the cosmic variance is large, so that using only the CMB power spectrum provides a weak constraint on the dark energy property.

Baryon Acoustic Oscilation

Until $z \sim 1100$, the typical energy of the CMB photons are enough to ionize hydrogen atoms and they exist as plasmas. The CMB photons interact electrons through inverse Compton scattering and the electrons are connected with protons by the electromagnetic force. So, those photons and baryonic particles were as a mixed fluid. After the matter and radiation energy equality at $z \sim 3000$, dark matter begins to cluster based on the density fluctuation. The photons and baryonic matter fluid also attempt to get into the gravitational potential of dark matter by the gravitational interaction between dark matter and baryons, but the

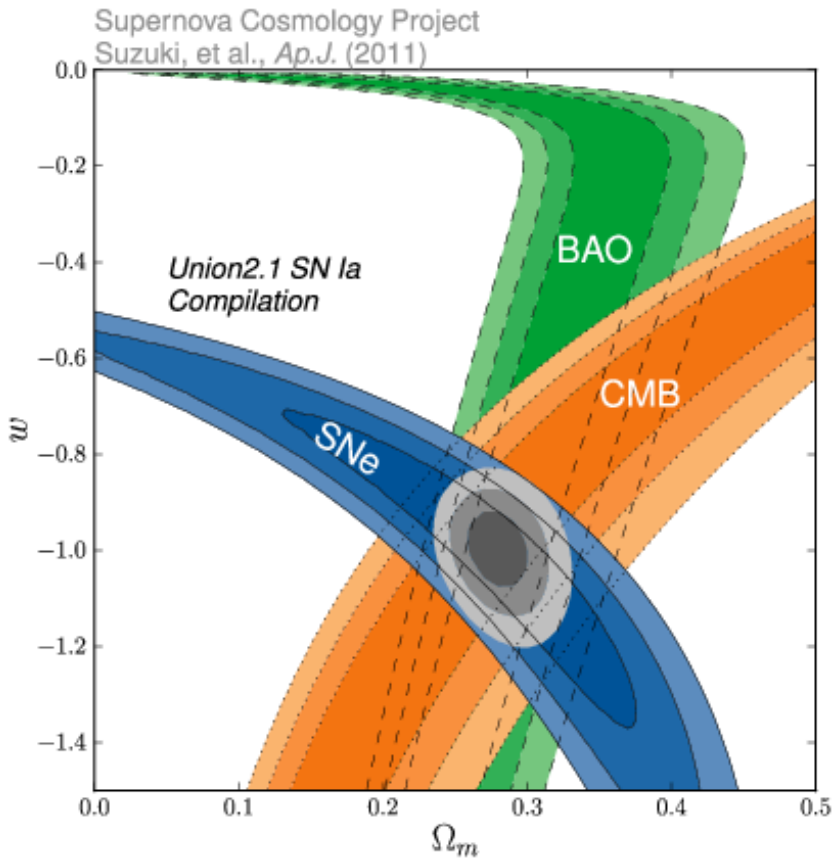

Figure 1.4: The constraint on the nature of dark energy and matter density in the Universe. This figure shows that a cosmological constant is a preferable model of dark energy. This figure is from Suzuki et al. (2012)

clustering of the baryonic matter rebounds due to the radiation pressure of the photons. Until the recombination, the fluctuation caused by the rebound propagates and recorded in the matter density when the CMB photons and baryons were decoupled. This is called the Baryon acoustic oscillation.

This fluctuation is observed in the CMB angular power spectrum (Hu & Sugiyama, 1996; Eisenstein & Hu, 1998), and do not change its scale after the recombination, so that it can be utilized as a standard ruler to measure the cosmological distance. In fact, the oscillation scale is detected in the galaxy distribution (Eisenstein et al., 2005) and provide the cosmological constraint (Suzuki et al., 2012) (see Figure 1.4).

Cluster abundance

The abundance of astronomical objects with a specific mass range provides us with information about the structure growth, which is related to the time evolution of density perturbations. The abundance of the massive objects is called the mass function and beginning with the Press-Schechter mass function (Press & Schechter, 1974), several mass functions have been proposed (Sheth & Tormen, 2002; Tinker et al., 2008) and utilized to get the information of the Universe. In general, however, it is quite difficult to model the evolution of the high-density object, so that the estimation of our cosmology from the cluster abundance is very model-dependent.

Cosmic voids

In recent years, the wide and deep redshift survey of galaxies enables us to distinguish the large scale structures. Among them, the formation of cosmic voids is expected to reveal the nature of dark energy because they contain fewer matter components inside the region (Gregory & Thompson, 1978). They are expected to be a clean object to see the effect of dark energy on the formation of them. For example, the dynamical evolution of their shapes are sensitive to the nature of dark energy, especially the equation of state (Park & Lee, 2007; Lavaux & Wandelt, 2010; Biswas et al., 2010; Bos et al., 2012). Also, the low-density might lead to the fact that they are relatively easily modeled because of the amplitude of the density fluctuation, their growth would be linear or semi-linear regime. For this property, some studies have tried to obtain cosmological information from its dynamics (Hamaus et al., 2016).

Even though voids are expected to be the probe of the Universe, it still seems difficult to fully utilize the void property to constrain the cosmological model because they are relatively larger structures than the clusters, such that the statistical samples are less. However, such a situation can be improved by more large scale surveys. Even now, the alternative way to trace the matter distribution is under construction. Thus we are now in the era to investigate the Universe through voids.

1.4 Purpose of this Thesis

To evaluate the cosmological model precisely, one needs it is important to examine the model in terms of many aspects. In this thesis, we are going to investigate the possibility of the application of cosmic voids to the model evaluation in cosmology, especially some nature of dark energy such as its equation of state, energy budget, and spatial perturbation. To achieve this purpose, we provide a basic formalism to describe the evolution of our Universe itself and structure formations in the Universe in section chapter 2.

In the next chapter, we are going to investigate the effect of dark energy perturbations on the void formations. Some previous studies try to see the effect of dark energy perturbation of the void formation, especially focusing on the void density profile. On the other hand, what we will see is the effect on the void size. We provide the equation of density perturbation of dark energy inside a spherical void and examine how much the perturbation of dark energy enhances or suppresses the size evolution of individual voids. Then we focus on the effect of the dark energy perturbation on the statistical property of the void size, namely the size abundance. We use the void size function derived in the next chapter to see the effect.

In the latter part of this thesis, we are going to investigate the application of the void shape to evaluate the cosmological parameters. The method is called the Alcock-Paczynski (AP) test, which is an evolution free method to constrain the cosmological model demanding only isotropic objects. The concept of the AP test with cosmic voids was proposed by Ryden (1995) for the first time and sophisticated by Lavaux & Wandelt (2012). The application of voids to the Alcock-Paczynski test has been conducted in the galaxy surveys (Sutter et al., 2012a, 2014; Mao et al., 2017a). However, voids in the conventional galaxy surveys have a large shape noise due to the insufficient number of void samples. Thus we need more void samples in order to reduce the shape noise.

To obtain a huge number of void samples, we consider identifying cosmic voids in the HI intensity mapping survey. An international radio telescope project, called the Square Kilometre Array (SKA) has been ongoing, in which we survey the emission from the neutral hydrogen (HI) atom along with the large scale structures. By this survey, we will observe much more volume of the Universe than the conventional galaxy surveys (Santos et al., 2015; Square Kilometre Array Cosmology Science Working Group et al., 2018). From this point of view, HI intensity mapping survey seems to have a huge potential to provide a lot of void samples.

In chapter 4, we review the HI signal and introduce some aspects of the SKA experiments. In chapter 5, we introduce our procedure to make a mock intensity map from the IllustrisTNG simulation data (Nelson et al., 2019) and how we identify the void structure in the intensity map. Then we conduct the AP test by using the average shape of the voids in the HI intensity field and show how much precisely recover the fiducial cosmological parameters by our method as results.

Chapter 2

Standard Cosmological model

Observations such as Cosmic Microwave Background (CMB) or the galaxy distribution have suggested that our Universe is statistically homogenous and isotropic at very large scales. This is called the cosmological principle. On the other hand, for small scales, we can see a rich structures of the Universe such as stars, galaxies, and the large scale structures. Such structures are thought to be formed from tiny density fluctuations. Even though the fluctuations are very small, they have evolved by the gravitational instability. In order to quantitatively describe the evolution of the Universe and the structure formations, we introduce some fundamental equations form them in this chapter. We begin with the evolution of the Universe as a back ground at first, and then, we introduce the cosmological perturbation theory as a first oder perturbation. We also show an analytic model to describe the non-linear structure formations. At the end part of this chapter, we introduce some statistical values to evaluate the our models.

2.1 Background cosmology

Expansion of the Universe

The line-element of the 4 dimensional homogeneous and isotropic spacetime is called Friedmann-Lemaître-Robertson-Walker (FLRW) spacetime, which is described as

$$ds^2 = -dt^2 + a(t)^2 \left(\frac{dr^2}{1 - Kr^2} + r^2(d\theta^2 + \sin^2\theta d\phi^2) \right), \tag{2.1.1}$$

where $a(t)$ is a scale factor and K is a constant curvature which can be $1, -1$ and 0 that corresponds to close, open and flat universe respectively. From the Einstein equation

$$G^{\mu}{}_{\nu} = \frac{8\pi G}{c^4} T^{\mu}{}_{\nu} \tag{2.1.2}$$

with the perfect fluid,

$$T^{\mu}{}_{\nu} = (\rho + P) u^{\mu} u_{\nu} + P \delta^{\mu}{}_{\nu}, \tag{2.1.3}$$

we will obtain two independent equations,

$$\left(\frac{\dot{a}}{a}\right)^2 = \frac{8\pi G}{3c^2}\rho - \frac{c^2 K}{a^2}, \tag{2.1.4}$$

$$\frac{\ddot{a}}{a} = -\frac{4\pi G}{3c^2}(\rho + 3P), \tag{2.1.5}$$

where ρ is the total energy density of substances in the Universe including radiation, matter, dark energy and so on, These are equations which describe the expansion of the universe and we often write $H(a) = \dot{a}/a$ on the left hand side of equation (2.1.4). Combining the above equations, we obtain the equation of energy conservation,

$$\dot{\rho} + 3\frac{\dot{a}}{a}(\rho + P) = 0. \tag{2.1.6}$$

By defining the density parameters as

$$\Omega = \frac{8\pi G\rho}{3H^2}, \quad \Omega_K = -\frac{K}{(aH)^2}, \tag{2.1.7}$$

we can write equation (2.1.4) as

$$\Omega + \Omega_K = 1 \tag{2.1.8}$$

The energy components ρ in the Universe are roughly divided into "radiation", "matter" and "dark energy",

$$\rho = \rho_{\mathrm{r}} + \rho_{\mathrm{m}} + \rho_{\mathrm{de}}, \tag{2.1.9}$$

and we can define the density parameters for them like above respectively,

$$\Omega_{\rm r} = \frac{8\pi G\rho_{\rm r}}{3H^2}, \quad \Omega_{\rm m} = \frac{8\pi G\rho_{\rm m}}{3H^2}, \quad \Omega_{\rm de} = \frac{8\pi G\rho_{\rm de}}{3H^2}. \tag{2.1.10}$$

The relation between energy density and pressure is described by the equation of state, here we parameterized it as

$$P = w\rho, \tag{2.1.11}$$

Time evolution of the energy density is obtained by solving conservation equation (2.1.6) as

$$\rho(t) = \rho_0 \exp\left[\int_{a_0}^{a(t)} (1 + w(a'))\frac{da'}{a'}\right]. \tag{2.1.12}$$

If w is constant, we can conduct the integration in the above equation and get

$$\rho(t) = \rho_0 a^{-3(1+w)}. \tag{2.1.13}$$

For radiation and matter, $w_r = 1/3$ and $w_m \sim 0$ respecttively. By using these expressions, we rewrite equation (2.1.4)

$$H^2(a) = H_0^2\left(\frac{\Omega_{\rm r}}{a^4} + \frac{\Omega_{\rm m}}{a^3} + \frac{\Omega_K}{a^2} + \frac{\Omega_{\rm de}}{a^{-3(1+w)}}\right). \tag{2.1.14}$$

From the equation (2.1.5), we can also derive the condition for dark energy dandidates. Since the expansion of the Universe is accelerating, the condition is satisfied if $\rho + 3P < 0$, which can be read as

$$w < -\frac{1}{3}. \tag{2.1.15}$$

This is the condition for the energy source that cause accelerating expansion. In cosmology, one of the goals is to constraint the w for dark energy. The current situation is consistent with $w = -1$ which leads to a cosmological constant since the energy density does not change along the time (see equation (2.1.13)).

The recent observations such as CMB anisotropy and the BAO and so on, indicate that the Universe is quite flat, $\Omega_K = 0.001 \pm 0.002$ and the cosmological constant is preferred

as a dark energy $w = -1.028 \pm 0.031$. When we stand on the ΛCDM model in which we consider cosmological constant Λ as dark energy and dark matter as a dominant matter component, the observations show that our Universe is dominated by the dark components as $\Omega_{\rm m} = 0.315 \pm 0.007$ and $\Omega_\Lambda = 0.689 \pm 0.006$ with $H_0 = 67.7 \pm 0.4$[km/s/Mpc] (Planck Collaboration et al., 2018).

Cosmological redshift

Since the Universe is expanding, the wavelength of light also expands from it is emitted until it reaches an observer. How much the wavelength is expanded is quantified as the redshift and it is described as

$$z = \frac{\lambda_o}{\lambda_e} - 1 = \frac{a_o}{a_e} - 1, \tag{2.1.16}$$

where subscription "o" and "e" mean the value at the time when it is observed and emitted respectively and we set the present epoch as $z = 0$.

Cosmological distances

The distance between an observer and an object will be different between when the light emitted from the object and when it reaches the observer because the Universe is expanding while the light is propagating. It is convenient to define the distance which does not change along with the time evolution. This is called the comoving distance, χ, and its infinitesimal displacement is given by

$$d\chi = \frac{dr}{\sqrt{1 - Kr^2}} \tag{2.1.17}$$

The integration of this equation results in

$$r = S_K(\chi) = \begin{cases} \dfrac{\sinh\left(\sqrt{-K}\chi\right)}{\sqrt{-K}} & (K < 0) \\ \chi & (K = 0) \\ \dfrac{\sin\left(\sqrt{K}\chi\right)}{\sqrt{K}} & (K > 0) \end{cases} \tag{2.1.18}$$

The light propagates to us satisfying $d\theta = d\phi = 0$ so that its geodesic satisfies

$$\frac{dt}{a(t)} = -\frac{dr}{\sqrt{1-Kr^2}}. \tag{2.1.19}$$

Therefore, comoving distance can be obtained as a function of redshift,

$$\chi = \int_t^{t_0} \frac{cdt'}{a(t')} = \int_0^z \frac{cdz'}{H(z')} \tag{2.1.20}$$

We also define the angular diameter distance d_A and luminosity distance d_L as

$$d_A = (1+z)^{-1} r(z), \tag{2.1.21}$$

$$d_L = (1+z) r(z). \tag{2.1.22}$$

2.2 Theory of Structure Formation

While our Universe seems homogeneous and isotropic at very large scale, we can see a lot of structures such as stars, galaxies, clusters of galaxies and voids. Such objects originate from very tiny density fluctuations which were exited at an early epoch and carved on the cosmic microwave background. In this section, we describe the evolution of the density fluctuation.

2.2.1 Cosmological perturbation theory

If the universe is perfectly homogeneous, there will be no structures in the future. However, our Universe is full of rich structures such as stars, galaxies, and large scale structures. These structures are regarded as results of the evolution of tiny matter density fluctuations at a very early epoch, and such fluctuations have been confirmed the CMB observation (Bennett et al., 2003).

Since the matter and space are connected through the Einstein equation (2.1.2), the evolution of the perturbations are also written by the equation.

Now, we assume the flat universe (ignoring the curvature K) and consider the perturbation theory in the conformal Newtonian gauge. The metric can be written as

$$ds^2 = -\left(1 + \frac{2\Phi}{c}\right) c^2 dt^2 + a^2 \left(1 + \frac{2\Psi}{c}\right) \delta_{ij} dx^i dx^j. \tag{2.2.1}$$

The Φ and Ψ represents the fluctuation in the time and space respectively.

We also consider the perturbation in a matter. We express the density and pressure with perturbations, and physical velocity as

$$\rho = \bar{\rho}(1+\delta), \quad P = \bar{P} + \delta P, \quad v_i = ac\frac{u^1}{u^0}, \tag{2.2.2}$$

respectively. The equations of the dynamics of the fluctuations are

$$3\frac{\dot{a}}{a}\left(\dot{\Psi} - \frac{\dot{a}}{a}\Phi\right) - \frac{c^2}{a^2}\Delta\Psi = 4\pi G\bar{\rho}\delta, \tag{2.2.3}$$

$$\left(\dot{\Psi} - \frac{\dot{a}}{a}\Phi\right)_{,i} = \frac{4\pi G}{c^2}(\bar{\rho} + P)av_i, \tag{2.2.4}$$

$$\left[\left(2\frac{\ddot{a}}{a} + \left(\frac{\dot{a}}{a}\right)^2\right)\Phi - \ddot{\Psi} - 3\frac{\dot{a}}{a}\Phi + \frac{c^2}{2a^2}\Delta(\Phi+\Psi)\right]\delta_{ij} - \frac{c^2}{2a^2}\left(\Phi+\Psi\right)_{,ij} = 4\pi G\delta P\delta_{ij}. \tag{2.2.5}$$

The trace and the other component of The equation (2.2.5) can be decomposed into the trace and the other components as

$$\left[\left(2\frac{\ddot{a}}{a} + \left(\frac{\dot{a}}{a}\right)^2\right)\Phi - \ddot{\Psi} - 3\frac{\dot{a}}{a}\Phi + \frac{c^2}{3a^2}\Delta(\Phi+\Psi)\right] = 4\pi G\delta P, \tag{2.2.6}$$

$$\left(\Phi+\Psi\right)_{,ij} = \frac{1}{3}\delta_{ij}\Delta\left(\Phi+\Psi\right). \tag{2.2.7}$$

For equation (2.2.7), $\left(\Phi+\Psi\right)_{,ij}$ equal zero when $i \neq j$, which indicate $\Phi + \Psi = 0$ because the universe should be homogeneous at very large scale which suggests the integration of

$(\Phi+\Psi)_{,ij}$ in terms of space should be zero. Therefore we obtain,

$$\frac{c^2}{a^2}\Delta\Phi - 3\frac{\dot{a}}{a}\left(\dot{\Phi}+\frac{\dot{a}}{a}\Phi\right) = 4\pi G\bar{\rho}\delta, \tag{2.2.8}$$

$$\dot{\Phi}+\frac{\dot{a}}{a}\Phi = \frac{4\pi G a}{c^2\dot{a}}\left(\bar{\rho}+\bar{P}\right)\psi, \tag{2.2.9}$$

$$\ddot{\Phi}+4\frac{\dot{a}}{a}\dot{\Phi}+\left(2\frac{\ddot{a}}{a}\frac{\dot{a}^2}{a^2}\right)\Phi = 4\pi G\delta P \tag{2.2.10}$$

where we redefine the velocity in terms of a velocity potential as

$$\boldsymbol{v} = -\frac{\nabla\psi}{aH}. \tag{2.2.11}$$

Combining equations (2.2.9) and (2.2.10) results in

$$\Delta\Phi = \frac{4\pi G a^2}{c}\bar{\rho}\left[\delta+\frac{3}{c^2}(1+w)\psi\right]. \tag{2.2.12}$$

This is the usual Poisson equation if the second term is lost. The second term is appearing when we consider a system in a relativistic context such as Hubble scale phenomenon. However, if we pay attention to the sub Hubble scale, the contribution from the velocity to the potential will be small. We will see this reason later.

The dynamics of the fluid is written by the continuity and Euler equations, which are obtained by the conservation law of the energy-momentum tensor,

$$T^{\mu}_{\nu;\mu} = 0. \tag{2.2.13}$$

The conservation law for the time and space components are then

$$-cT^{\mu}_{0;\mu} = \bar{\rho}\dot{\delta}+3\frac{\dot{a}}{a}(\delta P-\bar{P}\delta)+(\bar{\rho}+\bar{P})\left(\frac{1}{a}\nabla\cdot\boldsymbol{v}+\frac{3}{c^2}\dot{\Psi}\right) = 0 \tag{2.2.14}$$

$$\frac{c^2}{a}T^{\mu}_{i;\mu} = (\bar{\rho}+\bar{P})\left[\dot{v}_i+\frac{\dot{a}}{a}\left(1-3\frac{cs^2}{c^2}\right)v_i+\frac{c^2}{a}\frac{\partial\delta P}{(\bar{\rho}+\bar{P})}\frac{1}{a}\partial_i\Phi\right] = 0 \tag{2.2.15}$$

where we defined the speed of sound as

$$c_s^2 \equiv c^2 \frac{\dot{\bar{P}}}{\dot{\bar{\rho}}} = c^2 \frac{\delta P}{\bar{\rho}\delta}. \tag{2.2.16}$$

The second equation holds if the adiabatic condition is assumed. In this case, those equations are written

$$\dot{\delta} + 3\frac{\dot{a}}{a}\left(\frac{c_s^2}{c^2} - w\right)\delta + (1+w)\left(\frac{1}{a}\nabla\cdot\boldsymbol{v} + \frac{3}{c^2}\dot{\Psi}\right) = 0, \tag{2.2.17}$$

$$\dot{\boldsymbol{v}} + \frac{\dot{a}}{a}\left(1 - 3\frac{c_s^2}{c^2}\right)\boldsymbol{v} + \frac{c_s^2}{a}\frac{\nabla\delta}{(1+w)} + \frac{1}{a}\nabla\Phi = 0. \tag{2.2.18}$$

These above equations are the basis to describe the dynamics of the space-time. In the next part, we will see some aspects of the time evolution of these perturbations, especially for the non-relativistic matter.

Density evolution of non-relativistic matter

For the structure formation of the Universe, the role of the non-relativistic matter is important since if the velocities of the matter is close to the speed of light the matter is hardly gravitationally bounded, so that a lot of objects cannot be formed. Now we consider such non-relativistic matter evolution in the era in which the matter is a dominant component of the universe. We note that in our Universe, Cold Dark Matter which does not have interaction with the electromagnetic wave but has only the gravitational interaction and has a small velocity dispersion is a dominant ingredient of matter component. So, what we are considering is corresponding to the density evolution of the CDM. We assume the matter dominant era and a single fluid system in the subhorizon scale. For the above assumption we take the limit of $\dot{\Psi} \to 0, c_s \ll c, w = 0$ in equations (2.2.17) and (2.2.18), and then obtain

$$\dot{\delta} + \frac{1}{a}\theta = 0, \tag{2.2.19}$$

$$\frac{\partial\theta}{\partial t} + \frac{\dot{a}}{a}\theta + \frac{c_s^2}{a}\Delta\delta\frac{1}{a}\Delta\Phi = 0, \tag{2.2.20}$$

where we define $\theta \equiv \nabla \cdot \boldsymbol{v}$. By substituting θ of equation (2.2.19) into (2.2.20), we get the equation of motion of δ as

$$\ddot{\delta} + 2\frac{\dot{a}}{a}\dot{\delta} - \left(\frac{c_s^2}{a^2}\Delta\delta + \frac{1}{a^2}\Delta\Phi\right) = 0 \tag{2.2.21}$$

For the Newtonian limit, the potential satisfies the Poisson equation such that

$$\Delta\Phi = 4\pi G a^2 \bar{\varrho}\delta. \tag{2.2.22}$$

We note that this is a $\psi \to 0$ limit of equation (2.2.12) and $\bar{\varrho} = \bar{\rho}/c^2$ is the background mass density of matter.

Let us consider the qualitative discussion about the equation of motion of δ in Fourier-space. The equation is expressed as

$$\ddot{\tilde{\delta}} + 2\frac{\dot{a}}{a}\dot{\tilde{\delta}} - \left(4\pi G\varrho - \frac{c_s^2}{a^2}k^2\right)\tilde{\delta} = 0, \tag{2.2.23}$$

where "tilde" denotes that the valuable is a function in Fourier-space. The last term of the equation dominates the evolution of δ such that when $4\pi G\varrho - \frac{c_s^2}{a^2}k^2 > 0$, $\tilde{\delta}$ evolves while when $4\pi G\varrho - \frac{c_s^2}{a^2}k^2 < 0$, $\tilde{\delta}$ oscillationally decreases. In this condition, we derive the Jeans' wavenumber, and equivalently, the Jeans' length as

$$k_J = \frac{2\pi}{\lambda_J} = \frac{a\sqrt{4\pi G\bar{\varrho}}}{c_s}. \tag{2.2.24}$$

We note that these scales are defined in comoving scale. Thus, the condition for the evolution of perturbation can be in terms of the Jeans scale in other words, if the wavelength of the perturbation is larger than the Jeans length, such perturbation can evolve, while is the perturbation scale is smaller than the Jeans' length, such perturbation cannot grow.

Now we consider a further discussion of the growth of the density perturbation in the linear regime. The perturbations well enough large scale (at least larger than the Jeans scale) is written

$$\ddot{\tilde{\delta}} + 2\frac{\dot{a}}{a}\dot{\tilde{\delta}} - 4\pi G\varrho\tilde{\delta} = 0, \tag{2.2.25}$$

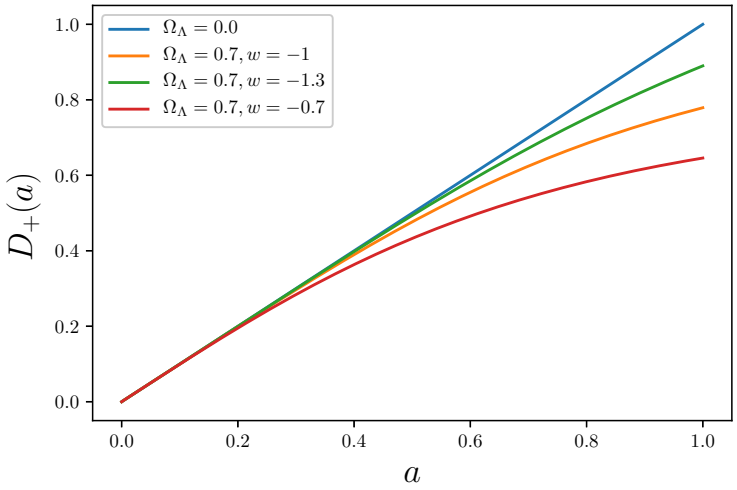

Figure 2.1: The time evolution of the linear growth factor with different cosmological parameters. Here we assume matter dominant universe, dark energy as a cosmological constant, dynamical dark energy model with equation of state parameter $w = -1.3$ and -0.7.

The solution of the equation can be written as

$$\tilde{\delta} = (D_+(a) + D_-(a))\tilde{\delta}_{\rm ini} \tag{2.2.26}$$

$$D_+(a) = \frac{5\Omega_{\rm m}H_0^2}{2}H(a)\int_0^a \frac{1}{a^3H^3}da \tag{2.2.27}$$

$$D_-(a) \propto H \tag{2.2.28}$$

where $D_+(a)$ and $D_-(a)$ are growing and diminishing solutions respectively. For the structure formation, the growing solution is important and $D_+(a)$ is called the linear growth factor. In Figure 2.1, we show the time evolution of the growth factor in different universe, which are matter dominant ($\Omega_{\rm de} = 0, \Omega_{\rm m} = 1$), dark energy as a cosmological constant ($\Omega_{\rm de} = 0.7, w = -1$), dynamical dark energy model with $w = -1.3$ and $w = -0.7$. We see that the matter dominant universe realizes the growth of the perturbation effectively. On the other hand, the accelerating expansion of the universe suppresses the evolution of perturbation, so that the growth factors deviate from the matter dominant universe. If w is less negative, the equality time between matter and dark energy becomes earlier such that the growth factor begins to be suppressed earlier.

2.2.2 Non-linear theory

In a very high-density region, it is difficult to analytically calculate the evolution of density fluctuation. However, based on using some assumptions, we can obtain some insights into the evolution of the high-density regions. Here we introduce the spherical collapse model. Let us consider a spherical mass shell with a physical radius of R. The dynamics of the mass shell is determined by the gravity caused by the matter which is inside the mass shell. The equation of motion of the radius of the mass shell is

$$\frac{d^2R}{dt^2} = -\frac{GM}{R^2}, \tag{2.2.29}$$

where M is the total mass within the mass shell, which is

$$M = \frac{4\pi}{3}R^3\varrho. \tag{2.2.30}$$

We assume that the amount of matter is conserved through the time evolution of the mass shell. Thus we have a conservation law of the matter,

$$M = \frac{4\pi}{3}\varrho R^3 = \frac{4\pi}{3}\varrho_{\rm ini}R_{\rm ini}^3 \tag{2.2.31}$$

where the subscription " ini" means the initial epoch. We decompose the mass density into the average matter density and the perturbation as

$$\varrho = \bar{\varrho}(1+\bar{\delta}), \tag{2.2.32}$$

where the matter fluctuation, $\bar{\delta}$, is the averaged fluctuation within the mass shell,

$$\bar{\delta}(R) = \frac{3}{4\pi R^3}\int_{|\boldsymbol{r}|<R} dr^3\delta(\boldsymbol{r}). \tag{2.2.33}$$

The equation (2.2.29) can be integrated over time and we obtain

$$\frac{1}{2}\left(\frac{dR}{dt}\right)^2 - \frac{1}{2}\left(\frac{dR}{dt}\right)^2_{t=t_{\rm ini}} = \frac{GM}{R} - \frac{GM}{R_i}. \tag{2.2.34}$$

Then, we assume that the initial velocity of the mass shell is approximated to the Hubble velocity such that

$$\frac{1}{2}\left(\frac{dR}{dt}\right)^2_{t=t_{\rm ini}} \approx \frac{1}{2}H^2_{\rm ini}R^2_{\rm ini} = \frac{4\pi G}{3}\bar{\varrho}_{\rm ini}R^2_{\rm ini}. \tag{2.2.35}$$

Thus the equation (2.2.34) is written as

$$\left(\frac{dR}{dt}\right)^2 - \frac{2GM}{R} = 2E \tag{2.2.36}$$

where $2E = 2G\bar{\varrho}_{\rm ini}R^2_{\rm ini}\delta_{\rm ini}$ is a constant value which is determined by the initial condition of the density fluctuation. The equation (2.2.36) can be solved by using a parameter Θ. When we consider a high dense region such that $\delta_{\rm ini} > 0$ or $K > 0$, the solutions of R and t are

$$\begin{cases} R = A(1-\cos\Theta), \\ t = B(\Theta - \sin\Theta). \end{cases} \tag{2.2.37}$$

On the other hand, if the spherical region is low dense at the initial epoch, $\delta_{\rm ini} < 0$ or $K < 0$,

$$\begin{cases} R = A(\cosh\Theta - 1), \\ t = B(\sinh\Theta - \Theta). \end{cases} \tag{2.2.38}$$

The coefficients, A and B have a relation

$$A = \frac{GM}{C}, \quad B = \frac{GM}{C^{3/2}}, \tag{2.2.39}$$

where we defined $C = |2E|$. In the matter dominant universe, the background density evolves as $\varrho = 1/6\pi G t^2$, so that the density contrast in the spherical region evolves as

$$\delta(t) = \frac{9(\Theta - \sin\Theta)^2}{2(1-\cos\Theta)^3} - 1 \tag{2.2.40}$$

for overdense region and

$$\delta(t) = \frac{9(\sinh\Theta - \Theta)^2}{2(\cosh\Theta - 1)^3} - 1 \tag{2.2.41}$$

For the linear regime, we can expand $\delta(t)$ with parameter θ and obtain

$$\delta_L(t) = \pm\frac{3}{20}\left(\frac{C^{3/2}}{GM}6t\right)^{2/3}, \tag{2.2.42}$$

where positive or negative signs are determined by whether the region is overdense or underdense, respectively.

For the gravitationally bounded objects, the evolution of R shows a maximum value at the turn around time $t = t_{\rm ta}$ and then the objects will collapse at $t = t_{\rm co}$. At those epoch,

$$t_{\rm ta} = \pi\frac{GM}{C^{3/2}}, \quad t_{\rm c} = 2t_{\rm ta}, \tag{2.2.43}$$

so that

$$R(t_{\rm ta}) = \frac{GM}{C}, \quad \delta(t_{\rm ta}) \sim 4.55, \quad \delta_L(t_{\rm ta}) \sim 1.06, \tag{2.2.44}$$

$$R(t_{\rm co}) = 0, \qquad \delta(t_{\rm ta}) = \infty, \qquad \delta_L(t_{\rm ta}) \sim 1.69. \tag{2.2.45}$$

For the gravitationally unbounded object, the radius continues to expand. As is the case of over-dense regions, we can define criteria for the structure formation of low dense regions in a little bit complex way as well. By comparing equations (2.2.38) and (2.2.39), the solutions can be expressed

$$\begin{cases} R = \dfrac{R_i}{2\epsilon}(\cosh\Theta - 1), \\ \dfrac{t}{t_i} = \dfrac{3}{4\epsilon^{3/2}}(\sinh\Theta - \Theta), \end{cases} \tag{2.2.46}$$

where $\epsilon = -\bar{\delta}_i > 0$. Let us consider a situation that the inner shell catches up the outer shell separated δR since the inner regions are more empty so that the expansion of the inner shell would be faster than the outer shell. The moment that the inner shell reaches the outer shell can be considered as the epoch that the formation of the underdense region goes into the

nonlinear stage, which can be considered as a formation of a void (Blumenthal et al., 1992). According to the equation (2.2.46), the separation of the shells is expressed as

$$\delta R = \frac{\delta R_i}{2\epsilon}(\cosh\Theta - 1) - \frac{R_i}{2\epsilon^2}(\cosh\Theta - 1)\delta\epsilon + \frac{R_i}{2\epsilon}\sinh\Theta\delta\Theta, \tag{2.2.47}$$

and $\delta\Theta$ can be obtained by setting $\delta t = 0$ in the second equation (2.2.46).

$$0 = -\frac{1}{\epsilon}(\sinh\Theta - \Theta)\delta\epsilon + \frac{3}{2}(\cosh\Theta - 1)\delta\Theta. \tag{2.2.48}$$

By substituting eqation (2.2.48) into (2.2.47), we obtain

$$\delta R = \frac{\delta R_i}{2\epsilon}(\cosh\Theta - 1)\left(1 - \frac{\partial \ln\epsilon}{\partial \ln R_i}\left[1 + \frac{3}{2}\frac{\sinh\Theta\cdot(\sinh\Theta - \Theta)}{(\cosh\Theta - 1)^2}\right]\right). \tag{2.2.49}$$

At the moment of the shell crossing, the separation δR will be zero. This condition will occur when the parameter becomes $\Theta = \Theta_{sc} \approx 3.488$. At this epoch, the linear and non-linear density contrast inside the void is

$$\delta(\Theta_{sc}) = -0.8, \quad \delta_L(\Theta_{sc}) = -2.71. \tag{2.2.50}$$

Then, we may consider that the low density region with above density contrast has been reached the stage of non-linear evolution.

We summarize the linear and non-linear density evolution of the spherical model for both collapse and expansion cases in Figure 2.2

2.3 Statistics of density perturbation

In the previous section, we have derived how the density field in the universe evolves, but we would not be able to obtain the cosmological information by observing the evolution at each position. In order to obtain the information on the evolution of the cosmological structure formations, we need to "statistically" analyze the density filed. The statistical properties of the density field are represented by two-point correlations of the field which is usually called the correlation function $\xi(r)$ or the power spectrum $P(k)$. Another way is to estimate how many massive structures are formed, which is expressed mass function. In this section, we provide a basic formula for such statistical properties.

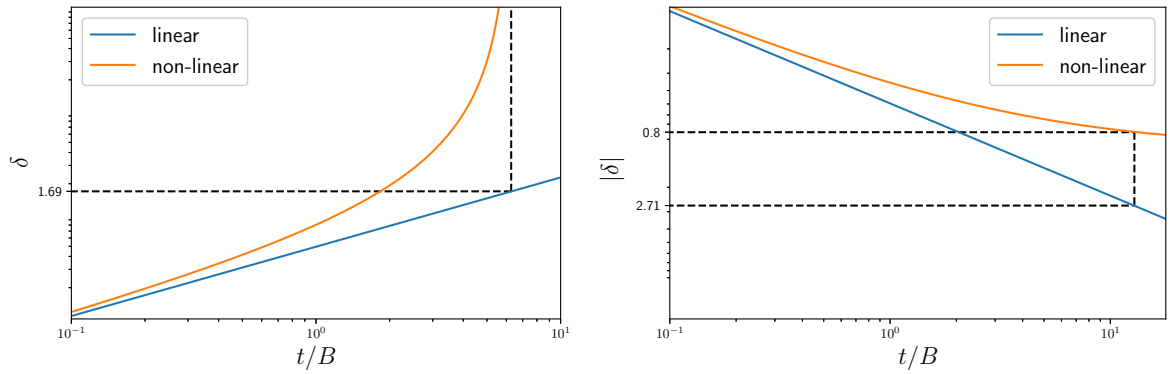

Figure 2.2: Density evolutions in the spherical model both for a collapsing (left) and expanding (right) objects. For the left panel, the horizontal dashed line shows the amplitude of the perturbation as $\delta = 1.69$. When the linear density contrast reaches the value, the non-linear density perturbation goes to ∞. For the right panel, the above horizontal dashed line indicate the amplitude of the $\delta = -2.71$. when the linear perturbation reaches this value, the non-linear density contrast is about -0.8 which is indicated by the below horizontal dashed line.

2.3.1 Correlation function and Power spectrum

The statistical inhomogeneity of the matter distribution is characterized by the relative position of density fields. Let us introduce the two-point correlation function. The two-point correlation function is defined by taking the ensemble average of multiplication of density fields at an fixed separation $|\boldsymbol{x}_1 - \boldsymbol{x}_2|$, which is expressed as

$$\langle \varrho(\boldsymbol{x}_1)\varrho(\boldsymbol{x}_2)\rangle = \bar{\varrho}^2[1 + \xi(|\boldsymbol{x}_1 - \boldsymbol{x}_2|)], \tag{2.3.1}$$

$$\xi|\boldsymbol{x}_1 - \boldsymbol{x}_2| = \langle \delta(\boldsymbol{x}_1)\delta(\boldsymbol{x}_2)\rangle\,. \tag{2.3.2}$$

If the densities with a separation r are not correlate, the value of the correlation function is zero, $\xi(r) = 0$.

The correlation of the density contrast in the Fourier space is the power spectrum. As is the case of the two-point correlation function, taking the ensemble average of the density contrast in Fourier space yields

$$\langle \tilde{\delta}(\boldsymbol{k})\tilde{\delta}(\boldsymbol{k}')\rangle = (2\pi)^3\delta_D(\boldsymbol{k} + \boldsymbol{k}')P(k). \tag{2.3.3}$$

The correlation function and the power spectrum connected each other by the Fourier

transform,

$$P(k) = \int d^3x\ e^{-i\boldsymbol{k}\cdot\boldsymbol{x}}\xi(|\boldsymbol{x}|) = 4\pi \int dx x^2 \frac{\sin(kx)}{kx}\xi(x), \tag{2.3.4}$$

$$\xi(x) = \int \frac{d^3k}{(2\pi)^3}\ e^{i\boldsymbol{k}\cdot\boldsymbol{x}}P(|\boldsymbol{k}|) = \int \frac{dkk^2}{2\pi^2}\frac{\sin(kx)}{kx}P(k). \tag{2.3.5}$$

We also would like to define the variance of the density contrast because it is one of the barometers to measure the property of the density fields. For example, let us consider the matter density field with the smoothing scale R such that the variance of the density overwhelms unity. If so, we consider the density field smoothed by the scale R is in the non-linear stage.

Let us define the density contrast smoothed by the scale R as

$$\delta_R(\boldsymbol{x}) = \int d^3x' W_R(|\boldsymbol{x} - \boldsymbol{x}'|)\delta(\boldsymbol{x}'), \tag{2.3.6}$$

where $W_R(x)$ is a window function. Here we consider a Top-Hat type window function which is expressed as

$$W_R(x) = \frac{3}{4\pi R^3}\Theta(R - x), \tag{2.3.7}$$

$$\Theta(x) = \begin{cases} 1 & (x \geq 0) \\ 0 & (x < 0), \end{cases} \tag{2.3.8}$$

where $\Theta(x)$ is a step function.

Then we can obtain the variance with smoothing scale R from the power spectrum as

$$\sigma^2(R) = \langle \delta_R^2(\boldsymbol{x}) \rangle = \frac{1}{2\pi^2}\int dkk^2\tilde{W}^2(kR)P(k), \tag{2.3.9}$$

where $\tilde{W}(kR)$ is the window function in the Fourier-space,

$$\tilde{W}(kR) = \frac{3}{(kR)^3}\left[\sin(kR) - (kR)\cos(kR)\right] \tag{2.3.10}$$

2.3.2 Mass Function

Counting the number of objects at a specific time is also the measurement of the structure formation of the Universe. Press & Schechter (1974) proposed an analytic model to estimate the number of an object with a mass M by assuming that the primordial mass density field obeys the Gaussian probability distribution and if the density contrast smoothed with mass-scale M reaches a threshold value the object with M has been formed. However, in the Press-Schechter formalism, there is an unknown factor of 2 in order to fill a lack of matter which should be contributed to the structure formation. In 1991, (Bond et al., 1991) suggested another way to derive the mass function by considering a random walk of the linear density fields according to the smoothing scale. In their way, the theory of Press-Schechter would be explained naturally. Furthermore, this formalism can be applied to explain the abundance of the cosmic voids (Sheth & van de Weygaert, 2004). Here we would like to introduce an idea of the mass function which estimates the number of objects according to their mass by combining linear theory and probabilistic property of the density fluctuation.

Excursion set theory

In this section, we would like to introduce the concept of the excursion set formalism. We consider that the linear density contrast with the smoothing radius R distribute in a Gaussian probability,

$$P(\delta_R) = \frac{1}{\sqrt{2\pi\sigma_R^2}} \exp\left(-\frac{\delta_R^2}{2\sigma_R^2}\right), \tag{2.3.11}$$

where σ_R^2 is the variance of the density contrast (see equation (2.3.9)). With a very large smoothing scale, the density contrast and its variance will be zero. Then let us consider the trajectory of $\Pi(\delta_n, S_n = \sigma_n^2)$ which take a random walk starting from $(S_0, \delta_0) = (0, 0)$, which also satisfy

$$\Pi(\delta_n, S_n) = \int d\delta_{n-1} P(\delta_n, S_n|\delta_{n-1}, S_{n-1})\Pi(\delta_{n-1}, S_{n-1}), \tag{2.3.12}$$

where $P(\delta_n, S_n|\delta_{n-1}, S_{n-1})$ is a transition probability. This probability is assumed to have a Gaussian form,

$$P(\delta_n, S_n|\delta_{n-1}, S_{n-1}) = \frac{1}{\sqrt{2\pi\Delta S}} \exp\left(-\frac{\Delta\delta^2}{2\Delta S}\right), \tag{2.3.13}$$

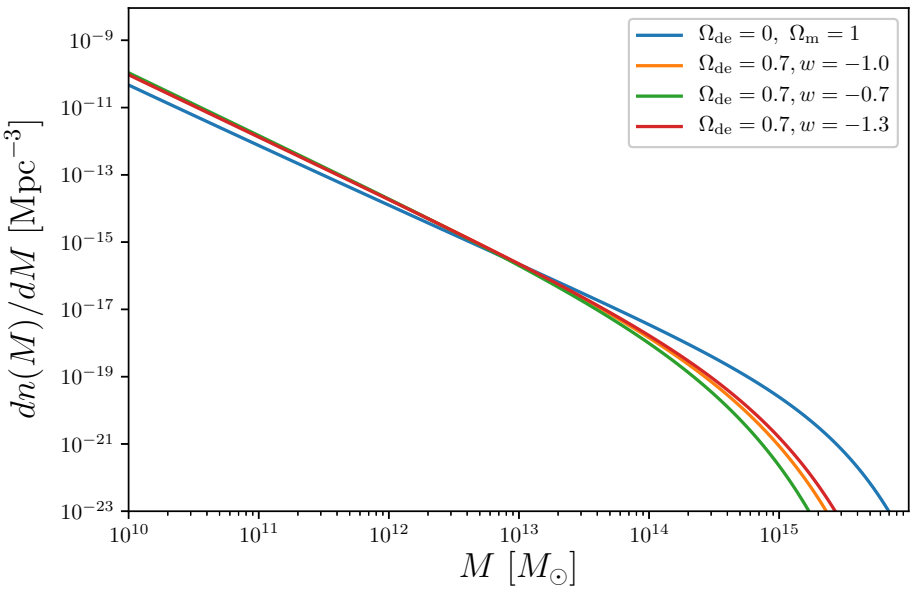

Figure 2.3: Mass functions with different cosmological parameters, but the same initial conditions. The blue line shows the matter dominant universe, while yellow, green and red lines show the universe including dark energy. The difference among dark energy models is represented by the equation of state parameter, w. For yellow, green and red lines we set $w = -1, -0.7$ and -1.3 respectively. The figure shows that in the matter dominant universe there are more massive objects than the universe including dark energy.

where $\Delta\delta = \delta_n - \delta_{n-1}$ and $\Delta S = S_n - S_{n-1}$. Taylor expansion of Π in terms of δ and S results in the diffusion equation about Π

$$\frac{\partial \Pi}{\partial S} = \frac{1}{2}\frac{\partial^2 \Pi}{\partial \delta^2}. \tag{2.3.14}$$

Then, the distribution of Π which satisfies the above equation can be regarded as the distribution of the primordial density fluctuation.

Press-Sheheter Mass function

By solving as the first piercing one barrier problem of the random walk as described by the diffusion equation, we will obtain the Press-Schechter mass function. As we have already derived, we can consider that if the linear density contrast within a region smoothed by the radius R reaches 1.69, mass fragment within the region will be absorbed in the objects with

mass $M = 4\pi\bar{\varrho}R^3/3$. The probability density that Π has never reached δ_c at scale S is

$$\Pi(\delta, S) = \frac{1}{\sqrt{2\pi(S-S_0)}}\left[\exp\left(-\frac{(\delta-\delta_0)^2}{2(S-S_0)}\right) - \exp\left(-\frac{[2(\delta_c-\delta_0)-(\delta-\delta_0)]^2}{2(S-S_0)}\right)\right]. \quad (2.3.15)$$

Thus the probability that the trajectory is above the threshold at scale S is

$$F(S) = 1 - \int_{-\infty}^{\delta_c} \Pi(\delta', S)d\delta'. \quad (2.3.16)$$

The probability that the trajectory first cross the threshold is obtained by subtracting $F(S+dS)$ from $F(S)$,

$$\begin{aligned} f(S)dS = \frac{dF}{dS}dS &= -\left(\int_{-\infty}^{\delta_c}\frac{\partial\Pi}{\partial S}\right)dS \\ &= -\frac{1}{2}\left[\frac{\partial\Pi}{\partial\delta}\right]_{-\infty}^{\delta_c} dS \\ &= \frac{\delta_c-\delta_0}{\sqrt{2\pi(S-S_0)^{3/2}}}\exp\left(\frac{(\delta_c-\delta_0)^2}{2(S-S_0)}\right)dS. \end{aligned} \quad (2.3.17)$$

The total mass of objects whose masses are between M and $M+dM$ is written as

$$n(M)MdM = \bar{\varrho}\frac{dF}{dM}dM, \quad (2.3.18)$$

where $n(M)$ is the number density of objects with mass M. Recalling that $S = \sigma^2(M)$, the number density $n(M)$ is then

$$n(M) = \sqrt{\frac{2}{\pi}}\frac{\bar{\varrho}}{M^2}\left|\frac{d\ln\sigma}{d\ln M}\right|\frac{\delta_c}{\sigma(M)}\exp\left(\frac{\delta_c^2}{2\sigma^2(M)}\right). \quad (2.3.19)$$

This is the Press-Sshechter mass function. In Figure 2.3 we show the example mass functions at present epoch. In order to calculate the mass function, we obtain the variance of the matter density fluctuation by calculating the matter power spectrum using the publicly available code "CAMB" Lewis et al. (2000). We calculate the matter power spectrum with the same initial condition but the different background cosmology such as a matter dominant universe and dynamical dark energy universe. For the dynamical dark energy universe, we vary the equation of state parameter of dark energy as $w_{\rm de} = -1.3, -1$ and -0.7. The $w = -1$ case corresponds

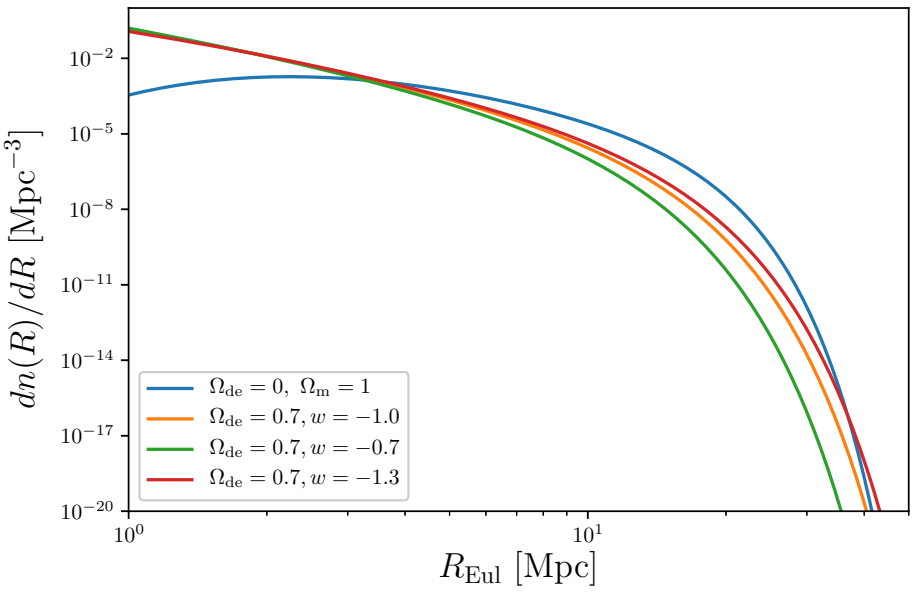

Figure 2.4: The void size function at present epoch with different cosmological parameters. The blue line shows the matter dominant universe, while yellow, green and red lines show the universe including dark energy. The difference among dark energy models is represented by the equation of state parameter, w. For yellow, green and red lines we set $w = -1, -0.7$ and -1.3 respectively. The figure shows that voids of the radius around 10 Mpc are more abundant in the matter dominant universe than the universe in which dark energy exists. However, for small scale, the voids are less exist.

to the ΛCDM model.

In Figure 2.3, we see that there are more massive objects in the matter dominant universe. This is because in such a universe the density perturbation evolves without any retardation such as decreasing the potential due to the accelerating expansion. Among dark energy included universe, $w_{\rm de} = -1.3$ model is producing more massive objects. When the equation of state parameter of dark energy is more negative, the equality epoch between matter and dark energy becomes late, so that until the equality epoch the objects have been formed in the same way as matter dominant universe, then there are more objects in such universe. On the other hand, if $w_{\rm de}$ is less negative, the opposite phenomenon would occur, so that objects are less abundant.

Sheth-van de Weygaert Void size function

For cosmic void abundance, we may simply think to replace the threshold value δ_c^{lin} with void formation criteria δ_v. However, the void case is a little bit different from the case of halos.

Let us consider a situation that the density contrast smoothed by scale R is below δ_v, but it is above δ_c when the smoothing scale is larger than R. Such a region seems like a void but at scale R but should become a halo with $M = 4\pi\bar{\varrho}R'^3/3$ where $R' > R$. Thus we should not count such void. In terms of the random walk trajectory, the situation corresponds to that the trajectory reaches δ_c before reaching δ_v. What we have to estimate is the distribution of Π which has never reached both δ_c and δ_v until scale S. This was pointed by Sheth & van de Weygaert (2004) and they suggested this process is solved by setting the random walk as a two barrier problem.

The solution is

$$\begin{aligned}\Pi(\delta, S) =& \frac{1}{\delta_c - \delta_v} \sum_{n=1}^{\infty} \left[\cos\left(\frac{n\pi}{\delta_c - \delta_v} \delta \right) - \cos\left(\frac{n\pi}{\delta_c - \delta_v} (2\delta_v - \delta) \right) \right] \\ & \times \exp\left(-\frac{n^2\pi^2}{2(\delta_c - \delta_v)} S \right). \end{aligned} \tag{2.3.20}$$

The same as the halo case, the fraction of Π that is between δ_c and δ_v at a scale S is

$$F(S) = 1 - \int_{-\delta_v}^{\delta_c} \Pi(\delta', S) d\delta', \tag{2.3.21}$$

and the first crossing the thresholds at scale S is

$$\begin{aligned} f(S)dS &= -\frac{1}{2} \left[\frac{\partial \Pi}{\partial \delta} \right]_{\delta_v}^{\delta_c} dS \\ &= -\frac{1}{2} \left[\left. \frac{\partial \Pi}{\partial \delta} \right|_{\delta=\delta_c} - \left. \frac{\partial \Pi}{\partial \delta} \right|_{\delta=\delta_v} \right] dS. \end{aligned} \tag{2.3.22}$$

As an analogy to the halo case, the first term will produce the probability of the first crossing of δ_c which is not our interest here. What we want is the first crossing of δ_v which is the second term of the above equation. Then, the fraction that the trajectories first cross δ_v without breaking δ_c before is

$$\begin{aligned} f_v(S)dS &= \left. \frac{1}{2} \frac{\partial \Pi}{\partial \delta} \right|_{\delta=\delta_v} dS \\ &= \sum_{n=1}^{\infty} \frac{n\pi\mathcal{D}}{\delta_v^2} \sin(n\pi\mathcal{D}) \exp\left(\frac{n^2\pi^2\mathcal{D}^2}{2} \frac{S}{\delta_v^2} \right) dS. \end{aligned} \tag{2.3.23}$$

Thus the number density of voids including mass M is

$$n_v(M) = \frac{\bar{\varrho}}{M^2}\nu f_v(\nu)\frac{d\ln\nu}{d\ln M}, \tag{2.3.24}$$

where we exchange the valuable S to $\nu = |\delta_v|/S^{1/2}$ and $\nu f_v(\nu)$ is

$$\nu f(\nu) = \sum_{n=1}^{\infty} \frac{2n\pi\mathcal{D}^2}{\nu^2}\sin(n\pi\mathcal{D})\exp\left(-\frac{n^2\pi^2\mathcal{D}^2}{2\nu^2}\right), \tag{2.3.25}$$

where $\mathcal{D} = |\delta_v|/(\delta_c + |\delta_v|)$. For voids, it is convenient to express its abundance in terms of their size. This can be done by the mass conservation low,

$$M = \frac{4\pi}{3}\bar{\varrho}R_{Lag}^3 = (1+\delta)\frac{4\pi}{3}\bar{\varrho}R_{Eul}^3, \tag{2.3.26}$$

where $R_{\rm lag}$ is a radius in the Lagrangian coordinate which corresponds to the initial position of the mass fragment and $R_{\rm Eul}$ is the radius measured in the Eulerian coordinate by which we measure the void size observationally. We can change the valuables as

$$3\frac{dn(M)}{d\ln M} = \frac{dn(R_{\rm Lag})}{d\ln R_{\rm Lag}} = \frac{dn}{d\ln R_{\rm Eul}}, \tag{2.3.27}$$

with $R_{\rm Lag}^3 = (1+\delta)R_{\rm Eul}^3$. This relations result in

$$\frac{dn}{dR_{\rm Eul}} = (1+\delta)^{1/3}\frac{3}{4\pi R_{\rm Lag}^3}f(\nu,\delta_v,\delta_c)\frac{d\nu}{dR_{\rm Lag}}. \tag{2.3.28}$$

In Figure 2.4 we show an example void size distribution at the present epoch. Here we again use the same power spectrum described in the Press-Schechter mass function. The figure shows that in the matter-dominant universe voids of the radius around 10 Mpc are more abundant if the initial conditions are the same. However, for small scales, the number of voids is less compared to the universe including dark energy. The reason might be that for the matter-dominant universe the expansion is decreasing so that the objects easily collapse and the void-in-cloud process significantly affects the small scale voids. On the other hand, in the dark energy dominant universe, the accelerating expansion retards the collapsing process, so that the number of small voids is abundant compared to the matter dominant universe. This effect might be significant for the large scales. Thus even though the number of voids

about 10 Mpc seems to be less for dark energy included model, larger voids should be more abundant. We can see this at the large radius tails in the Figure, such that the number of voids in the matter dominant universe lastly decreases at the large scales more than 20 Mpc.

Although we have shown the dependence of the void size function on the budget and equation of state of dark energy, there is another possibility that affects the size function due to the nature of dark energy. That is the spacial perturbation of dark energy. In the next chapter, we will investigate the effect of dark energy perturbation on the void formations.

Chapter 3

Cosmology with cosmic void

The cosmology with cosmic voids has been paid more attention because of the development of the theoretical study and numerical way to identify cosmic voids from the cosmic web, as well as the wider observation of the large scale structures. There seem to be some merits to study voids in a cosmological context since they are considered to be one of "clean" objects to trace the nature of dark energy. By definition of them, they are matter less so that dark might be the dominant component if its clustering is not strong. In this chapter, we would like to show some topics of voids related to dark energy, especially the void abundance and void shape. For the void abundance, we first review some previous works and then, we investigate the impact of the dark energy clustering on the void formation in a numerical way. After that, we introduce the topic of the void shape, particularly the Alcock-Paczynski test.

3.1 Void abundance

In Section 3.1, we have introduced one of the theoretical ways to estimate the abundance of voids. Even though the theoretical model is not enough to estimate the actual abundance of the void in matter density fields because of the assumption of the spherical void formulation and sharp k filtering (Bond et al., 1991). This abundance model has been applied to constrain cosmology in some studies (Clampitt et al., 2013; Pisani et al., 2015; Zivick & Sutter, 2016; Endo et al., 2018; Verza et al., 2019).

The cosmological dependence comes through $\sigma^2(R)$, δ_c and δ_v, which are the variance of the mass fluctuation, the linear density contrast for the collapsed objects and voids, respectively. About the void abundance, the cosmological application is focused on the equation of state of the dark energy (Pisani et al., 2015; Verza et al., 2019) because it affects the growth mode of the density perturbation (see Section 2.2.1). However, the clustering property of dark energy also affects the evolution of structure formation. This effect on the high-density objects has

been investigated by several authors (Chiba et al., 1998; Abramo et al., 2007; Basse et al., 2011), but not so much on the formation of cosmic voids (Novosyadlyj et al., 2016). Inside the cosmic voids, the matter is not the dominant component, so that the nature of dark energy would easily appear in the void formation. In order to investigate the effect, we first consider a simple model such as the evolution of a spherically expanding object and evolution of dark energy perturbation inside the void following the formalism of Basse et al. (2011).

Void evolution with dark energy perturbation

We describe the evolution of a void in the presence of dark energy perturbation by coupling the spherical expansion model and linear perturbation theory.

The evolution of the void radius is

$$\frac{\ddot{X}_{\rm v}}{X_{\rm v}} + \mathcal{H}\frac{\dot{X}_{\rm v}}{X_{\rm v}} = -\frac{4\pi G}{3}a^2[\bar{\rho}_{\rm m}\delta_{\rm m}^{\rm TH} + \bar{\rho}_{\rm de}\delta_{\rm de}^{\rm TH} + 3\delta P_{\rm de}^{\rm TH}]. \tag{3.1.1}$$

where X denotes the void radius in comoving coordinate, $\mathcal{H}$ is a conformal Hubble parameter $\mathcal{H} = aH$, $\bar{\rho}_{\rm m}$ and $\bar{\rho}_{\rm de}$ are background energy density of matter and dark energy, respectively. The dot means a derivative in terms of conformal time $d\tau = adt$. $\delta_{\rm m}^{\rm TH}$, $\delta_{\rm de}^{\rm TH}$ and $\delta P_{\rm de}^{\rm TH}$ are density perturbation of dark matter, dark energy and pressure perturbation of dark energy respectively, where we assume a top-hat profile for them. For matter density contrast we use a mass conservation such that

$$\delta_{\rm m}^{\rm TH}(\tau) = (1+\delta_{{\rm m},i}^{\rm TH})\left[\frac{X_{{\rm v},i}}{X_{\rm v}(\tau)}\right]^3 - 1. \tag{3.1.2}$$

On the other hand, we solve continuity and Euler equations. In order to introduce the dark energy pressure into those equations, we adopt a pseudo-Newtonian approach (Lima et al., 1997). The equation of evolution of dark energy perturbation in Fourier space is then,

$$\dot{\tilde{\delta}}_{\rm de}^{\rm lin} + 3(c_s^2 - w)\mathcal{H}\tilde{\delta}_{\rm de}^{\rm lin} + (1+w)\tilde{\theta}_{\rm de}^{\rm lin} = 0, \tag{3.1.3}$$

$$\dot{\tilde{\theta}}_{\rm de}^{\rm lin} + (1-3c_s^2)\mathcal{H}\tilde{\theta}_{\rm de}^{\rm lin} - \frac{k^2c_s^2}{1+w}\tilde{\delta}_{\rm de}^{\rm lin} - k^2\tilde{\phi} = 0. \tag{3.1.4}$$

where $\theta_{\rm de}$ is a divergence of the velocity of dark energy, c_s is the speed of sound of dark energy and $\tilde{\phi}$ is the gravitational potential which satisfies the poisson equation,

$$-k^2\tilde{\phi} = 4\pi G a^2[\bar{\rho}_{\rm m}\tilde{\delta}_{\rm m} + \bar{\rho}_{\rm de}\tilde{\delta}_{\rm de} + 3\delta\tilde{P}_{\rm de}]. \tag{3.1.5}$$

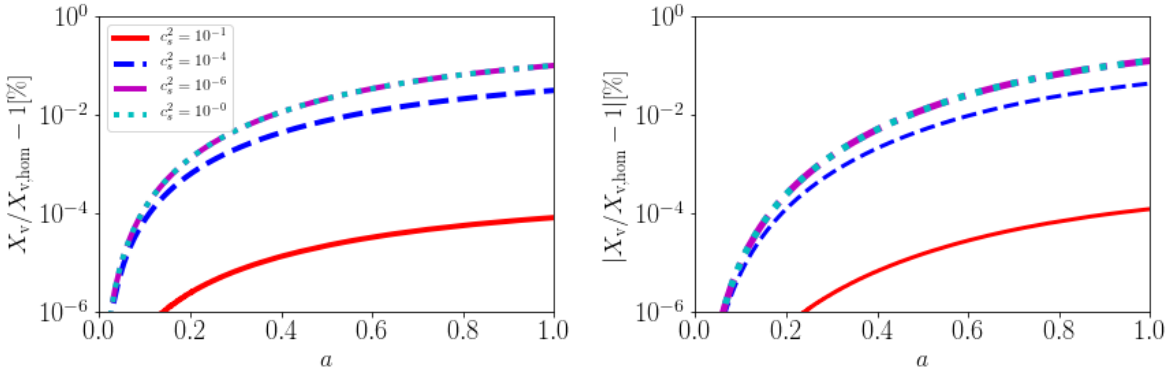

Figure 3.1: Relative evolution of a isolated void with a top hat density profile. We set $w=-0.9$ for the left panel while $w=-1.3$ for the right panel. In both the left and right panels, we show the deviation from the homogeneous dark energy model such that $c_s^2=1$. We find that in the case of small speed of sound the void evolution is enhanced when $w=-0.9$ while it is suppressed when $w=-1.3$. The deviations are expressed by percent, so that for both cases the deviations are less than 0.01.

Those equations are combined into

$$\frac{d^2\tilde{\delta}_{\rm de}^{\rm lin}}{ds^2}+\mathcal{D}(s)\frac{d\tilde{\delta}_{\rm de}^{\rm lin}}{ds}+\left[\frac{k^2c_s^2}{\mathcal{H}^2}\chi(s)-\kappa(s)\right]\tilde{\delta}_{\rm de}^{\rm lin}=\frac{3}{2}(1+w)\Omega_{\rm m}(s)\tilde{\delta}_{\rm m}, \tag{3.1.6}$$

where

$$s=\ln a, \tag{3.1.7}$$

$$\mathcal{D}(s)\equiv 1+\frac{1}{\mathcal{H}}\frac{d\mathcal{H}}{ds}-3w, \tag{3.1.8}$$

$$\kappa(s)\equiv 3w\left(1+\frac{1}{\mathcal{H}}\frac{d\mathcal{H}}{ds}\right)+\frac{3}{2}(1+w)\Omega_{\rm de}(s), \tag{3.1.9}$$

$$\chi(s)\equiv 1+3\frac{\mathcal{H}^2}{k^2}\left[1+\frac{1}{\mathcal{H}}\frac{d\mathcal{H}}{ds}-3(c_s^2-w)-\frac{3}{2}(1+w)\Omega_{\rm de}(s)\right]. \tag{3.1.10}$$

We solve the equation numerically with the initial conditions described in Endo et al. (2018).

In Figure 3.1, we show the relative evolution for the void of the radius 18 Mpc at the initial epoch with different speed of sound of dark energy, $c_s^2=10^{-1}, c_s^2=10^{-4}, c_s^2=10^{-6}, c_s^2=0$. Here we set the equation of state parameter of dark energy $w=-0.9$ for the left panel while $w=-1.3$ for the right panel in Figure. The horizontal axis shows the scale factor and we have normalized it as 1 at present. We find that in the case of small speed, the evolution of void is enhanced when $w=-0.9$ (left), while it is suppressed for $w=-1.3$ (right). Whether

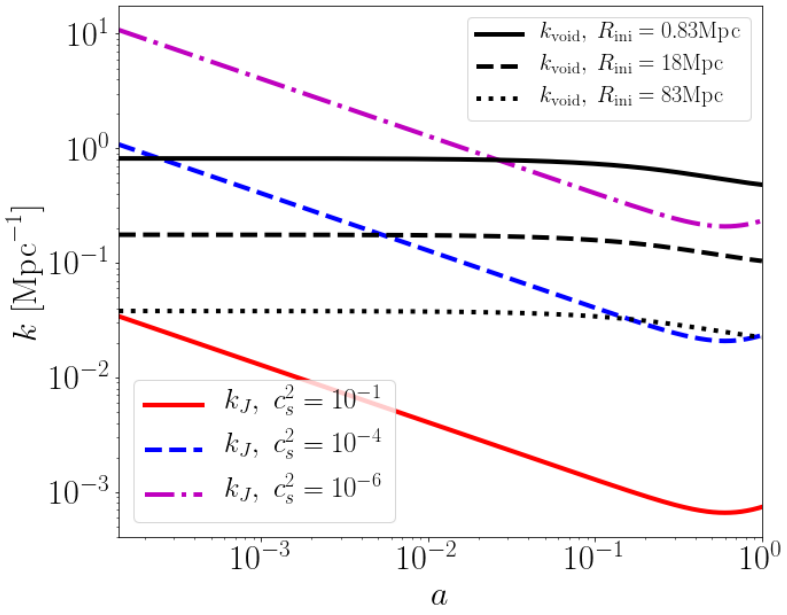

Figure 3.2: Time evolution of the Jeans wavenumber for different speed of sound. We set $w = -0.9$, and speed of sound of dark energy as $c_s^2 = 10^{-1}, 10^{-4}$ and 10^{-6}, which are represented by the red solid, blue dashed and magenta dotted-dashed lines respectively. The black lines indicate wavenumbers corresponding to the void radius with the initial size of 0.83 (dotted), 18 (dashed) and 83 (solid) Mpc. The correction of the wavenumber of Jeans length and void radius means the point that the Jeans length and void radius are equal.

the perturbation of dark energy enhances or suppresses the void evolution is determined by the sign of $1 - w$. In equation (3.1.6), we can see that if $w > -1$ the density contrast of dark energy will evolve with the same sign as matter perturbation, which leads to the enhancement of gravitational potential inside the void as (3.1.1), so that the evolution of the void is promoted. On the other hand, when $w < -1$, we see the opposite phenomenon in the evolution of matter and dark energy, which results in the reduction of the potential inside the void.

In addition to the above trends, we can find that there seems to be no difference between $c_s^2 = 10^{-6}$ and $c_s^2 = 0$. This is understood in terms of the Jeans instability as mentioned in Section 3.1 According to the idea of the Jeans instability, the fluctuation with wavelength k will collapse if k is smaller than k_J, where k_J is the Jeans wavenumber. In Figure 3.2, we show the time evolution of the Jeans wavenumbers with a different speed of sound of dark energy. We set $w = -0.9$ and also show the wavenumbers which correspond to the void radius. According to Figure 3.2, for $c_s^2 = 10^{-1}$ the Jeans length is larger than any void radius, which

means that dark energy perturbation hardly evolves inside those voids in this case.

On the other hand, k_J with c_s^2 crosses the wavenumber corresponding to the scales of about 1 and 20 Mpc very early epoch while it reaches about 80 Mpc later. For this case, the perturbation of dark energy could grow at the early epoch inside those voids, but the growth has stopped once the Jeans length overwhelm the void radius. The Jeans length for $c_s^2 = 10^{-6}$, the length has never become larger than the voids with the initial radius of 20 Mpc. In this case, the perturbation can grow until $a = 1$ inside the voids larger than 20 Mpc. We can see those differences in dark energy perturbation with the different speeds of sound in the different evolution of the void radius in figure 3.1. The perturbation of dark energy inside the void can grow until the late time if c_s^2 is smaller than 10^6, and if c_s^2 is smaller than the value, the perturbation has not been suppressed such that there is no difference in the evolution of the void among those cases.

We can see the different time evolution of dark energy perturbation inside void according to the different speed of sound of dark energy more explicitly in Figure 3.3. In Figure 3.3 we show three wavenumber modes of dark energy density perturbation in Fourier space. For $k = 0.01$ mode, the Jeans length reaches very early at this length when $c_s^2 = 0.1$ so that the perturbation does not grow. For this mode, the Jeans wavenumber of $c_s^2 = 10^{-4}$ reaches $k = 0.01$ while that of $c_s^2 = 10^{-4}$ has not reached the value, so that perturbation of this mode stop to grow at the epoch the Jeans length cross the scale of the mode when $c_s^2 = 10^{-4}$ while it continues to evolve when $c_s^2 = 10^{-6}$. For other wavenumber modes, we can understand their evolution in the same manner.

Void size distribution with dark energy perturbation

So far we have investigated the effect of dark energy perturbation on the evolution of each void. However, even though we observe the evolution of each void precisely, we do not obtain the information of dark energy perturbation because the difference between the growth of each void is more affected by their uniqueness. To draw the nature of dark energy from voids, we need to consider the statistical property of them, one of which is the void size function. In Section 2.3.2 we have derived the size function of voids using the excursion set formalism. Recent studies have argued that the original Sheth-van de Weygaert void size function does not fit the void distribution found in the n-body simulation, so some studies extend the model by setting δ_v as a free parameter and so on.

In this work we adopt the original void size function derived in Section 3.1 to see the effect of dark energy perturbation on the void size distribution. As shown in the previous section, the dark energy perturbation affects the matter density perturbation. In terms of the size function, this effect comes through the variance of mass density fluctuation, namely

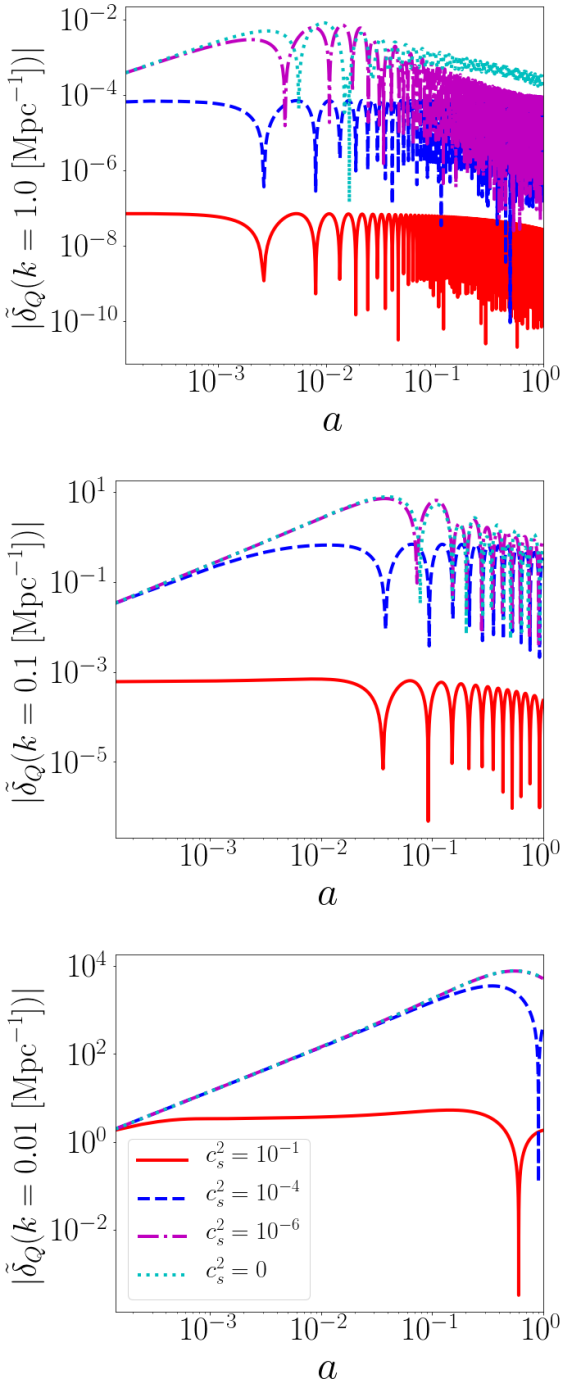

Figure 3.3: Evolutions of density perturbation of dark energy in Fourier space. The evolution for $k = 0.01, 0.1$ and $1.0\mathrm{Mpc}^{-1}$ are shown in the top, middle and bottom panels, respectively. Each density contrast begins to oscillate when the Jeans length for each value of the speed of sound crosses the wavelength.

$\sigma^2(M)$ which is expressed by the integral of the matter power spectrum combined with the window function (see equation (2.3.9)). In order to calculate the matter power spectrum in the presence of dark energy perturbation, we utilize the publicly available code "CAMB" (Lewis et al., 2000). In Figure 3.4 we show the deviations of $\sigma^2(R)$ from the monogynous dark energy model. We set the same initial condition but the different speed of sound. For the left panel, we set $w = -0.9$ and as we have seen that the fluctuation of dark energy enhances the matter density perturbation, the variance deviates more when c_s^2 is small. Also, the enhancement affects negatively when $w < -1.0$.

We show the resulting void size distribution as a deviation from the uniform dark energy model in Figure 3.5. In the left panel of Figure 3.5, for $w = -0.9$, the relative abundance is clear at the void radius of $R \sim 5$ Mpc when $c_s^2 \leq 10^{-6}$, while for $c_s^2 = 10^{-4}$ the deviation appear at the scale of $R \sim 10$ Mpc and for $c_s^2 = 10^{-1}$ the deviation can not be seen in the radius range. This is also because of the Jeans instability. For small speed of sound small scale but larger than the corresponding Jeans length, the fluctuation in dark energy can evolve and affect matter density fluctuation. Although we could not see the deviation from the uniform dark energy model when $c_s^2 = 10^{-1}$ in the range, we would confirm the deviation if we observe larger voids. According to the previous discussion of Jeans length, such deviation could appear at $R \geq 10^3$ Mpc. As we mentioned, the effect of dark energy perturbation on the void abundance is different between $w > -1$ and $w < -1$. When $w > -1$, the effect appears as an enhancement of the abundance of large voids while when $w < -1$ the effect appears as the opposite. Even though the deviations in $\sigma^2(R)$ are sub percent level, the deviations in the abundance model are quite large. The reason might be due to the fact that the model includes exponential terms, such that the model is sensitive to the even small deviation in $\sigma^2(R)$.

Summary of effects of dark energy perturbation on the void formation

We have investigated the effects of dark energy perturbation on the formation of cosmic voids in this section. We have treated the speed of sound and the equation of state of dark energy as constant parameters in our model. We studied the dependence of the formation of an isolated spherically symmetric void on these parameters and the initial size of the void. We found that the effects of the different values of the speed of sound and initial sizes are much small. These results are broadly consistent with those of Novosyadlyj et al. (2016), and may lead us to the conclusion that the dark energy perturbation does not greatly affect void formation. We also investigated the effects of the dark energy perturbation on the abundance of voids based on the excursion set theory. We found that the differences between the homogeneous and inhomogeneous dark energy models are significant when the speed of sound is much smaller

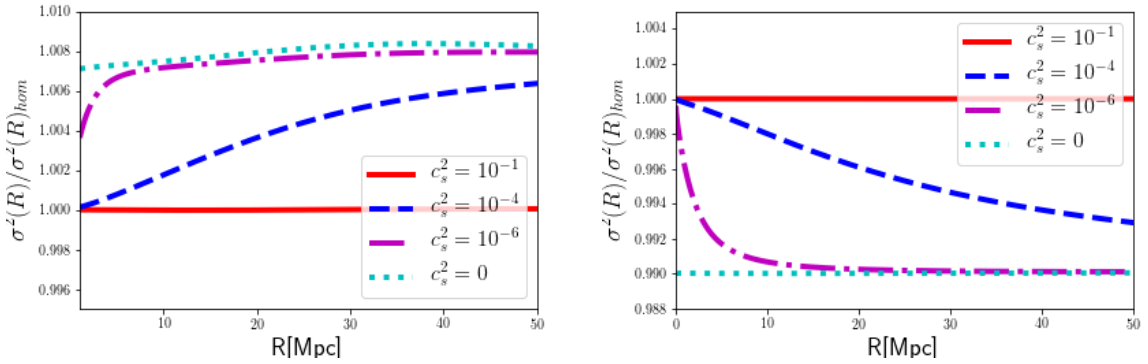

Figure 3.4: Comparison of variance at present time. We set w = − 0.9 for the left panel and w = − 1.3 for the right panel. Both panels show the fractional difference from the homogeneous dark energy mode.

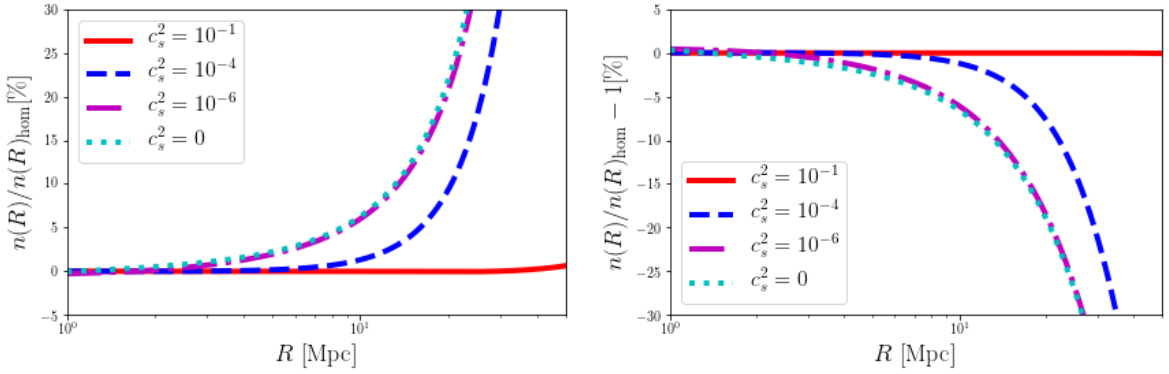

Figure 3.5: Comparison of the abundance of voids at present time. We fix w = − 0.9 (left) and w = − 1.3 (right), and the values of speed of sound as c2s = 0,10 − 6,10 − 4,10 − 1. The lower panels show the fractional difference from the homogeneous dark energy model with the same equation of state parameter, where N′ = dN/dRv. For both w, the deviation from the case for homogeneous dark energy is noticeable at larger radii: more than 10 % for c2s = 0 for 30 Mpc voids.

than that of light.

3.2 Void shape

The shape of cosmic voids is also one of the features of voids and can be applied to prove the nature of dark energy. In this section, we are going to use its shape to investigate the expansion history of the Universe. Due to the expansion of the Universe, we can not measure the size of objects quite far from us directly. What we can observe is redshifts and angle as the location of the object. To estimate the size of the object, we have to assume a kind of cosmological model. In this section, we briefly introduce the Alcock-Paczynski cosmological test which is an evolution model-free method to measure the expansion history of the Universe and the relation between the test and cosmic voids.

3.2.1 Alcock Paczynski test

In 1979, Alcock & Paczynski (1979) proposed a unique way to probe an expansion history of the Universe which does not depend on any evolution model of the structure formation, so-called the Alcock-Paczynski test (AP test). Since the universe is expanding, the observational shape of an object has a different dependence on the expansion. Let us consider observing a spherical object which is located quite far from us. The observable about the object is the redshift span Δz and angular span $\Delta\theta$, where $\Delta z, \Delta\theta \ll 1$. By definition of the relation between the comoving scale and these observables,

$$\begin{aligned} \Delta x_{\parallel} &= \int_{z}^{z+\Delta z} \frac{c}{H(z')} d(z') \simeq \frac{c}{H(z)} \Delta z, \\ \Delta x_{\perp} &= \Delta\theta \chi(z) \end{aligned} \tag{3.2.1}$$

where $H(z)$ and $\chi(z)$ is the Hubble parameter at redshift z and the comoving distance to the redshift, respectively. Since we have assumed that the object is spherical, such that $\Delta x_{\parallel} = \Delta x_{\perp}$,

$$\frac{\Delta z}{z\Delta\theta} = \frac{H(z)\chi(z)}{cz}. \tag{3.2.2}$$

Again, what we observe is the combination of Δz and $\Delta\theta$ by observing a spherical object at z. Thus the combination tells us the information included in the Hubble parameter such as Ω or w. We note that when the AP test was proposed, it was assumed to observe an intrinsically spherical object to conduct the test. However, one of the powerful points of the test is that it

can be applied to statistical isotropy. In the next section, we introduce an application of the AP test to the cosmic void which is not spherical individually but statistically.

Alcock Paczynski test with voids

The application of the observed void shape to the AP test was first pointed out by Ryden (1995). In their work, they assumed that each void is spherical and expands isotropically with no peculiar velocities for simplicity. The peculiar velocities of objects are another source of the shape distortion in the redshift survey. Also, the shapes of voids in the matter density fields or the galaxy distribution are not spherical (Platen et al., 2008; van de Weygaert, 2016). Thus, the practice of the AP test with cosmic voids seems to be difficult by the method with Ryden (1995).

However Lavaux & Wandelt (2012) has improved the possibility of the AP test with cosmic voids. They noticed the statistical isotropy of the void shape based on the cosmological principle even though each void shape is not spherical. They show that the averaged shape of voids will be spherical when they are stacked. However, they also showed that this sphericity is broken in redshift-space because the peculiar velocities of astronomical objects cause a Doppler shift, so that the constructed position from the redshifts is not exact. For clusters, this effect appears in a different way depending on the scales. For a large scale cluster, the objects tend to gather their center of the gravitational potential which causes the cluster seems to be flattened along the line of sight, while for small scales in which clusters are Virialized, the random motions of the objects cause an elongation along the line of sight.

In the case of voids, they found that the redshift-space distortion (RSD) on voids appears as a flattening along the line of sight. They mentioned some possible origins of this effect. One of which is that since the void ridge is usually high-dense region such as clusters of Virtualized objects, so the boundaries of voids are elongated along the line of sight that causes void region shortened along the line of sight.

One of the interesting features of RSD on cosmic voids is that Lavaux & Wandelt (2012) found the flattening effect does not depend on redshift, which indicates that the shape distortion due to the peculiar velocity on the stacked voids can be removable by tracing the redshift dependence of the signals or multiplying a constant correction factor. According to their analysis after shape correction, joint analysis of the BAO and the AP test with stacked voids has a potential of a tighter constraint on the cosmological parameters.

Motivated by the authors, there have been several attempts to constrain cosmological models by the AP test. The first try was done by Sutter et al. (2012b). They analyzed their void catalogs (Sutter et al., 2012c) which were obtained from the galaxy catalog of the Sloan Digital Sky Survey Data Release 7 (SDSS DR7) (Blanton et al., 2005; Abazajian et al., 2009).

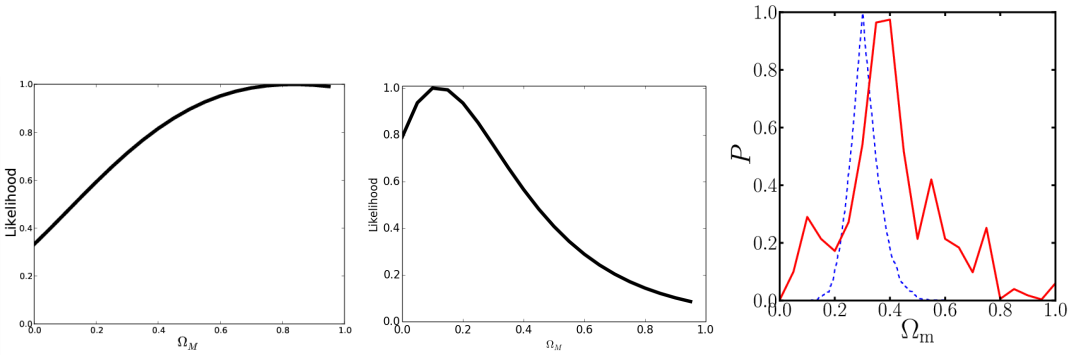

Figure 3.6: One-dimensional normalized likelihood as a function of $\Omega_{\rm m}$ for our stacked void measurements, after correcting for peculiar velocities. The left, middle and right panels are adopted from Sutter et al. (2012b), Sutter et al. (2014) and Mao et al. (2017b) respectively.

They identified voids with a modified void finding algorithm ZOBOV (Neyrinck, 2008) which is described in the later section in this thesis. Their first attempt was, however, failed due to the large shape noise which is caused by the insufficient number of sample voids.

They revisited the AP test but with later data set(Sutter et al., 2014), SDSS DR7 and DR10 LOWZ and CMASS samples (Ahn et al., 2014). In this analysis, they found about 1500 void samples and measured the AP signal by correcting the shape distortion due to the peculiar velocities by using the correction factor which appears in Lavaux & Wandelt (2012). Although the final result of their analysis has a large uncertainty and the most preferable value of the cosmological parameter is deviated from the standard model, their results surely suggested that the energy fraction of matter density of the Universe is not unity.

Mao et al. (2017b) would be the latest practice of the Alcock-Paczynski test until now. They used the galaxy catalog of the SDSS DR12 (Alam et al., 2015) to obtain the void catalog (Mao et al., 2017c) in which they identify $1,228$ voids. As mentioned above, the effect of redshift-space distortion on stacked voids appears in a similar way in any void radius and redshift, they try to calibrate the effect using mock galaxy catalogs rather than using the correction factor as mentioned by previous works. Since they stacked all voids by normalizing the particle position from the center of voids, the shape measurement would be more precise than the previous works in which those authors stacked voids within a radius bin. Comparing the calibrated shape distortion and the observed data, they put a constraint on the matter density which seems tighter than the previous works.

We summarize the previous results in Figure 3.6. The panels in Figure 3.6 is adopted from those previous works (Sutter et al., 2012b, 2014; Mao et al., 2017b)

Future prospects

As mentioned by the previous works, one of the essential factors of success in the AP test with stacked voids is a large number of void samples to determine the shape with small uncertainty. However, the conventional galaxy surveys need a significant cost to determine the position of galaxies with large survey volume.

Recently, a quite powerful way to observe the matter distribution in the Universe has been proposed. In that way, we observe the emission or absorption of the neutral hydrogen (HI). The resolution of the observation will not be enough to identify each galaxy, but we can obtain the distribution of HI with a huge survey volume.

Therefore we are going to investigate the possibility of the AP test with stacked void technique in order to prepare the cosmological application of the future large scale HI survey. In the next chapter, we explain the mechanism of the HI emission or absorption and the survey with the future Square Kilometre Array (SKA) HI intensity mapping survey.

Chapter 4

21cm signal

So far large scale galaxy surveys have been used to trace the matter distribution of the universe. In order to examine the cosmological models, we need far larger scales of the matter distribution. However, galaxy surveys need a lot of time to identify the location of the galaxy, so that tracing the larger scale of the matter distribution far from us is time expensive.

On the other hand, it has been expected to survey the large scale distribution of the neutral hydrogen along with the large scale structure. The HI intensity mapping survey has a huge potential to observe a quite huge volume of the Universe. Thus if we identify the void structures from the HI distributions, we will obtain much more void samples so as to determine the shape of voids. In this chapter, we introduce the mechanism of the emission line from the HI and intensity mapping survey by the future SKA experiments.

4.1 Brightness temperature

In order to derive the emission of the neutral hydrogens (HI) in the Universe, we would like to consider the radiation-transfer mechanism of the HI clouds. The total difference of the absorption and emission in a fragment of the HI cloud is

$$dI_\nu(x) = -\kappa_\nu(x) I_\nu(x) dx + \epsilon_\nu(x) dx, \tag{4.1.1}$$

where I_ν is the radiation intensity with a frequency ν, κ_ν is an absorption coefficient, ϵ_ν is an emission coefficient and x is a distance along the line of sight. Assuming those coefficients

dose not depend on the location, we obtain

$$I_\nu(x) = I_\nu(0)e^{-\tau_\nu(x)} + S_\nu(1 - e^{-\tau_\nu(x)}), \tag{4.1.2}$$

$$\tau_\nu(x) = \int_0^x \kappa_\nu dx', \tag{4.1.3}$$

$$S_\nu = \frac{\epsilon_\nu}{\kappa_\nu} \tag{4.1.4}$$

where τ_ν is an optical depth which is an integral of the absorption coefficient and S_ν is a source function.

The emission and absorption coefficients are expressed by Einstein's coefficients,

$$\epsilon_\nu = \frac{h\nu}{4\pi} n_1 A_{10} \phi(\nu), \tag{4.1.5}$$

$$\kappa_\nu = \frac{h\nu}{4\pi}(n_0 B_{01} - n_1 B_{10})\phi(\nu), \tag{4.1.6}$$

where h is the Planck constant, n_1 and n_2 is the number of neutral hydrogens which is in the lower and higher energy state respectively, A_{10}, B_{10} and B_{01} are the Einstein's coefficients for the spontaneous emission, absorption and stimulated emission respectively, and $\phi(\nu)$ is a line profile which satisfy $\int \phi(\nu)d\nu = 1$. There is a relation between these coefficients,

$$n_1 A_{10} + n_2 B_{10} \bar{I}_\nu = n_0 B_{01} \bar{I}_\nu \tag{4.1.7}$$

where $\bar{I}_\nu$ is an angular averaged intensity $\bar{I}_\nu = \int I_\nu d\Omega/4\pi$. From equation (4.1.7),

$$\bar{I}_\nu = \frac{n_0 A_{10}}{n_0 B_{12} - n_1 B_{10}} = \frac{A_{10}}{B_{10}} \frac{1}{\dfrac{n_0}{n_1}\dfrac{B_{01}}{B_{10}} - 1}. \tag{4.1.8}$$

If the system is in the thermal equilibrium, the intensity can be written by the Planck's law,

$$\bar{I}_\nu = \frac{2\pi h\nu^3}{c^2} \left[\exp\left(\frac{h\nu}{k_B T}\right) - 1\right]^{-1}. \tag{4.1.9}$$

where k_B is the Boltzmann constant and T is the temperature of the HI cloud.

The number of particles in each state obeys the Boltzmann distribution,

$$\frac{n_1}{n_0} = \frac{g_1}{g_0} \exp\left(-\frac{h\nu}{k_B T}\right), \tag{4.1.10}$$

where g_0 and g_1 are statistical weights, here $g_0 = 1$ and $g_1 = 3$, T is called the excitation temperature which determines the relative number of particles in each state.

By comparing the equations (4.1.8), (4.1.9) and (4.1.10), we get relations

$$\frac{A_{10}}{B_{10}} = \frac{2h\nu^3}{c^2}, \quad \frac{g_0}{g_1}\frac{B_{01}}{B_{10}} = 1. \tag{4.1.11}$$

Then we go back to the source function of the HI clouds, and it is written by those relations as

$$S_\nu = \frac{2h\nu^3}{c^2}\left[\exp\left(\frac{h\nu}{kT_s}\right) - 1\right]^{-1}. \tag{4.1.12}$$

For the case of 21cm line, $\nu = 1420.4057$ MHz, so that we can take the Rayleigh-Jeans limit and we can write the equation (4.1.2) in terms of the temperature

$$T_b = T_s(1 - e^{-\tau}), \tag{4.1.13}$$

where T_b is called the brightness temperature. If there is no other source object behind the HI could, the observed brightness temperature is given as a difference from the CMB radiation,

$$\delta T_b = (T_\mathrm{s} - T_\mathrm{CMB})(1 - e^{-\tau}), \tag{4.1.14}$$

where we call δT_b differential brightness temperature. The optical depth is given by the integral of κ which is written as (4.1.6), then referring the equations (4.1.8) and (4.1.11),

$$\kappa_\nu = \frac{c^2}{8\pi\nu^2} n_0 A_{10} \frac{g_1}{g_0}\left(1 - \exp\left(-\frac{h\nu}{k_B T_s}\right)\right). \tag{4.1.15}$$

Here, we consider the total number of neutral hydrogen atoms $n_\mathrm{HI} = n_0 + n_1$ then,

$$n_\mathrm{HI} = n_1 \times \left(1 + \frac{g_1}{g_0}\exp\left(-\frac{h\nu}{k_B T_s}\right)\right). \tag{4.1.16}$$

In a lots of cace, we can assume $h\nu/k_BT_s \ll 1$ for $\nu = 1420.4057$ MHz, therefore

$$\kappa_\nu = \frac{3hc^2}{32\pi\nu} A_{10} n_{\rm HI} \frac{1}{k_B T_s} \phi(\nu). \tag{4.1.17}$$

In the cosmological context, the differential brightness temperature affected by the expansion of the Universe such that the amplitude of the δT_b emitted from redshift z decrease in proportion to $(1+z)^{-1}$,

$$\delta T_b(z) = \frac{T_s(z) - T_{\rm CMB(z)}}{1+z}(1 - e^{-\tau(z)}). \tag{4.1.18}$$

In general, the line profile has a shape broadening around $\nu = 1420$ MHz due to the velocities which HI clouds have. In the context, the most contribution to the $21cm$ signal comes from the Inter-Galactic-Medium (IGM) which is assumed to expand with the Hubble flow. Then the broadening of the line profile can be expressed by the Hubble velocity such that $\phi(\nu) \approx 1/\Delta\nu \approx c/\Delta V\nu$ with $\Delta V = (dv_{p,\parallel}/dr + H(z))\Delta r$ where $v_{p,\parallel}$ is a peculiar velocity along the line of sight. Based on the above discussion, we will obtain the formula of the differential brightness temperature as a cosmological signal,

$$\delta T_b(z) = \frac{3c^3}{32\pi} \frac{A_{10}h}{k_B\nu^2} \frac{n_{\rm HI}}{(1+z)(dV/dr)} \left(1 - \frac{T_{\rm CMB(z)}}{T_s(z)}\right). \tag{4.1.19}$$

Because of the factor of $(1 - T_{\rm CMB}/T_s)$, the differential brightness temperature is observed as an emission or an absorption line whether the spin temperature is larger than the CMB temperature. In the next section, we briefly review the behavior of the signal according to the redshifts.

4.2 Evolution of the brightness temperature

So far there are plenty of studies of the global signal of $\delta T_b(z)$. Since there is a factor of $(1 - T_{\rm CMB}/T_s)$, the signal can be observed differently depending on the magnitude relation between the spin temperature and CMB temperature. The spin temperature is determined by interactions with the CMB photons, collision with baryonic particles, scattering of the background high energy photons (UV background) (Field, 1958; Furlanetto et al., 2006).

Assuming that the HI atoms are in the equilibrium of these interactions, we find the relation,

$$n_1(C_{10} + P_{10} + A_{10} + B_{10}T_{\mathrm{CMB}}) = n_0(C_{01} + P_{01} + A_{01} + B_{01}T_{\mathrm{CMB}}), \tag{4.2.1}$$

where C_{01} and C_{10} are excitation and de-excitation rates of the collision, P_{10} and P_{01} are also excitation and de-excitation rates but of the scattering of the UV background. The excitation and de-excitation rates have a relation

$$\frac{C_{01}}{C_{10}} = \frac{g_1}{g_0} \exp\left(-\frac{T_*}{T_K}\right). \tag{4.2.2}$$

where T_* is the temperature corresponding to the energy gap in the fine structure, $T_* = h\nu/k_B = 0.068\mathrm{K}$ and T_K is the kinetic temperature of the gas particles. In the same manner, we can treat the excitation and de-excitation rates due to the UV background scattering by defining the color temperature of the UV radiation field, T_C. Then,

$$\frac{P_{01}}{P_{10}} = \frac{g_1}{g_0} \exp\left(-\frac{T_*}{T_C}\right). \tag{4.2.3}$$

Considering the Rayleigh-Jeans limit, the intensity of the CMB is in proportion to the temperature T_{CMB},

$$I_{\mathrm{CMB}} = \frac{2h\nu^2}{c^2} k_B T_{\mathrm{CMB}}. \tag{4.2.4}$$

Using the relations between Einstein coefficients in equation (4.1.11), we obtain

$$\exp\left(-\frac{T_*}{T_s}\right) = \frac{C_{10}\exp\left(-\frac{T_*}{T_K}\right) + P_{10}\exp\left(-\frac{T_*}{T_C}\right) + A_{10}\frac{T_\gamma}{T_*}}{C_{10} + P_{10} + A_{10}\left(1 + \frac{T_\gamma}{T_*}\right)}. \tag{4.2.5}$$

In most case it seems to be reasonable to assume $T_* << T_K, T_C$ and T_γ, we can expand the exponential and defining the coupling coefficients as

$$y_K = \frac{C_{10}}{A_{10}}\frac{T_*}{T_\gamma}, \quad y_C = \frac{P_{10}}{A_{10}}\frac{T_*}{T_\gamma}, \tag{4.2.6}$$

we finally get the formula of the spin temperature

$$T_s^{-1} = \frac{T_{\rm CMB}^{-1} + y_{\rm K} T_{\rm K}^{-1} + y_C T_C^{-1}}{1 + y_{\rm K} + y_C}, \tag{4.2.7}$$

Those temperatures and the coupling coefficients evolve with time, so that the behavior of the signal can be separated into some stages (Furlanetto et al., 2006; Mesinger et al., 2011). We summarize the behavior of the global signal of the brightness temperature as below.

Collisional coupling; $100 \leq z$**:** $T_{\mathbf{K}} = T_s \leq T_{\mathbf{CMB}}$

After the recombination of the CMB photons and electrons, the collisions of hydrogens each other occurred most frequently. Then the spin temperature coupled with the gas temperature which decreased in proportion to $(1+z)^2$ while the CMB temperature decreases as $(1+z)$. Thus the differential brightness temperature would be observed as an absorption line.

Collisional decoupling; $35 \leq z \leq 100$**:** $T_{\mathbf{K}} < T_s < T_{\mathbf{CMB}}$

Due to the expansion of the Universe, the number density of baryons in the IGMs declined. Therefore, in this epoch, the collisions of hydrogens each other become less often and the spin temperature coupled with the CMB photons and it would come up with the CMB temperature.

After collisional decoupling $\rightarrow$ **Wouthuysen-Field Coupling;** $25 \leq z \leq 35$**:**
$T_{\mathbf{K}} < T_s \simeq T_{\mathbf{CMB}} \rightarrow T_{\mathbf{K}} \simeq T_s < T_{\mathbf{CMB}}$

After decoupling hydrogens each other, the spin temperature decouples from the kinematic temperature. Then the spin temperature and the CMB temperature almost the same until the first stars appear. When the first stars come into existence, the emission of the Ly-α photons from the first stars interact the HI gas and the spin temperature couples with the kinetic temperature again, which is called Wouthuysen-Field effect (Wouthuysen, 1952; Field, 1958).

X-ray heating transition; $16 \leq z \leq 25$**:** $T_{\mathbf{K}} = T_s > T_{\mathbf{CMB}}$

Since the spin temperature tightly couples with the kinetic temperature due to the WF effect, it decreases as the Universe expands. However, x-rays from the stars heat the IGM gas and the spin temperature starts to rise. At this epoch, the kinetic temperature of the IGM, as well as the spin temperature become over the CMB temperature, so that δT_b would be observed as the emission line.

Figure 4.1: An artistic image of the SKA1-MID dishes in South Africa.This picture is taken from "https://www.skatelescope.org/the-ska-project/"

Reionization → Present; $z \leq 16$**:** $T_{\mathbf{K}} = T_s \gg T_{\mathbf{CMB}}$

Once the x-ray heat the IGM enough, the spin temperature is so larger than the CMB temperature that the differential brightness temperature does not depend on this temperature. Furthermore, when the deionization starts due to the high energy photon emitted from the first generation stars or galaxies, the ionized regions begin to increase. Thus the amount of the neutral hydrogen diminishes so that the amplitude of δT_b becomes small.

4.3 HI intensity mapping survey in the SKA era

The large scale galaxy surveys have revealed the astonishing large scale structures in the Universe (Seldner et al., 1977; Gregory & Thompson, 1978; Jõeveer et al., 1978; de Lapparent et al., 1986; Geller et al., 1987; Colless, 1998; York et al., 2000; Dawson et al., 2013). On the other hand, tracing the emission from the neutral hydrogen, namely the 21cm line, with a significant survey volume is ongoing.

The HI intensity mapping survey is a technique to trace the line emission of HI following the distribution of matter by not demanding to resolve the location of a point source of the emission (Bharadwaj et al., 2001). Since we know the redshift dependence of the observed HI signal, the time consumption to determine the redshift of the emission field is much less

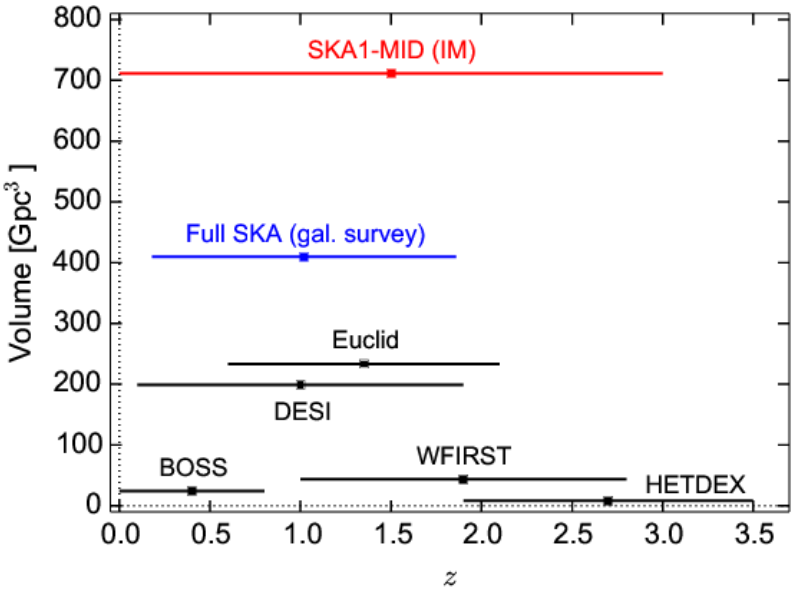

Figure 4.2: The expected survey volumes by the SKA1-MID intensity mapping survey and HI galaxy survey as well as other galaxy surveys are shown. Each survey volume is calculated at the redshift centers. We can see that the HI intensity mapping survey conducted by the SKA has huge potential to trace the large scale matter distribution. This figure is adopted from Santos et al. (2015)

compared to the determination in galaxy surveys. Because of the traceability of the redshifts, we can construct 3D pixels of the intensity fields which will enable us to trace the fluctuation in the intensity field as a biased matter density field.

The Square Kilometre Array (SKA) is an international collaboration to build a next-generation radio observatory. The SKA will consist of two telescopes of a dish array (SKA-MID) in South Africa and an array of dipole antennas (SKA-LOW) in Australia. The project is separated into two phases as SKA1 and SKA2, the former is planned to begin its operation in 2020, while the latter about in 2025.

For the SKA1-MID, according to Square Kilometre Array Cosmology Science Working Group et al. (2018), the adopted design baseline is that it consists of 133 dish arrays with a dish diameter of 15m, which will provide angular resolution of 0.3 arcmin at 1.4GHz. The SKA1-MID is planned to use 5 different frequency bands among which the most cosmology relevant are band 1 and band2, especially for band1 the target frequency and redshift are $0.35\text{GHz} < \nu < 1.05\text{GHz}$ and $0.35 < z < 3$ respectively. The wide band1 survey of the SKA1-MID will cover 20,000deg^2 of the sky and about 10,000hours will be planned.

One of the main targets for the HI intensity mapping survey is to detect the Baryon

Acoustic Oscillation (BAO) with a very large scale survey. The measurement of the BAO is, as mentioned, one of the probes of the nature of dark energy since the measurement of it with different redshifts provide a strong constraint on the expansion history of the universe through the angular diameter distance and the Hubble parameter, which is very affected by the energy budget of dark energy and its equation of state.

For the conventional galaxy survey, it has been detected the peak scale of the BAO in the galaxy distributions Eisenstein et al. (2005); Beutler et al. (2011); Cuesta et al. (2016). The distribution of galaxies in the Universe is very distinct, such that we see that it would trace the underlying matter distribution. However, the determination of the redshift of each galaxy is much time expensive so that obtaining the large scale distribution of galaxy needs much time. Also, the large scale distribution of galaxies has a limitation in the radial direction since it can not be observed as long as they exist in principle.

On the other hand in terms of the survey volume for HI , it is expected to overwhelm the galaxy surveys by not only the sly coverage but also redshift. In Figure 4.2, we show the expected survey volume conducted by the SKA as well as future galaxy surveys such as BOSS (Eisenstein, 2015), DESI (DESI Collaboration et al., 2016), Euclid (Racca et al., 2016), WFIRST (Kruk, 2019), HETDEX(Adams et al., 2011). The Figure is adopted from Santos et al. (2015).

As shown in Figure 4.2, the SKA intensity mapping survey will trace the huge distribution of neutral hydrogen as a biased tracer of dark matter, which will provide not only the detection of BAO but also the property of cosmic voids. As mentioned in the previous Chapter, It is important to have much more void samples to succeed in the Alcock-Paczynski test with the shape of cosmic voids. We consider that the future HI intensity mapping survey will open the window of void statistics as well. In the next chapter, we will investigate the possibility to apply voids in the intensity map to the Alcock-Paczynski test.

Chapter 5

Alcock Paczynski test with stacked voids in HI intensity mapping

In this chapter, we are going to investigate the possibility of the Alcock-Paczynski test with stacked void in the HI intensity mapping survey. First, we would like to introduce how we construct the mock HI intensity map and then we will explain the method to detect void structure with a particle base void finding algorithm. We analyze the average shape pf voids and practice the AP test and obtain the density parameter estimation. We finally discuss the effect of peculiar velocities and observation resolution.

5.1 Mock HI map

In order to investigate the possibility of the AP test with void stacking technique to the future HI intensity popping survey, we examine our procedure by using hydrodynamical simulation data. In this work, we have adopted the IllustrisTNG simulation which is the state of the art cosmological simulation of the matter dynamics (Pillepich et al., 2018; Naiman et al., 2018; Springel et al., 2018; Nelson et al., 2018; Marinacci et al., 2018; Nelson et al., 2019). Since the simulation data include physical valuables of the baryonic components, we can produce the mock intensity map based on the simulation results. In this section, we will show our procedure to make mock maps.

Spin temperature

In Section 4.2, we have explained that the spin temperature is determined by the coupling with the CMB temperature, the kinetic temperature of the IGM gas and the color temperature of the UV background photons as equation (4.2.7), where the coupling coefficient y_K is described

interns of the number density of the baryonic particle,

$$y_K = \frac{T_*}{A_{10}T_\gamma}\left(\kappa n_{\rm HI} + \kappa_{\rm p} n_{\rm p} + \kappa_{\rm e} n_{\rm e}\right), \tag{5.1.1}$$

where n_H, n_p and n_e are the number density of hydrogen atom, proton and electron, κ_H, κ_p and κ_e are the de-excitation rates in collisions with hydrogen atoms, protons and electrons respectively. These de-excitation has been calculated by previous works, and we follow the same manner as Kuhlen et al. (2006). For the collision with hydrogen atoms, Allison & Dalgarno (1969); Zygelman (2005) calculated the de-excitation rates which is fitted by

$$\frac{\kappa_{\rm HI}}{[{\rm cm^3 s^{-1}}]} = 3.1\times10^{-11} T_{\rm K}^{0.357}\exp\left(-\frac{-32}{T_{\rm K}}\right). \tag{5.1.2}$$

For the collision with electrons Liszt (2001) provided a fitting formula,

$$\frac{\kappa_{\rm e}}{[{\rm cm^3 s^{-1}}]} = \begin{cases} 10^{-9.607+0.5\log(T_{\rm K})\exp\left(-(\log T_{\rm K})^{4.5}/1800\right)} & (T_{\rm K}\leq 10^4), \\ \kappa_{\rm e}(T_{\rm K}=10^4[K]) & (T_{\rm K}>10^4). \end{cases} \tag{5.1.3}$$

For collision with protons, the rate is obtained by multiplying κ_H by 3.2 (Smith, 1966), so that

$$\frac{\kappa_{\rm p}}{[{\rm cm^3 s^{-1}}]} = 3.2\kappa_{\rm HI}\,. \tag{5.1.4}$$

The coupling coefficient y_C is determined by the process known as the Wouthuysen - Field effect (Wouthuysen, 1952; Field, 1958). This process tells us the possible transition that the hydrogen in the ground state (n=1) jumps to the next above energy level (n=2) by absorbing the Ly-α photon and then emitting Ly-α photon

The coupling coefficient y_C is written (Furlanetto et al., 2006)

$$y_C = S_\alpha \frac{J_\alpha}{J_\nu^c}, \tag{5.1.5}$$

where J_α is the flux at Ly-α frequency, $J_\nu^c = 1.165\times10^{-10}[(1+z)/20)]{\rm cm^{-2}s^{-1}Hz^{-1}sr^{-1}}$ and

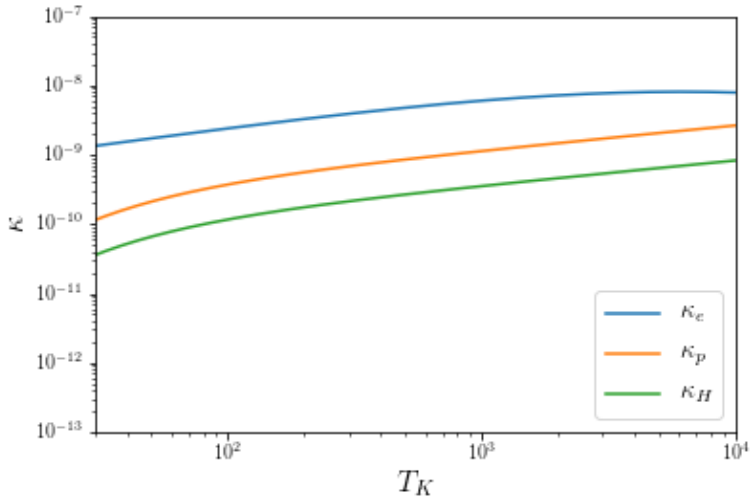

Figure 5.1: Collisional rates as a function of the gas temperature. As expected, the collisional rates become large when the gas temperature is high.

S_α is a correction factor which is approximated as

$$S_\alpha \sim \exp\left[-0.803 T_{\rm K} - -2/3 \left(\frac{10^{-6}}{\gamma}\right)^{1/3}\right]. \tag{5.1.6}$$

γ is the inverse Gunn-Perterson optical depth, which is defined by

$$\gamma = \tau_{\rm GP}^{-1} = \frac{H(z)\nu_\alpha}{\chi_\alpha n_{\rm HI}\, c}. \tag{5.1.7}$$

where $\chi_\alpha = \frac{\pi e^2}{m_e c} f_\alpha$, $f_\alpha = 0.4162$ is the oscillator strength of the Ly-α transition. Those coupling coefficients include the number density of hydrogen gas, proton, and electron. In order to calculate those values, we adopted the Cloud-in-Cell scheme to translate the particle-based data into the grid-based data. The simulation box divided into 256^3 grids.

In Figure 5.2 we show example maps of dark matter distribution and 21cm intensity fields. In the left panels of Figure 5.2, we show the dark matter distribution in the IllustrisTNG simulation, while in the right panels we illustrate the 21cm intensity fields by the procedure described above. The top panels show the snapshot at $z = 3$, the bottoms are $z = 0$. We can see rich structures and their evolutions in the dark matter distributions such as voids, filaments, and halos. For the right panels, we can also see the similar structures found in the

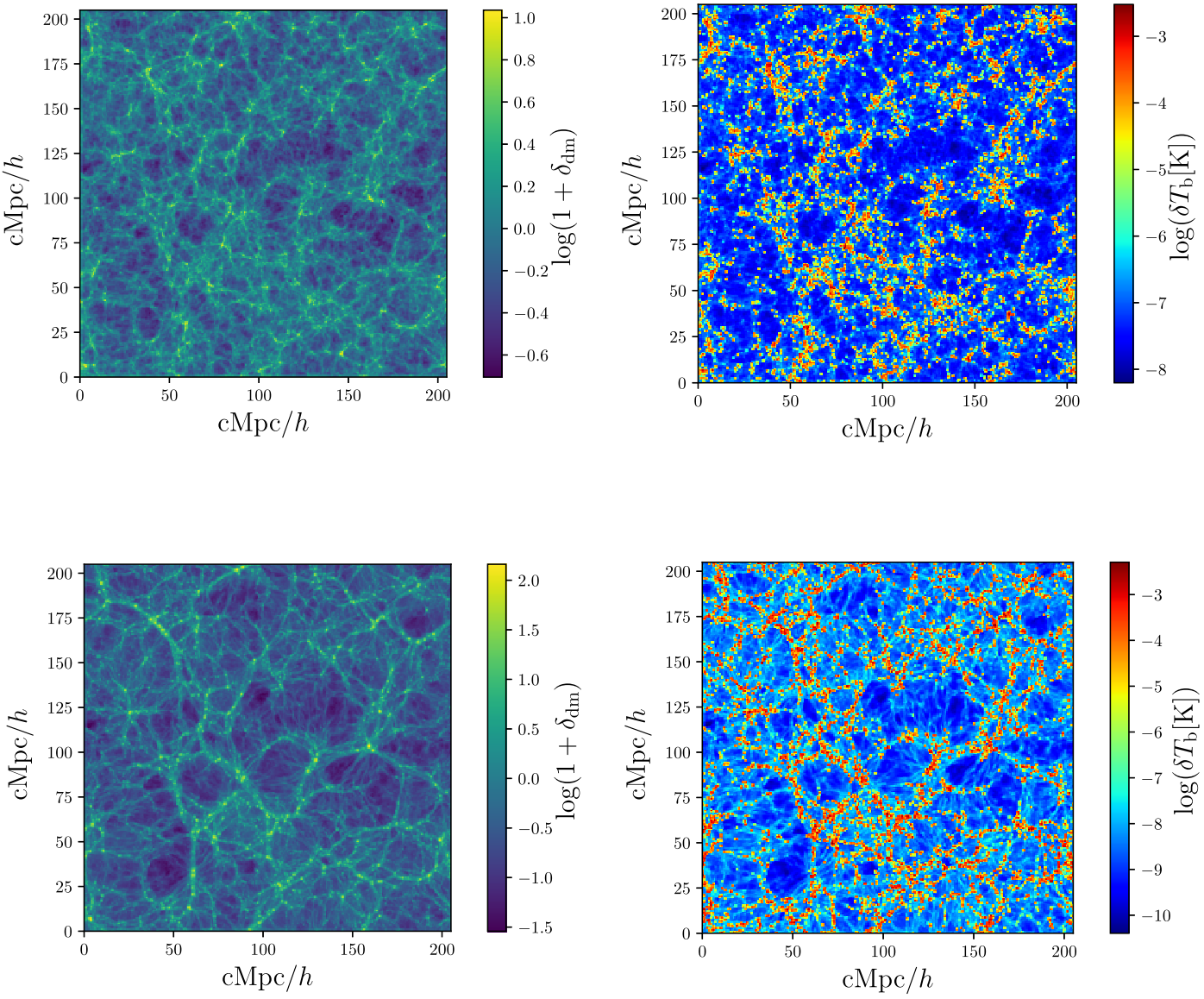

Figure 5.2: Dark matter density field (left panels) and the intensity map of the 21cm line(right panels). The top panels are the snapshots at $z = 3$ while the bottom panels are $z = 0$. In the dark matter distribution, we can see rich structures such as voids, filaments, and halos. On the other hand, the intensity fields traces the dark matter structures.

dark matter distributions, so as our expectation, the emission of the neutral hydrogen is a good tracer of the large scale structures.

We note that what we would like to achieve is to identify voids from the intensity map and conduct the AP test with stacked voids. However, it also should be noted that the AP test demands statistical isotropic objects. From this point of view, we do not care about what the structure exactly is. So we expand our aim that we would like to conduct the AP test with intensity contour surface surrounding cosmic voids. Similar to voids in the galaxy survey map, we can assume that voids in the 21cm intensity contour map are statistically spherical according to the cosmic principle.

In Figure 5.3, we show the original intensity map and the contour maps by separating regions whether the intensity is larger or not than the thresholds. In this figure, we vary the threshold value from $0.01, 0.1, 1$ and 10 times the averaged intensity for the middle left, middle right, bottom left and bottom right panels respectively. We see that different contour levels draw different pictures of the structures. For low contour levels, we can surely distinguish the void structures while some possible void regions are painted out. On the other hand, for a higher contour level, the structures seem faint, so that the shape of voids is ambiguous.

5.2 Void finding in the HI intensity map

As we have already mentioned our aim is to investigate the possibility of the AP test in the future HI intensity mapping survey with the void stacking technique. We have adopted publically available code "VIDE" (The Void IDentification and Examination toolkit) in order to find void structure in the mock intensity maps produced from the IllustrisTNG simulation. We first explain how VIDE finds voids. The core component of VIDE is ZOBOV (Neyrinck, 2008) which finds void structure based on the Voronoi tessellation (van de Weygaert & Schaap, 2009) and watershed algorithm (Platen et al., 2007). The example procedure is in Figure 5.4 which is adopted from Neyrinck (2008)

ZOBOV first does the Voronoi tessellation on the particle distribution to estimate the density of each particle position which is illustrated on the top right panel in Figure 5.4. In the panel, each Voronoi cell is colored according to its volume or density. In the panel, the lower the density is the darker the color is. After the Voronoi tessellation of the space, ZOVOV finds local minima density cell which is not adjacent to lower density cells than themselves. Then, ZOBOV ties the local minimum cells with the next cells to them and repeat this process until the density of the tied cells reaches the density edge. The locally maximum cells are tied with the lowest density cells among their neighbors. This process is called zoning and each grouped cells are called zones, the result of this process is shown in the lower-left panel

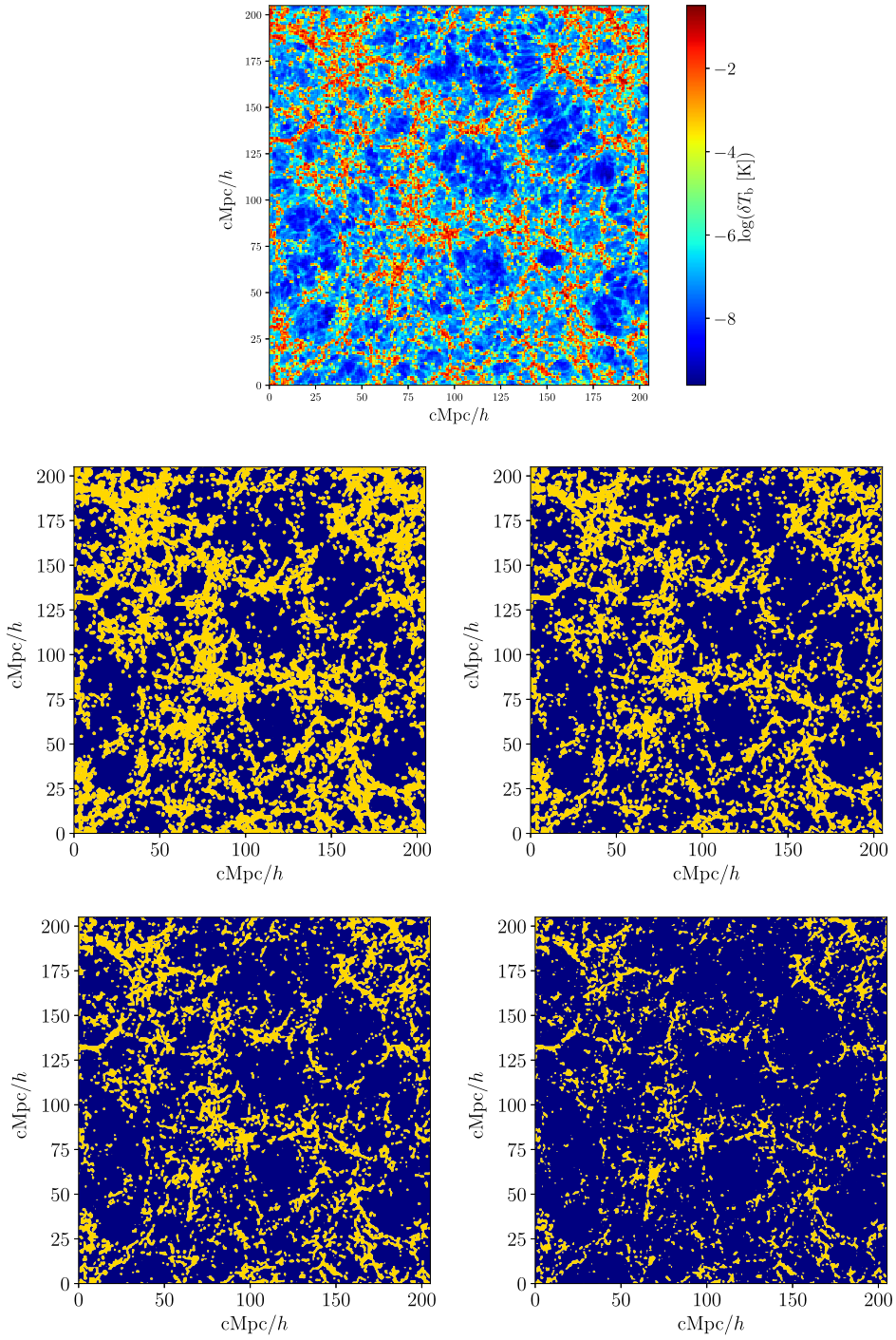

Figure 5.3: The intensity map and its contour maps. The top panel indicate the original intensity map while the middle and bottom panels are intensity contour maps made from the top panel. In the contour maps, each region is distinguished by the colors such that if the brightness temperature is larger than the contour threshold, it is painted as a bright color while if the brightness temperature is below the threshold, it is colored as dark. Therefore we can regard the dark regions as void regions. Here we very the contour levels as $0.01, 0.1, 1$ and 10 times average intensity for the middle left, middle right, bottom left and bottom right panels respectively.

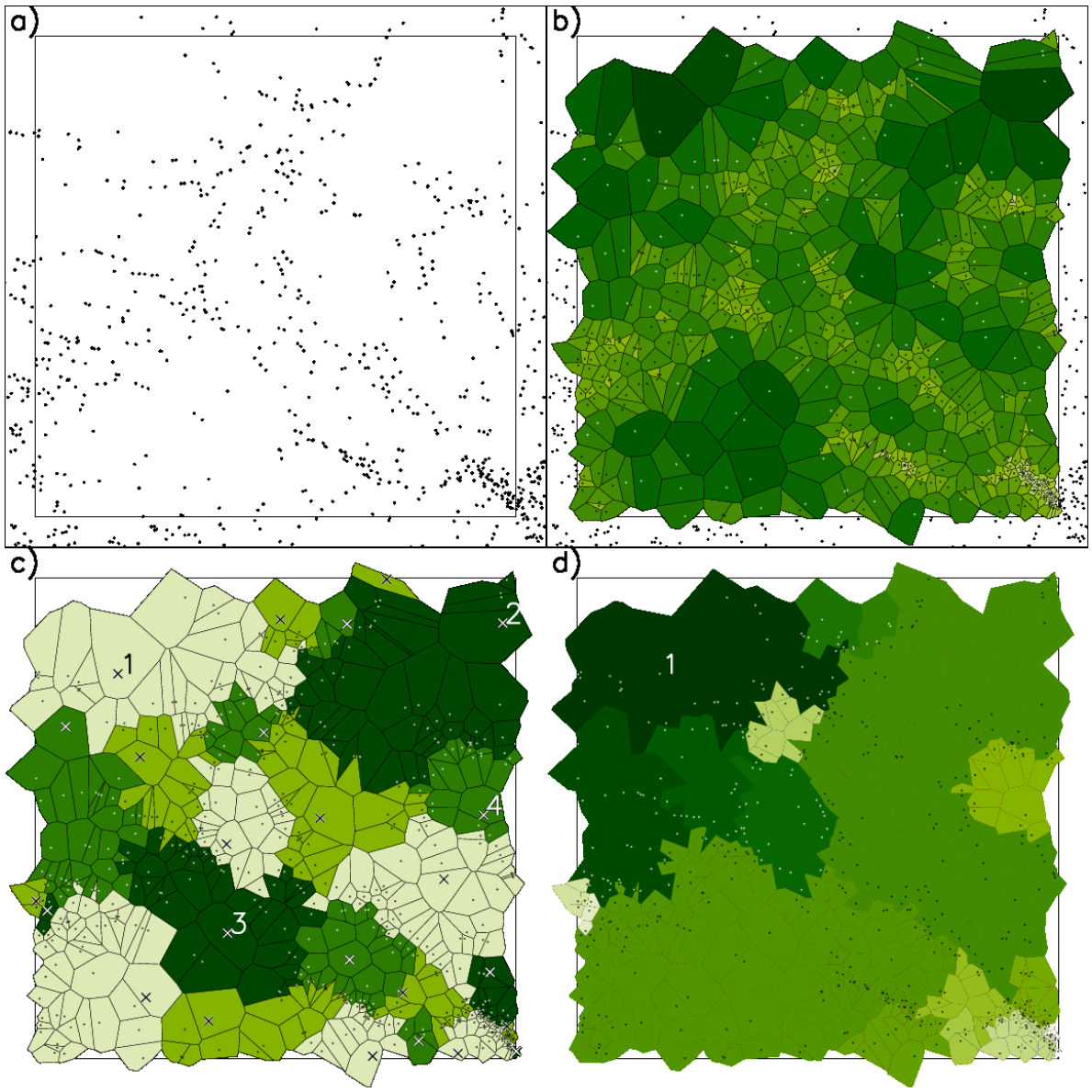

Figure 5.4: An example of the Voronoi tessellation and watershed method to find void structures, adopted from Neyrinck (2008). On the top left panel, the particle distribution is illustrated. The first step of void finding by ZOBOV is to conduct the Voronoi tessellation on the particle distribution, which is illustrated on the top right panel. On the top right panel, each Voronoi cell is colored according to their volume (density). By zoning the Voronoi cells, ZOBOV finds primitive voids that are called zones as shown on the bottom-left panel. The final step is to gather each zone if its boundary is not above a threshold. After jointing zones, ZOBOV reports voids as the final groups of the Voronoi cells, shown on the lower right panel.

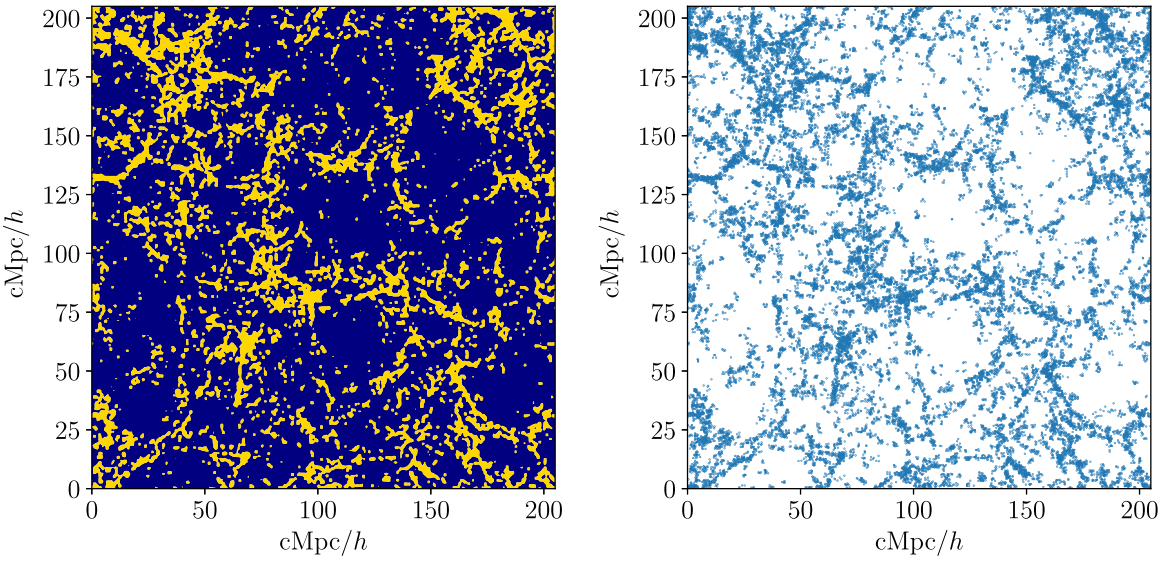

Figure 5.5: The example mock particle distribution (right) made from the left panel. We put a particle if the intensity of the region is above the averaged value. The distribution of particles reasonably trace the shape of voids.

in Figure 5.4.

The final step of ZOBOV is to joint the zones into voids. We note that each zone is a primitively void, but if the density of their boundary cells is not high, those voids can be regarded as one void. By default setup, VIDE reports every pattern of voids, in other words, VIDE provide voids as resulting in joining zones as well as zones themselves if the size of zones are larger than that of our demands since zones are in principle primitive voids.

As described above, VIDE identifies voids in particle distributions while what we are going to do is to find contour surface surrounding voids in 21cm intensity fields. Hereafter we would like to introduce our method to produce a particle distribution.

We assume that if $\delta T_{\rm b}$ is large at a position the density of HI or just matter is also large. Then we put a particle if $\delta T_{\rm b}$ is above a threshold. The threshold can take any values in principle, while we have adopted the averaged value for the threshold. Because of the rule to make a particle distribution, the particle distribution does not reflect the real density field since we put a particle both relatively low $\delta T_{\rm b}$ and high $\delta T_{\rm b}$ if both values are above the threshold. Even though our mock particle distribution never reflects the matter density field, it does not matter, since what we want is the shape of voids in the intensity fields. For only this purpose, we consider that the process to make the particle distribution and void finding will work.

We show the example particle distribution from the intensity map data in Figure 5.5. We

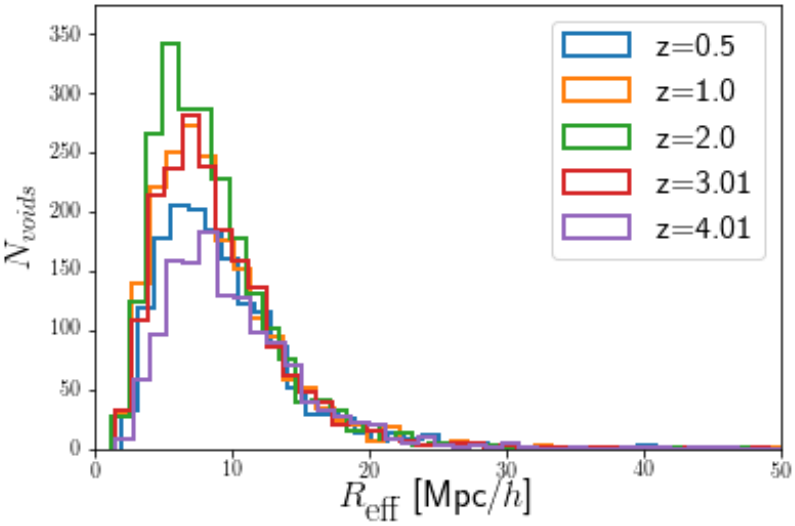

Figure 5.6: The abundance of voids according to their radius. Different colors indicate different redshifts. Our void catalogs show that voids of the radius between 5 Mpc/h and 10 Mpc/h are the most popular in the simulation box. Also The number of voids increases until $z = 2$ because the large scale structure grows while it decrease after the redshift since the marginalize process happens.

can see that the particle distribution reasonably trace the shape of voids surrounded by the average intensity contour. Then we run VIDE to the mock particle distributions made from the intensity maps for $z = 0.5, 1.0, 2.0, 3.01$ and 4.01 respectively. We have obtained voids as shown in Figure 5.6 In the figure, we show the number of voids according to their radius defined as equation (5.3.5) for each redshift. We note that we do not adopt any filtering on voids that VIDE outputs. Therefore, in fact, some voids might be just Poisson noise due to the discrete particle distribution. In the original ZOBOV paper (Neyrinck, 2008), the author suggested a way to distinguish the fake voids by considering the ratio of the density at the center to the density at the ridge of voids. For example, if the ratio r of some voids is more than 1.57, we can regard those voids as true voids with a 2σ confidence level.

However, based on the concept of the AP test, we do not have to care about whether the voids are really "voids" or not. What is important for the test is to observe the isotropic objects and this concept encourages us to use any voids which VIDE provides.

When we see Figure 5.6, we notice that our void populations have peaks at $5[\mathrm{Mpc}/h < R < 10\mathrm{Mpc}/h$. Also, we can see that the number of voids increases until $z = 2.0$ while it decreases toward the present after the redshift. Since the large scale structure grows as time

passes, the void structures also evolve and can be of served more as time flow. However, in the recent epoch, the margin process among voids begins to occur such that the total number of voids will decreases while the voids in the recent epoch recognized as sure voids.

5.3 Void shape in the HI intensity map

In the Alcock-Paczynski test, we measure the shape distortion due to cosmic expansion. What we will observe about the size of a distant object in a survey is the angular and redshift span. To reconstruct the original size of the object, we have to assume a cosmological model as described in equation (3.2.1). If the shape of the object is spherical, we have the relation of equation (3.2.2). Thus, in order to apply the shape of the cosmic voids in the HI intensity mapping survey to the AP test, we need to confirm whether the shape of stacked voids in the HI intensity fields is spherical or not at first. Then we are going to check the physical shape of the staked voids.

Before doing that, we would like to introduce our void stacking process. The stacking is done by setting the position of every void's center at the origin, where the center of a void is defined by the Voronoi cell volume-weighted center,

$$\boldsymbol{x}_c = \frac{\sum_i^{N_p} V_i \boldsymbol{x}_i}{\sum_j^{N_p} V_j}, \tag{5.3.1}$$

where $\boldsymbol{s}_c$ is the position vector of the center of the void, $\boldsymbol{s}_i$ and V_i is the position vector and the volume of the Voronoi cell of the ith particle which is a member of the void and N_p is the number particle included in the void. Thus the position of the particle when the center of the void is set at the origin (or the relative position of the particle from the center of the void) is

$$\delta \boldsymbol{x}_i = \boldsymbol{x}_i - \boldsymbol{x}_c. \tag{5.3.2}$$

Then we define the size of stacked voids along each axis as the second moment of the particle distribution,

$$\Delta x_{\parallel}^2 = \frac{1}{N} \sum_i^N \delta x_{i,3}^2, \tag{5.3.3}$$

$$\Delta x_{\perp}^2 = \frac{1}{N} \sum_i^N \frac{(\delta x_{i,1}^2 + \delta x_{i,2}^2)}{2}, \tag{5.3.4}$$

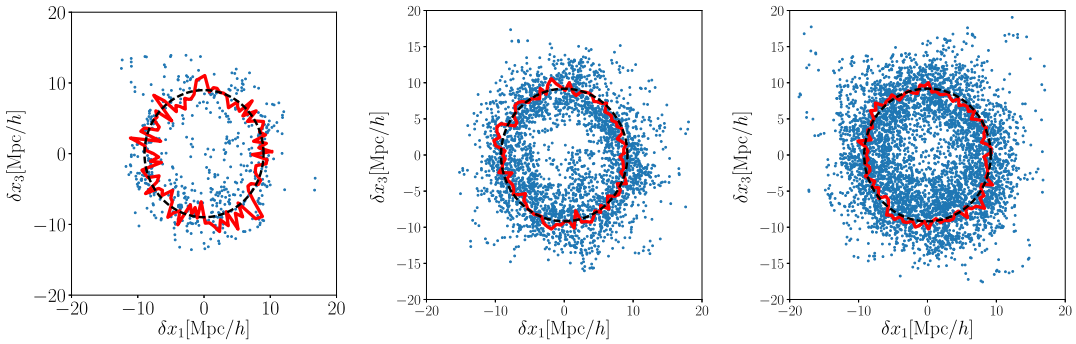

Figure 5.7: An example of 2 dimensional void stacking process. Here we stack voids of the radius $R_{\rm eff} = 10 \pm 5{\rm Mpc}/h$. Both axes show the relative position of the particles from the center of voids. From left to right panels, the numbers of voids for the stacking are $10, 50$ and 100 respectively. The red solid lines in each panel show the averaged radial positions of the particles within an azimuthal bin. The black dashed lines are the reference circles whose radii correspond to the averaged radial position of all particles. One can see that the shape of stacked void seems to be more spherical when the number of voids for stacking becomes large.

where N is the number of total particles which are stacked and we suppose the third axis of the simulation data as the line of sight and the first and second axises as the angular direction.

We stack voids within the narrow radius bin like $R_{\rm eff} \pm 0.5{\rm Mpc}/h$, where the effective void radius is determined by the volume of it,

$$R_{\rm eff} \equiv \left(\frac{3}{4\pi} V \right)^{1/3} . \tag{5.3.5}$$

where V is the volume of the void.

In Figure 5.7, we show the shape convergence of the 2D stacked voids. The numbers of voids to be stacked are 10, 50, and 100 from the left to the right panels, respectively. The dots indicate relative positions of the void particles. Here, we have stacked voids of the radius of $10 \pm 0.5{\rm Mpc}/h$. The red solid lines show the averaged positions of the particles within azimuthal bins, while the black dashed lines represent the reference circles. One can see that the red line in the left panel is fluctuating along the black circle, which indicates that if the number of voids for stacking is not enough, the shape of the stacked voids is ambiguous. On the other hand, if the number of voids to be stacked is large, the red line converges towards the black circle as in the right panel. Thus, our hypothesis that the shape of stacked voids found in the intensity map is spherical is correct when we stack the enough number of voids. In Figure 5.8, we show the ratio between $\Delta x_{\parallel}$ and $\Delta x_{\perp}$ for stacked voids

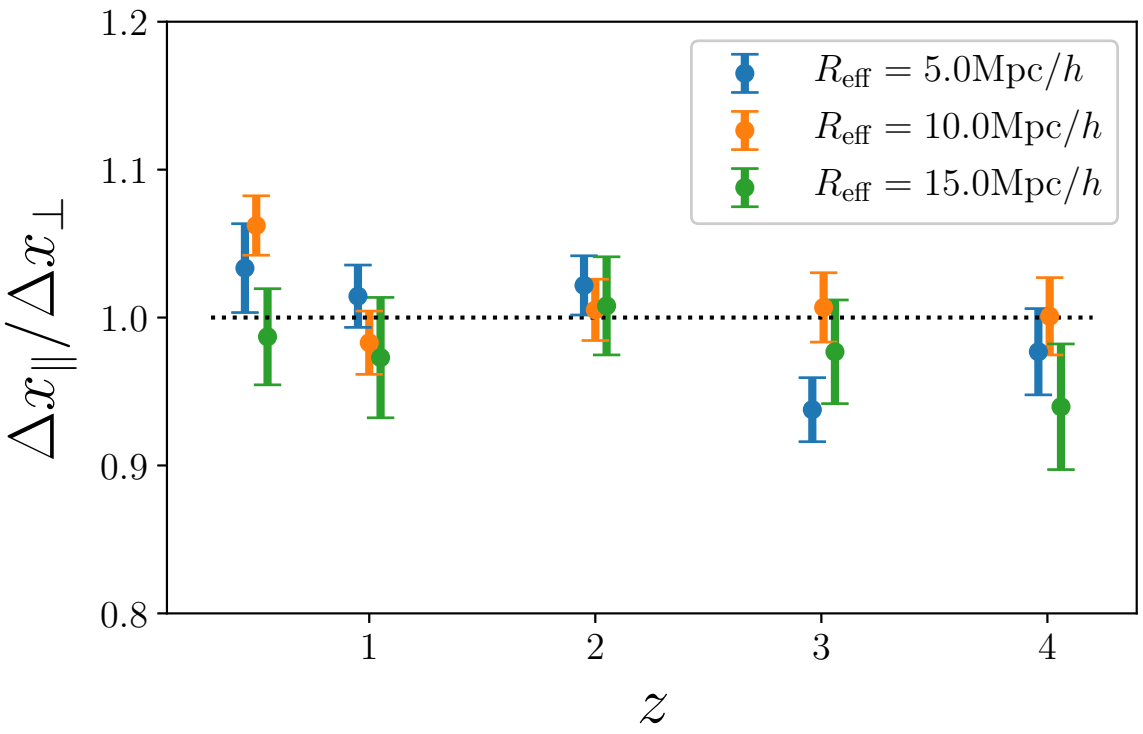

Figure 5.8: Top: The normalized AP signal of stacked HI voids, where $e^{\rm fid}$ is calculated by adopting fiducial cosmological parameters adopted in the IllustrisTNG simulation. The error bars show the 1-σ confidence regions around the data points. One can see that the normalized signals are consistent with unity which suggests that the shape of the stacked void is spherical. It seems that this property does not depend on the redshift and the size of the stacked void.

of the radii with $R_{\rm eff}$ = 5,10,and 15Mpc/h at $z = 0.5, 1, 2, 3$, and 4. Since we have only one realization simulation data, we evaluate the variance of the shape measurement by means of the bootstrap method. We reconstruct mock catalogs by sampling the same number of voids in a radius bin from the original catalog has. In the sampling process, we allow overlapping voids. By the above process, we produce 100 mock catalogs and calculate the size ratio of stacked voids for each catalog, and evaluate the mean value and variance among the catalogs. One can see that the ratios are consistent with unity, which also indicates that the shape of stacked voids is spherical. We have confirmed that this trend does not depend on the void size and redshift so that we can perform the AP test by using the stacked voids in the HI intensity map.

We note that in the future intensity mapping survey conducted by SKA1-MID, we will observe $20,000\mathrm{deg}^2$ of the sky. This corresponds to $20, 61, 149, 225$ and 286 time as large as the IllustrisTNG-3 simulation size for $z = 0.5, 1.2, 3$ and 4 respectively. Thus, if we obtain a similar intensity map from the actual observation to our simulation, the error bars are reduced by at least $1/\sqrt{20}$ if noise-free situation. We note, however, for making the simulation map, we do not include any contaminations such as the resolution effect, noise, foreground and so on. Even though it is possible to obtain a different result from this study in the real observation, one of our aims is to investigate the possibility of the application of the test to the HI intensity mapping survey, we conduct the AP test with our signals.

5.4 Performing the AP test

In the previous section, we confirm that the averaged shape of voids in the HI intensity field becomes spherical when we stack enough number of voids. Now we are going to consider performing the AP test by using the shape of stacked voids. Here we adopt the Markov Chain Monte Carlo (MCMC) method to estimate the cosmological parameters. In this method, we calculate the probability distribution of the parameters based on the Bayes's theorem,

$$P'(\boldsymbol{p}|\boldsymbol{e}) = \frac{P(\boldsymbol{p})L(\boldsymbol{e}|\boldsymbol{p})}{\int P(\boldsymbol{p}')L(\boldsymbol{e}|\boldsymbol{p}')d\boldsymbol{p}'}, \tag{5.4.1}$$

where $\boldsymbol{p}$ and $\boldsymbol{e}$ are a set of model parameters and observation data, $L(\boldsymbol{e}|\boldsymbol{p})$ is a probability to obtain the data $\boldsymbol{e}$ when the parameters are $\boldsymbol{p}$, which corresponds to the likelihood. $P(\boldsymbol{p})$ and $P'(\boldsymbol{p}|\boldsymbol{e})$ are called prior distribution and posterior distribution respectively. The latter is the probability distribution of the parameter set after getting the data, which is what we want here.

When we assume that the probability of the observation data follows the Gaussian distribution, the likelihood of this measurement is given by

$$L(\boldsymbol{e}|\boldsymbol{p}) = \prod_{i,j} \frac{1}{\sqrt{2\pi\sigma_{i,j}^2}} \exp\left[-\frac{\left(e_{i,j}^{\rm data} - e_i\right)^2}{2\sigma_i^2}\right], \tag{5.4.2}$$

where $e_{i,j}^{\rm data}$ and $\sigma_{i,j}^2$ are the observation data and the variance of the data, $e_i(\boldsymbol{p})$ is the theoretical value determined by the model parameters. Here the observation data can be produced by the relation of observable and the physical size in equation (3.2.1) as

$$e_{i,j} \equiv \left.\frac{\Delta z}{z\Delta\theta}\right|_{i,j} = \frac{\chi H(z_i, \Omega_{\rm fid}, w_{\rm fid})}{cz_i} \cdot \left.\frac{\Delta x_\parallel}{\Delta x_\perp}\right|_{i,j}, \tag{5.4.3}$$

where the subscript i and j are the index of redshift and the stacked void radius. The theoretical value of the AP signal can be obtained by assuming $\Delta x_\parallel = \Delta x_\perp$, namely

$$e_i(\boldsymbol{p}) \equiv \frac{\Delta z}{z\Delta\theta} = \frac{\chi H(z_i, \Omega, w)}{cz}. \tag{5.4.4}$$

As described above equation, our model parameters here are matter density parameter and the equation of state parameter of dark energy, which appear in the Friedmann equation (2.1.4). For the prior distributions of them, we assume a step function such as

$$P(\Omega_m) = \begin{cases} 1 & (0 \leq \Omega_{\rm m} \leq 1), \\ 0 & (\text{otherwise}). \end{cases}, \tag{5.4.5}$$

$$P(w) = \begin{cases} 1 & (w \leq -\frac{1}{3}), \\ 0 & (\text{otherwise}). \end{cases} \tag{5.4.6}$$

In Figure 5.9, we show the parameter estimation result by the MCMC analysis. For MCMC calculation, we utilize a python module called EMCEE (Foreman-Mackey et al., 2013). In the figure, two circles in the contour map indicate 1σ and 2σ confidence region of the estimation. On the other hand, the vertical lines in the one-dimensional estimation show the 1σ confidence region. The blue solid lines show the fiducial values of the parameters, which are $\Omega = 0.3089$ and $w = -1.0$. We can see that the estimation of the parameters is consistent with the fiducial values by the 1σ confidence level. The result of the estimation of the two parameters

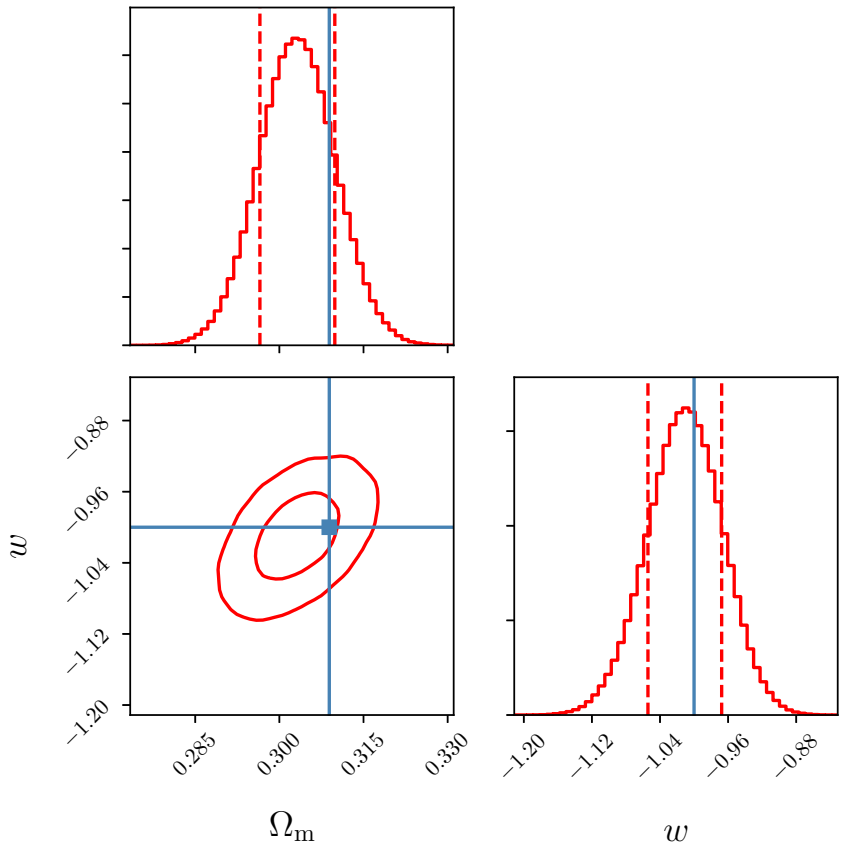

Figure 5.9: Parameters estimation by MCMC sampling. The contour map shows 1σ and 2σ confidence regions while dashed vertical lines in the one dimensional estimation indicate 1σ confidence regions. The blue solid lines show the fiducial values of each parameter, for which we assume the ΛCDM model as a fiducial model. The estimation is consistent with the fiducial values by the 1σ confidence level. The results are $\Omega = 0.3030^{+0.0068}_{-0.0069}$ and $w = -1.011^{+0.043}_{-0.044}$.

are $\Omega = 0.3030^{+0.0068}_{-0.0069}$ and $w = -1.011^{+0.043}_{-0.044}$. This result suggests that the AP test in the intensity map with the stacked void method can be possible in principle.

5.5 Redshift space distortion effect

So far we have investigated the possibility of the AP test with stacked voids surrounded by the HI intensity contour surface and we confirmed that the averaged shape of the voids is spherical so that we can estimate the cosmological parameters by measuring the shape distortion of the voids due to the expansion of the Universe as Figure 5.9. Even though the AP test can be achieved by the procedure we have proposed in principle, there is a big problem in the test, that is to say, the redshift-space-distortion (RSD). This distortion is caused by the peculiar velocities of the objects along the line of sight. The observed redshift of the objects includes the effect of cosmological expansion as well as the Doppler shift due to the motions along the line of sight,

$$z_{\rm obs} = \bar{z} + \frac{v_\parallel - v_{0,\parallel}}{ca}, \tag{5.5.1}$$

where $v_\parallel$ and $v0, \parallel$ are the peculiar velocities of the objects and observers along the line of sight, respectively. $\bar{z}$ represents the redshift due to the expansion of the Universe. Then, the comoving distance to the object is

$$s_\parallel = \int_0^{z_{\rm obs}} \frac{cdz}{H(z)} = x_\parallel(\bar{z}) + \frac{v_\parallel - v_{0,\parallel}}{aH}. \tag{5.5.2}$$

Thus, the observed positions of the objects would be different by the effect of the peculiar velocities. In the HI intensity mapping surveys, we observe the redshifted 21cm lines, which, of course, include the effect of peculiar velocities, and then the estimated positions of the HI gas are also distorted compared to the one with no peculiar velocities. This RSD effect causes a systematic error in the AP test, and we should take care of these distortions in order to take the true cosmological expansion history. In the previous studies, the effects of RSD on the stacked void's shape were reported (Lavaux & Wandelt, 2012; Sutter et al., 2014; Mao et al., 2017c). Among those studies, the RSD effect has appeared as a flattening of the void shape along the line of sight.

Here we also would like to investigate its effect on our procedure. In order to introduce

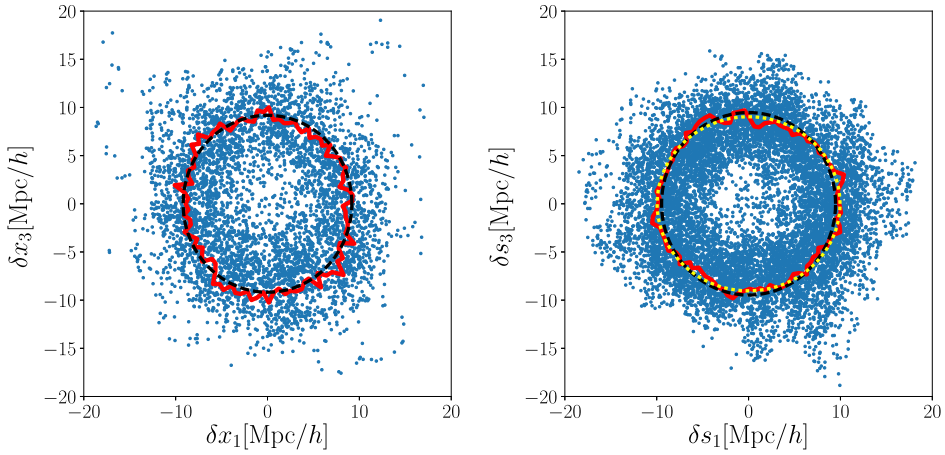

Figure 5.10: A comparison of 2-dimensional stacked void in real-space (left) and redshift-space (right). Here we stack voids of the radius $R_{\rm eff} = 10 \pm 5$Mpc/h. Both axes show the relative position of the particles from the center of voids. For both panels, we stacked 100 voids. The red solid lines and black dashed lines in each panel are the same ones as in Figure 5.7. The yellow dotted line in the right panel indicates an ellipsoid fitted to the void particle positions in redshift-space. One can see that the shape of stacked void in redshift space seems to be squashed along the line of sight.

the effect of peculiar velocities, we shift the gas-cell positions when we make a grid field,

$$s_\parallel = x_\parallel + \frac{(1+z)v_\parallel}{H(z)}, \tag{5.5.3}$$

where $x_\parallel$ and $v_\parallel$ are the position and velocity of a gas cell along the line of sight in the simulation box, and therefore, $s_\parallel$ is the position of the gas cell in the redshift-space. For simplicity, we set the observer's velocity equal to zero.

Then we make mock intensity maps in redshift-space and finds void structure in the same manner as we have conducted in the real-space in which we do not include the effect of the peculiar velocities. Here we again ignore the resolution and noise effects, so that we construct 256^3 grid fields and calculate the brightness temperature.

Figure 5.10 shows the 2D stacked void in real-space (left panel) and redshift-space (right panel). The left panel is the same one in the right panel in Figure 5.7. In the right panel, we notice that the red solid line seems to come into the black dashed circle in the line of sight direction, while the red line goes out the black circle along the horizontal direction. We have fitted the particle positions in the right panel by an ellipsoid, which results in the yellow dotted line in the panel. In this case, the ratio between the major axis and the minor axis

was 0.9075. One can see that the yellow line reasonably traces the red line.

This result indicates that the void shapes in the HI intensity field in redshift-space are squashed along the line on average. This is the same trend as reported in the previous studies with the dark matter or mock galaxy distributions.

In Figure 5.11, we plot the ratio between $\Delta s_{\parallel}/\Delta s_{\perp}$ for several stacked void radii and redshift. Those ratios result in to be less than unity as expected in Figure 5.10. The ratios are about 0.9, which is consistent with the previous works. In the figure, only $R = 15\mathrm{Mpc}/h$ at $z = 4$ deviates from the trend, but we think this is due to the small samples in our catalogs. So if we observe larger volumes and obtain more samples, the signal would be shifted as other signals do.

We can understand this flattening effect in 2 ways. One of them is the elongation of the void ridges along the line of sight, which is so-called the finger-of-god effect. This elongation is caused by the random motions in the clusters. The other one is the Kaiser effect (Kaiser, 1987) which is the large scale coherent motion of clusters. In both cases, the void region is squashed along the line of sight and due to the definition of the stacked void sizes is calculated as the second moment of the mock particle positions around the center of voids in our analysis, the size of the stacked void along the line of sight tends to be flattened in redshift-space. To perform the AP test, we produce the AP signals in the same way described in the previous section but exchanging the size ratio $\Delta x_{\parallel}/\Delta x_{\perp}$ to $\Delta s_{\parallel}/\Delta s_{\perp}$.

To estimate the cosmological parameters correctly, we must remove the effect of peculiar velocities properly, otherwise, we fail to estimate the cosmological parameters. As already mentioned, previous works try to remove the effect by calibrating how much the shape distortion due to the RSD effect appears. For example, Lavaux & Wandelt (2012) proposed that multiplying by 1.16 ± 0.04 is reasonable to restore the sphericity of the stacked void in the dark matter distribution. According to their suggestion, we first try to remove the effect of the peculiar velocity by multiplying a constant. Then, we calibrated the constant to recover the sphericity in our simulation results and found that the stacked voids in the HI intensity fields are squashed by the factor of $0.9071^{+0.0032}_{-0.0031}$ along the line-of-sight direction on average. Thus, we can recover the sphericity of the stacked voids by multiplying the inverse of the factor.

After we corrected the AP signals, we conducted the MCMC analysis to estimate the cosmological parameters. In Figure 5.12, we show the result of the parameter estimation. One can see that the estimated cosmological parameters are different from the fiducial values even though the correction factor is optimized to restore the theoretical curve with $\Omega = 0.3089$ and $w = -1$. We notice that the deviation in the estimated equation of state parameter from the fiducial value seems larger than that of matter density. We would like to note that this

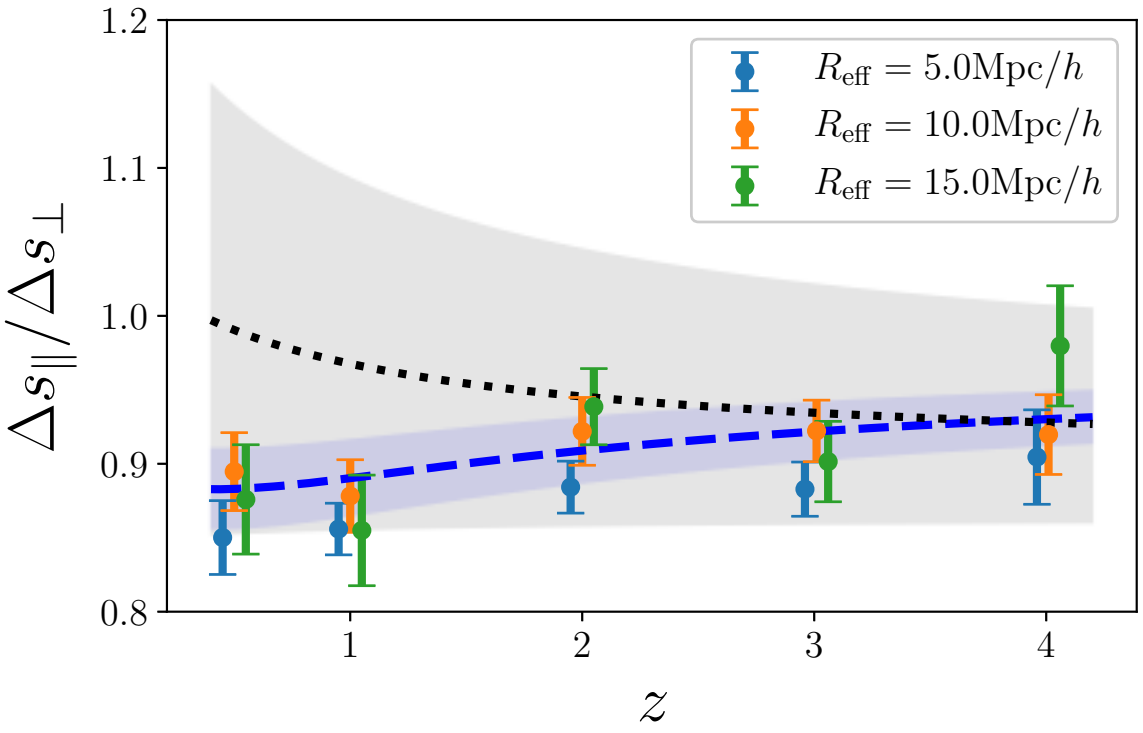

Figure 5.11: The ratio between sizes along and perpendicular to the line of sight direction including the effect of peculiar velocities of HI gas. The ratio of several radius of stacked voids are plotted from $z = 0.5$ to 4. Even though the shape of the stacked void is spherical without including the peculiar velocities, the RSD effect breaks the condition. The RSD effect appears as flattening of void shape along the line of sight. It seems that the flattening effect does not depend on the void radius but redshift. The blue dashed line indicates the theoretical model prediction, which is fitted to the data points in advance. The black dotted line is the result of the model fitting with the AP test at the same time.

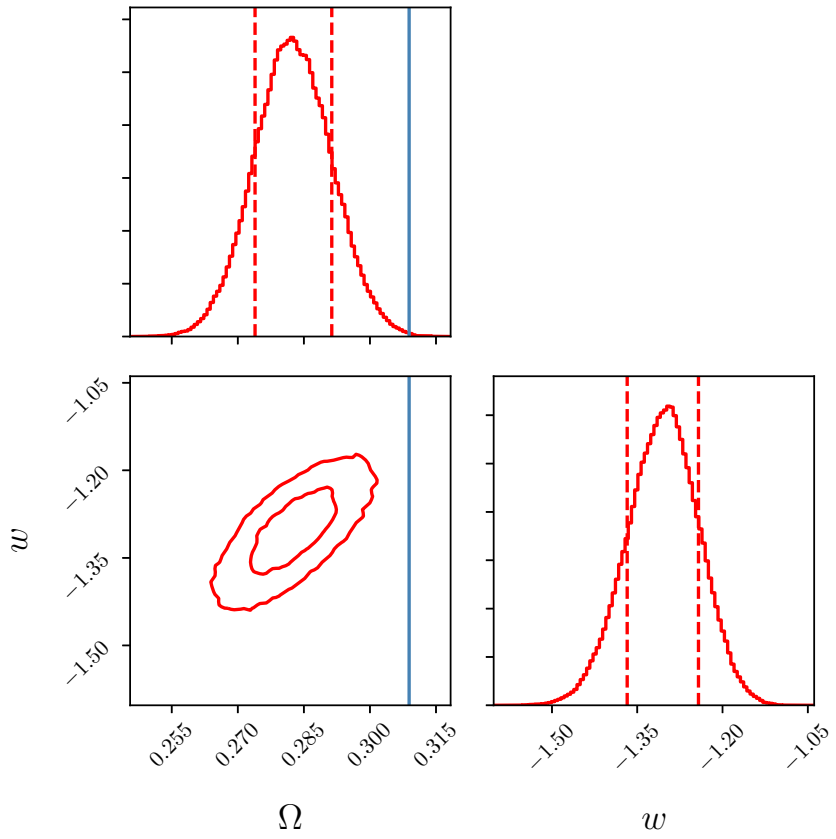

Figure 5.12: The same as Figure 5.9, but using corrected AP signals in redshift-space. The estimation of both the matter density and the equation of state parameter is inconsistent with the fiducial values.

result may be ambiguous since the accelerated expansion is more effective in the late epoch universe so that we need more samples at the late epoch to constrain w.

Although we have estimated the cosmological parameters after calculating the correction factors so far, the estimation is very dependent on the correction factors. In order to see the dependence on the estimation of the correction factors, we reanalyze the AP signals by adopting the correction factor to be a free parameter. So we conducted the MCMC estimation including the correction factor. In Figure 5.13, we show the results of the parameter estimation including the free correction factor which is represented as "offset" in the figure.

Even after we correct the AP signals, the parameter estimation seems to fail. This result indicates that the correction by the constant factor is not suitable for our analysis. We consider that this is because of the time evolution of the peculiar velocities of tracers. In fact,

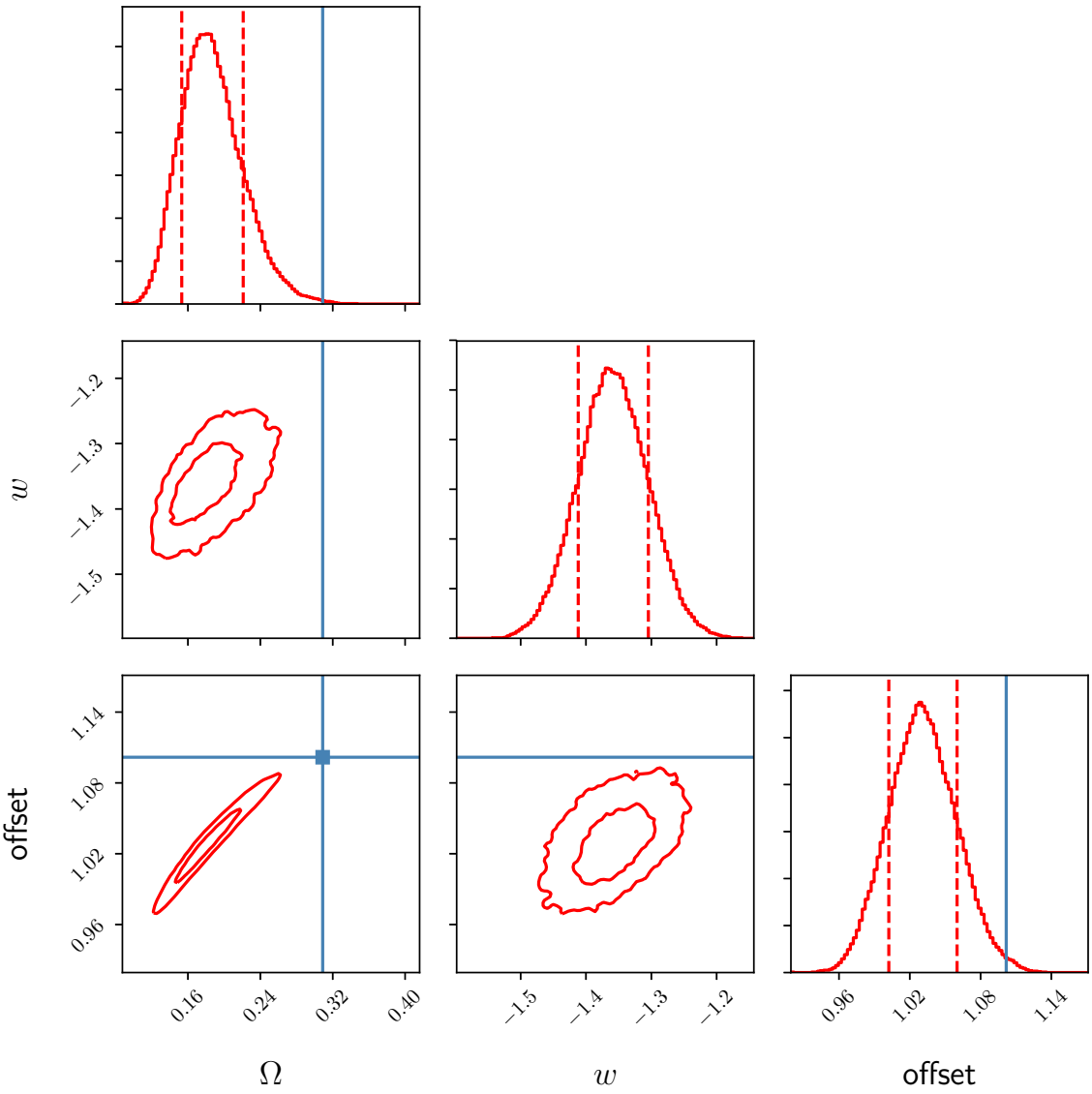

Figure 5.13: The parameter estimation by the AP signals with binned stacked voids in redshift-space. The dashed vertical lines indicate the 1σ confidence region while blue solid lines indicate the fiducial values of the parameters. For offset, we set the optimized value as the fiducial value. The difference between Figure 5.12 is that we estimate the correction factor as a free parameter at the same time. We can see that the matter density and correction factor are tightly degenerate each other.

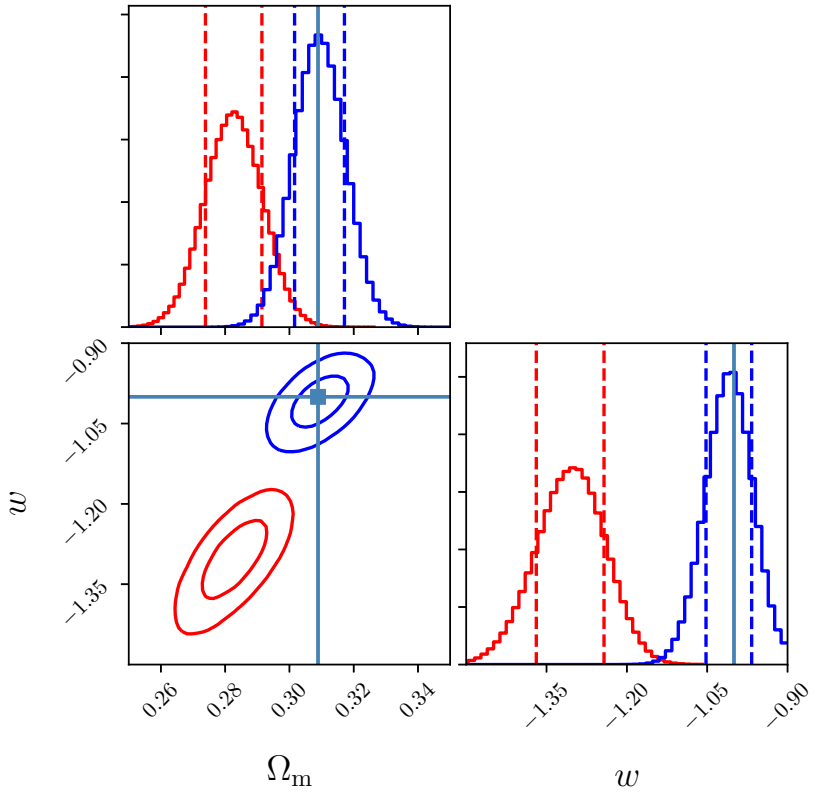

Figure 5.14: The parameter estimation with removing the RSD effect by the linear theory formula as indicated as blue lines. The red lines indicate the results by the constant fit as shown in Figure 5.12. We obtained $\Omega_{\rm m} = 0.3093^{+0.0076}_{-0.0077}$ and $w = -1.008^{+0.042}_{-0.044}$ after recovering the AP signals by the linear theory fit model.

the previous works analyze a narrow redshift range compared to our analysis so that the time evolution could not be seen in their results. Here we are going to take the time evolution of the peculiar velocity into account to remove the RSD effect properly.

The size ratio in redshift-space can be expressed as

$$\frac{\Delta s_{\parallel}^2}{\Delta s_{\perp}^2} = \frac{1}{\Delta x_{\perp}^2}\left[\langle \delta x_{\parallel}^2 \rangle + 2\frac{(1+z)\,\langle \delta x_{\parallel} \cdot v_{\rm p\parallel} \rangle}{H(z)} + \frac{(1+z)^2\,\langle v_{\rm p\parallel}^2 \rangle}{H(z)^2}\right]. \tag{5.5.4}$$

If the gas velocity is approximated to the dark matter velocity, the peculiar velocity can be

expressed by using the linear theory as

$$\boldsymbol{v}_{\rm p}(\boldsymbol{x}) = \frac{H(z)f(z)D(z)}{(1+z)} \int d^3x' \frac{\boldsymbol{x}-\boldsymbol{x}'}{|\boldsymbol{x}-\boldsymbol{x}'|^3}\delta(\boldsymbol{x}'), \tag{5.5.5}$$

where $D(z)$ is the growth factor defined in section 2.2.1, $f(z)$ is the growth rate defined as

$$f(a) \equiv \frac{d\ln D(a)}{d\ln a} = \frac{\dot{D}}{HD}. \tag{5.5.6}$$

In this case, the size ratio in redshift-space can be expressed as

$$\frac{\Delta s_{\parallel}}{\Delta s_{\perp}} = \alpha f(z)D(z) + \beta. \tag{5.5.7}$$

Thus, if the dynamics of the void tracer particle can be written by the linear theory and there is no velocity bias between the dark matter and the tracers, it is possible to forecast the RSD effect so that we can estimate the coefficients α and β analytically.

However, this trial does not work when we try to estimate the RSD effect only in the analytic way. This result indicates that even though the density fluctuation inside the void region is mild, the void ridge which makes the shape is composed high-density objects. Thus, there might be some non-linear effect in the void dynamics. And also, there should be velocity bias between the dark matter and the HI gas, so that it is a quite hard problem to estimate the RSD effect only by the theoretical way.

Then, we leave α and β as free parameters and we fitted them to describe the signals. As a result, we have obtained $\alpha = 0.1329^{+0.1830}_{-0.1409}$ and $\beta = 0.9016^{+0.0480}_{-0.0427}$. By using these values, we can reasonably describe the AP signals including the RSD effect as shown in Figure 5.11.

Then, we correct the AP signals by using the equation (5.5.7) and conduct the MCMC parameter estimation. We show the results in Figure 5.14. In the figure, we also show the parameter estimation results with the constant fit, which is indicated by the red lines. On the other hand, we show results with the linear theory fit by the blue lines. One can see that the correction by the linear theory fit seems to be a success so that we can recover the fiducial cosmological parameters as indicated by the solid vertical lines. In the linear fit case, we have obtained the cosmological parameters as $\Omega_{\rm m} = 0.3093^{+0.0076}_{-0.0077}$ and $w = -1.008^{+0.042}_{-0.044}$.

We note that as in the case of the constant fit, in the actual observation we do not know the true parameters α and β. To see the relationship between those parameters and the cosmological parameters, we have conducted the MCMC analysis including α and β at the

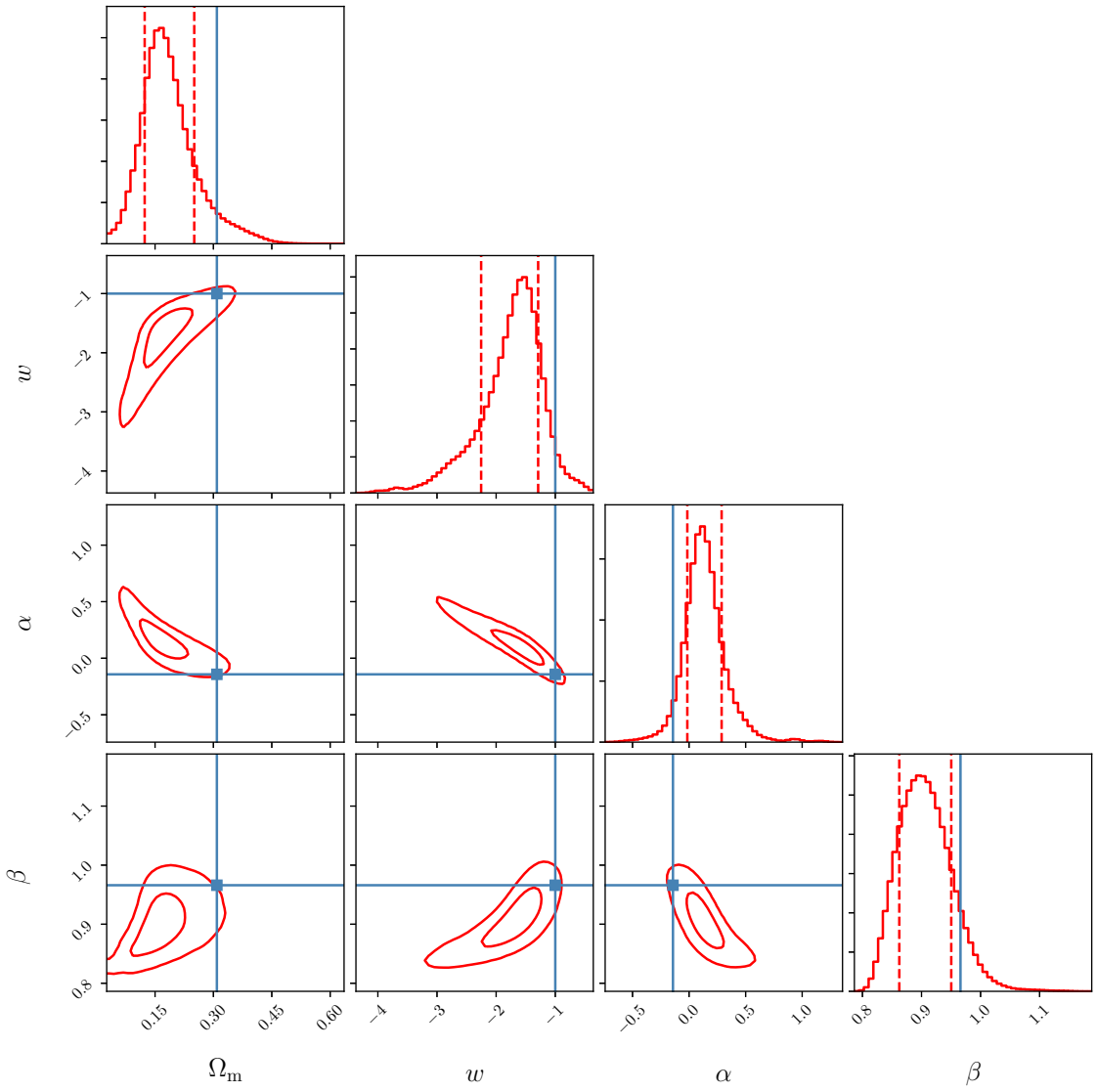

Figure 5.15: Same as Figure 5.14 but all the parameters are jointly fitted at the same time. We find that the RSD correction parameters and cosmological parameters are largely degenerate with each other. The estimated value for the cosmological parameters are biased; however, it is still consistent within 2σ. The best-fitting values are $\Omega_{\rm m} = 0.1723^{+0.0734}_{-0.0560}$, $w = -1.692^{+0.385}_{-0.663}$, $\alpha = 0.1329^{+0.1830}_{-0.1409}$, and $\beta = 0.9016^{+0.0480}_{-0.0427}$.

same time. In Figure 5.15, we show the parameter estimation results. We can see that each parameter largely degenerates and the preferable values are different from the fiducial values. For parameters α and β, we set the fiducial values as the one which has been obtained in the previous analysis. Even though the likely values are different from the fiducial values, the estimation is consistent with the values within 2-σ level.

Chapter 6

Conclusion

In this thesis, we have investigated the possibility of the application of the cosmic voids properties to the constraints on cosmological models. In terms of the void formation, we confirmed that void formation will be affected by the dark energy clustering if the void size is larger than the Jeans length of dark energy clustering which is determined by the speed of sound of dark energy fluid. To see the effect, we adopted the spherical void model and solving the evolution of the dark energy perturbations inside the void region. Even though the effect of dark energy clustering is sub percent level on each void formation, on a statistical property, namely size abundance, the effect is significant in which we confirmed that there are more than ten percent level deviations above the Jeans scale. The deviation can be found when the void size is larger than the Jeans scale. From this point of view, void size abundance can be one of the tools to distinguish the speed of sound of dark energy. However, the modification of the size abundance degenerates to the difference in the equation of state. So, in order to solve the degenerate, we need to determine the equation of state by the independent observations.

In addition to the possibility to distinguish the clustering nature of dark energy, we also study an application of void shape to constraint the cosmological models. The method is evolution model-free and it only demands either intrinsic or statistical isotropy of the observed objects, which is called the Alcock-Paczynski test. There have been some candidates to be proposed for the AP test. Among them, the averaged shape of voids has been paid attention to the test, since our observation region in the Universe is getting larger so that we can treat voids statistically. The averaged shape of voids is expected to be spherical even though each void shape is far from the sphericity. Thus it can be applied to the AP test. For now, there have been some studies that try to get the background energy budget of dark matter by combining the AP test and the shape of stacked void in galaxy surveys, but due to the shape noise, the constraints were weak.

In this study, we attempt to find voids in the HI distributions, which are also the biased

matter tracer and can be detected by the redshifted signals of the 21cm line. In order to trace the shape of voids in the intensity fields, we developed a method to identify the void region from the intensity fields by particle void finder, VIDE. In the process, we expand the concept of the void, in other words, we defined voids as low-intensity regions surrounded by the averaged intensity contour regions. We also assume that the shape of voids in our definition is expected to be spherical when they are averaged due to the cosmological principle.

We confirmed the sphericity of the stacked void surrounded by the intensity contour and that can be applied to constrain cosmological parameters such as matter density and the equation of state parameter of dark energy more precisely than the previous works with galaxy surveys. However, as is the case of galaxy surveys, the peculiar velocities of the gas along the line of sight distort the shape of voids systematically. So, if we do not remove the RSD effect properly, we misestimate the cosmological parameters.

Even though the previous works try to remove the RSD effect by multiplying a constant factor since the distortion does not seem to depend on the redshift, the procedure fails in our analysis. One of the reasons for the failure is that we analyze a wider redshift range. To introduce the time dependence of the RSD distortion, we adopt the idea of the cosmological linear perturbation theory. The theoretical model reasonably traces the shape distortion due to the peculiar velocities if the calibration of model parameters is conducted in advance. We confirmed that the RSD effect degenerates with the cosmological parameters estimation especially.

According to our study, we have shown that the void size property is very sensitive to the clustering nature of dark energy and the averaged void shape can be used to constrain the cosmological parameters such as Ω and w through the expansion history of the Universe. These results suggest that the cosmic voids can become one of the important observation targets although we have paid attention to bright or matter clustering regions. Thus, we conclude that voids are essential observable in order to know our Universe more precisely.

Appendix A

Derivation of the halo mass function from a random walk model

Here we solve the diffusion equation appearing in Section 2.3.2

$$\frac{\partial \Pi(\delta, S)}{\partial S} = \frac{1}{2}\frac{\partial \Pi(\delta, S)}{\partial^2 \delta} \tag{A.0.1}$$

as the one barrier problem for the halo formation or the two barriers problem for void formation by the same manner of Zentner (2007) The diffusion equation often appears in a thermo dynamics in which the coefficient in the right hand side is called heat conduction coefficient. For the halo formation case we will use the Fourier transform method while for void formation case we will use the valuable separation method.

A.1 Single barrier problem

Now we consider the random walk trajectory of δ at scale S. The condition of the trajectory is that the trajectory has never reached a threshold value δ_c. This condition implies the boundary condition $\Pi(\delta_c, S) = 0$ and we set the initial condition as $\Pi(\delta, S_0) = \delta_D(\delta - \delta_0)$. The initial condition comes from the fact that the trajectory starts only the point (δ_0, S_0) Now, we change valuable from δ to $\gamma = \delta_c - \delta$ such that $\Pi(\gamma = 0, S) = 0$ for the boundary condition and $\Pi(\gamma, S_0) = \delta_D(\gamma - \gamma_0)$ for the initial condition. The Fourier transform of the $\Pi(\gamma, S)$ is

$$\Pi(\gamma, S) = \frac{1}{\pi}\int_0^\infty A(k, S)\cos(k\gamma)dk + \frac{1}{\pi}\int_0^\infty B(k, S)\sin(k\gamma)dk \tag{A.1.1}$$

where the coefficients $A(k,S)$ and $B(k,S)$ are determined the inverse Fourier transform,

$$A(k,S) = \int_{-\infty}^{\infty} \Pi(\gamma,S)\cos(k\gamma)d\gamma, \qquad B(k,S) = \int_{-\infty}^{\infty} \Pi(\gamma,S)\sin(k\gamma)d\gamma. \tag{A.1.2}$$

The boundary condition $\Pi(0,S) = 0$ demands

$$\Pi(0,S) = \frac{1}{\pi}\int_0^{\infty} A(k,S)dk = 0, \tag{A.1.3}$$

thus we know $A(k,S) = 0$. Then, the diffusion equation can be written

$$\frac{\partial B(k,S)}{\partial S} = -\frac{k^2}{2}B(k,S). \tag{A.1.4}$$

The solution of the above equation is

$$B(k,S) = C(k)\exp\left(-\frac{k^2}{2}S\right), \tag{A.1.5}$$

so that we obtain

$$\Pi(\gamma,S) = \frac{1}{\pi}\int_0^{\infty} C(k)\sin(k\gamma)\exp\left(-\frac{k^2}{2}S\right)dk. \tag{A.1.6}$$

Since the Fourier transform of Π is written by only sine functions, its inverse Fourier transform should be,

$$C(k)\exp\left(-\frac{k^2}{2}S\right) = 2\int_0^{\infty} \Pi(\gamma,S)\sin(k\gamma)d\gamma \tag{A.1.7}$$

Now using the initial condition,

$$\begin{aligned} C(k)\exp\left(-\frac{k^2}{2}S_0\right) &= 2\int_0^{\infty} \Pi(\gamma,S_0)\sin(k\gamma)d\gamma \\ &= 2\int_0^{\infty} \delta_D(\gamma-\gamma_0)\sin(k\gamma)d\gamma \\ &= 2\sin(k\gamma_0) \end{aligned} \tag{A.1.8}$$

Thus,

$$C(k) = 2\sin(k\gamma_0)\exp\left(\frac{S_0}{2}k^2\right), \tag{A.1.9}$$

and

$$\begin{aligned}\Pi(\gamma, S) &= \frac{2}{\pi}\int_0^\infty \sin(k\gamma_0)\sin(k\gamma)\exp\left(-\frac{(S-S_0)}{2}k^2\right)dk \\ &= \frac{1}{\pi}\int_0^\infty \left[\cos(k(\gamma-\gamma_0)) - \cos(k(\gamma+\gamma_0))\right]\exp\left[-\frac{(S-S_0)}{2}k^2\right]dk. \end{aligned} \tag{A.1.10}$$

The integral in the right hand side finally results in

$$\Pi(\delta, S) = \frac{1}{\sqrt{2\pi(S-S_0)}}\left[\exp\left(-\frac{(\delta-\delta_0)^2}{2(S-S_0)}\right) - \exp\left(-\frac{[2(\delta_c-\delta_0)-(\delta-\delta_0)]^2}{2(S-S_0)}\right)\right] \tag{A.1.11}$$

where we use a formula

$$\int_0^\infty \cos(ax)e^{-bx^2}dx = \frac{1}{2}\sqrt{\frac{\pi}{b}}\exp\left(-\frac{a^2}{4b}\right), \qquad (b>0). \tag{A.1.12}$$

By setting the initial condition (δ_0, S_0) to $(0,0)$ we obtain

$$\Pi(\delta, S) = \frac{1}{\sqrt{2\pi S}}\left[\exp\left(-\frac{\delta^2}{2S}\right) - \exp\left(-\frac{[\delta-2\delta_c]^2}{2S}\right)\right] \tag{A.1.13}$$

This is the probability distribution of the trajectory which reaches (δ, S) without crossing δ_c earlier.

A.2 Double barrier problem

The next one is the case for the formation of the low density regions. The required condition for the trajectory is that it has never reached both δ_c and δ_v which is the criteria of the void formation. It is analogous to the Press-Schechter case that the boundary conditions are $\Pi(\delta_v, S) = \Pi(\delta_c, S) = 0$. We again change the valuable as $\gamma = \delta - \delta_v$, so that $\Pi(\gamma = 0, S) = \Pi(\gamma_c = \delta_c - \delta_v, S) = 0$ and $\Pi(\gamma, S_0) = \delta_D(\gamma - \gamma_0)$. To solve the diffusion equation as a two barriers problem, we adopt the valuable separation method this time.

We assume $\Pi(\gamma, S) = G(\gamma)P(S)$ and then the boundary conditions imply

$$G(0)P(S) = 0, \qquad G(\gamma_c)P(S) = 0. \tag{A.2.1}$$

If $P(S) = 0$, it is nothing to do with the random walk model. Therefore the boundary conditions indicate $P(S) \neq 0$ and $G(0) = G(\gamma_c) = 0$.

The diffusion equation (A.0.1) is

$$\frac{1}{P}\frac{dP}{dS} = \frac{1}{2G}\frac{d^2G}{d\gamma^2} = \kappa \tag{A.2.2}$$

where κ is some constant. It is straightforward to derive $P(S) \propto \exp(\kappa S)$. Even though κ can be any constant, because of our interests, κ should be $\kappa < 0$. For example, when $\kappa = 0$, the general solution of $G(\gamma)$ is $G(\Gamma) = a\gamma + b$. For this solution, the boundary conditions demand $a, b = 0$. The other case is when $\kappa > 0$. The general solution is $G(\gamma) = A\exp(k\gamma) + B\exp(-k\gamma)$ and the boundary conditions tell us $A = B = 0$ as well.

Hereafter we consider $\kappa = -k^2 < 0$. The general solution is then,

$$G(\gamma) = A\cos(\sqrt{2}k\gamma) + B\sin(\sqrt{2}k\gamma). \tag{A.2.3}$$

The boundary condition of $G(0) = 0$ indicates $A = 0$ Furthermore $G(\gamma)$ satisfies $G(\gamma_c) = 0$, so that $\sqrt{2}k = n\pi/\gamma_c$, where $n = 1, 2, 3, ...$ Therefore,the general solution of $G(\gamma)$ is written as

$$G(\gamma) = \sum_{n=1}^{\infty} C_n \sin\left(\frac{n\pi}{\gamma_c}\gamma\right) \tag{A.2.4}$$

where C_n are some constants Then the general expression of $\Pi(\gamma, S)$ is,

$$\Pi(\gamma, S) = \sum_{n=1}^{\infty} C_n \sin\left(\frac{n\pi}{\gamma_c}\gamma\right) \exp\left(-\frac{n^2\pi^2}{2\gamma_c^2}S\right) \tag{A.2.5}$$

The final step is to determine the coefficient C_n. Recalling the initial condition $S_0 = 0$,

$$\Pi(\gamma, 0) = \sum_{n=1}^{\infty} \sin\left(\frac{n\pi}{\gamma_c}\gamma\right) = \delta_D(\gamma - \gamma_0). \tag{A.2.6}$$

By the orthogonal relationship,

$$\int_0^L \sin\left(\frac{n\pi}{L}x\right)\sin\left(\frac{m\pi}{L}x\right) = \begin{cases} \frac{L}{2} & (n=m) \\ 0 & (n\neq m) \end{cases} \tag{A.2.7}$$

we multiply (A.2.6) by $\sin(m\pi\gamma/\gamma_c)$ and integration of it from $\gamma_0 - \gamma_c/2$ to $\gamma_0 + \gamma_c/2$ results in

$$C_n = \frac{2}{\gamma_c}\sin\left(\frac{n\pi}{\gamma_c}\gamma_0\right). \tag{A.2.8}$$

Thus the general solution of $\Pi(\gamma, S)$ with two barriers is

$$\Pi(\gamma, S) = \sum_{n=1}^{\infty}\frac{2}{\gamma_c}\sin\left(\frac{n\pi}{\gamma_c}\gamma_0\right)\sin\left(\frac{n\pi}{\gamma_c}\gamma\right)\exp\left(-\frac{n^2\pi^2}{2\gamma_c^2}S\right). \tag{A.2.9}$$

Finally we recover γ to δ,

$$\Pi(\delta, S) = \sum_{n=1}^{\infty}\frac{2}{(\delta_c-\delta_v)}\sin\left(\frac{n\pi}{(\delta_c-\delta_v)}(\delta_0-\delta_v)\right)\sin\left(\frac{n\pi}{(\delta_c-\delta_v)}(\delta-\delta_v)\right)\exp\left(-\frac{n^2\pi^2}{2(\delta_c-\delta_v)^2}S\right). \tag{A.2.10}$$

Appendix B

Resolution effect

Even though we revealed that the AP test in the HI intensity contour with stacked void technique has a huge potential to put a tight constraint on cosmological models in principle, our simulation setup has been a very simplified and idealized one. Here, we are going to evaluate the feasibility of the AP test by assuming future SKA observation detectabilities.

One of the biggest concerns is whether we can detect the fluctuation in the intensity field. In the previous analysis, we detect void shape by setting a threshold that corresponds to the spatially averaged brightness temperature. Our concern is that whether we can trace the void shape by the threshold. In order to outline the void shape by the average threshold, we need to detect intensities at least less than the average intensity otherwise the noise will overcome the intensity field and we cannot trace the HI structures. Here we consider only the instrumental noise. The noise amplitude can be determined by the angular and redshift resolution as well as the observation time. Assuming the SKA observation, such noise amplitude can be estimated as (Furlanetto et al., 2006; Horii et al., 2017)

$$\delta T_{\rm noise} \approx 264 \left(\frac{1'}{\delta\theta}\right)^2 \left(\frac{\rm MHz}{\Delta\nu}\frac{\rm 100h}{t_{\rm obs}}\right)^{1/2} \left(\frac{1+z}{1}\right) \ \mu{\rm K}. \tag{B.0.1}$$

By assuming the observation time to be $t_{\rm obs} = 1000$h and the resolution in the previous sections produce the noise amplitude as the left panel in Figure B.1. As shown in the panel, our previous situation can be achievable only for $z = 0.5$. For higher redshifts, the averaged signals are below the noise temperature. In order to solve this situation, we need to vary the threshold value to trace the shape of voids or observe the intensity field with lower resolution or take both procedures. The right panel in Figure B.1 shows the noise level when we fix the angular resolution which corresponds to 2 arcmins as well as setting the frequency resolution to correspond to the angular scale. In this case, the averaged signal can be detectable until

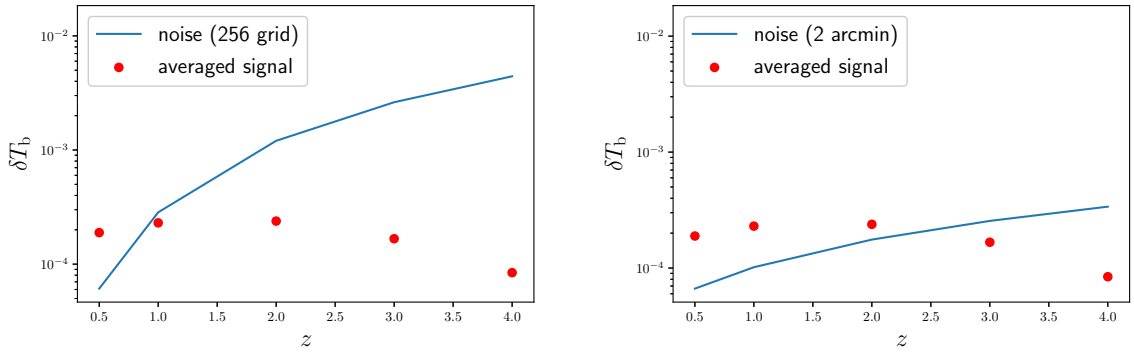

Figure B.1: Signal and noise of the brightness temperatures. For the fixed resolution of our idealized analysis, the signals are beneath the noise amplitude at $z > 1.0$. If the observation is conducted with a lower resolution, the signal can be detectable. For the right panel, we assume the angular resolution to be 2 arcmins.

$z = 2.0$. For higher redshifts, we can trace the void shape by modifying the threshold into 10 times larger the averaged value. We then make intensity maps with the 2 arcmin resolution and make mock particle distributions in both real-space and redshift-space by setting the the threshold to be the averaged brightness temperature until $z = 2.0$ and for higher redshifts than $z = 2.0$ setting the threshold to be ten times larger value. However, we cannot find enough voids for stacking at $z = 3$ and 4 since the structures are too smoothed and the mock particles are too discrete to trace the void structures of the scale we have focused on. Thus we simulate the AP signals until $z = 2.0$ and add additional redshift data at $z = 0.3$ and 1.5 so that the number of data in terms of redshift is the same. We note that when we make the intensity map at $z \leq 0.5$ we fixed the number of grids as 256^3 to reduce the calculation time and the memory. This resolution is rougher than the even 2 arcmin resolution at the redshifts. In this analysis, we have stacked all voids within the radius range by normalizing the relative position of the particles from the center of voids.

In Figure B.2 we show the AP signals for this setup.

The figure shows that the AP signals in real-space keep unity which indicates that the sphericity of voids is maintained in the relatively low resolution compared to the previous analysis. On the other hand, we notice that the AP signals in redshift-space getting close to unity at higher redshifts ($1.0 \leq z$) while at low redshifts they show the systematic deviation as we have already observed. The reason we consider is that for higher redshifts the position shift of the gas sells along the line of sight in redshift-space could not be resolved due to the low resolution at higher redshifts. In this setup, the resolution scales are $1.339, 1.767$, and 2.095 Mpc/h at $z = 1.0, 1.5$ and 2.0 respectively. We analyze the peculiar velocities of

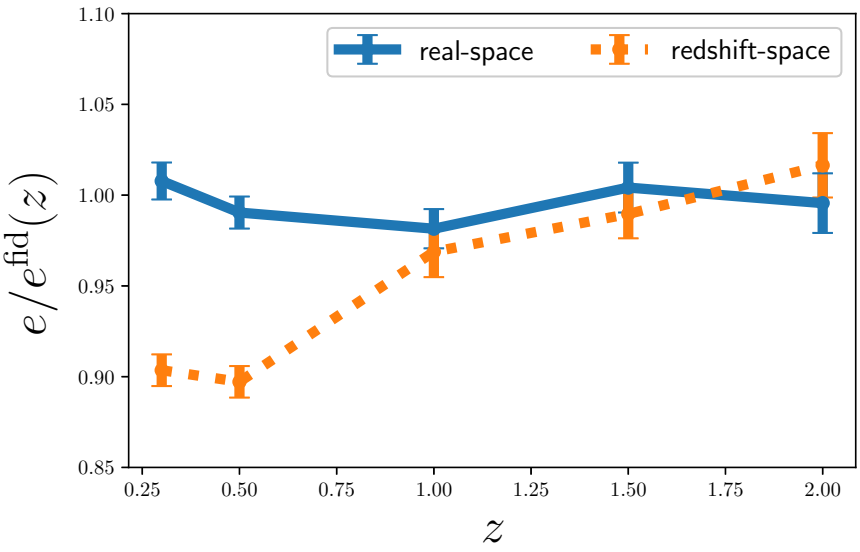

Figure B.2: The normalized AP signals by the fiducial values for 2 arcmin resolution in both real-space and redshift-space. Here we have stacked all voids within the radius range we have focused on. The AP signals in real-space seems to keep unity for the redshifts while the signals in redshift-space are close to unity at $1.0 \leq z$ and getting close to 0.9 at $z = 0.5$ and 0.3.

the gas cells in the simulation and obtain their velocity dispersions along the line of sight as $\sigma_{v\parallel} = 242.7, 222.9$ and 205.2 kms^{-1} for the redshifts, from which we expect the position shifts are $2.730, 2.374$ and 2.047 Mpc$/h$ respectively. These shift scales are close to the resolution scales so that the position shifts have not been resolved and we could not detect the systematic distortions.

Since it seems to be difficult to remove the RSD effect with the low resolution set up, we perform the AP test only for the real-space data set. In Figure B.3 we show the results of the MCMC parameter estimation. One can notice that the estimations are very close to the 1σ confidence region, especially for w the most preferable value is almost the fiducial value. This is because we include the low redshift point ($z = 0.3$) in the analysis. So this result suggests that it is important to observe the low redshift data to confirm the deviation in the equation of state parameter of dark energy from -1. Also, this result suggests that even with the low resolution, we can estimate the cosmological parameters by the stacked void shapes if we can remove the effect of the peculiar velocities in principle. The estimations are $\Omega = 0.2957^{+0.0124}_{-0.0122}$ and $w = -1.016^{+0.074}_{-0.076}$.

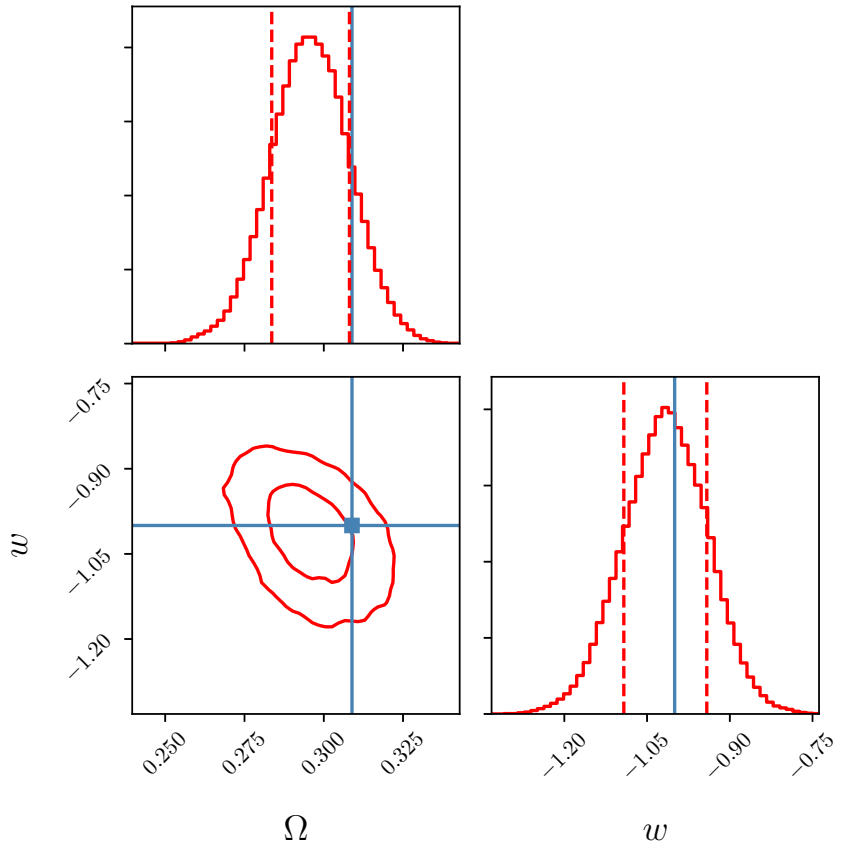

Figure B.3: The parameter estimation with the stacked voids found in the intensity maps with 2 arcmin resolution. Here we stack all voids in the radius range. In this analysis, we do not include the effect of the peculiar velocities. Even with the low resolution, we can reasonably estimate the parameters. The results are $\Omega = 0.2957^{+0.0124}_{-0.0122}$ and $w = -1.016^{+0.074}_{-0.076}$

Acknowledgement

I would like to give my gratitude to all people who support my life as a researcher, especially Professor Naoshi SUGIYAMA, Takahiko MATSUBARA, Kiyotomo ICHIKI Hiroyuki TASHIRO and Atushi J. NISHIZAWA, who have been directly guided my research interests. As well as those people, I thank all people with whom I spent in the cosmology group for 6 years, Shuichiro YOKOYAMA, Sachiko KUROYANAGI, Kenji HASEGAWA, Hironao MIYATAKE, Takeshi KOBAYASHI, YUKO URAKAWA, Naoya KITAJIMA, Atsushi NISHIZAWA, Jean-Baptiste DURRIVE, Chiaki HIKAGE and Daisuke NITTA. I also express my gratefulness to my students in the cosmology group, especially my colleagues Shun ARAI, Yuka MATSUI and Toshihiro HORII since owing to them I have been helped many times when I am in difficulties. Finally, I appreciate my family and Mongolkhatan OYUNCHIMEG for their kind attention and a lot of supports to me.

Bibliography

Abazajian K. N. et al., The Seventh Data Release of the Sloan Digital Sky Survey, 2009, ApJS, 182, 543

Abramo L. R., Batista R. C., Liberato L., Rosenfeld R., Structure formation in the presence of dark energy perturbations, 2007, JCAP, 11, 012

Adams J. J. et al., The HETDEX Pilot Survey. I. Survey Design, Performance, and Catalog of Emission-line Galaxies, 2011, ApJS, 192, 5

Ahn C. P. et al., The Tenth Data Release of the Sloan Digital Sky Survey: First Spectroscopic Data from the SDSS-III Apache Point Observatory Galactic Evolution Experiment, 2014, ApJS, 211, 17

Alam S. et al., The Eleventh and Twelfth Data Releases of the Sloan Digital Sky Survey: Final Data from SDSS-III, 2015, ApJS, 219, 12

Alcock C., Paczynski B., An evolution free test for non-zero cosmological constant, 1979, Nature, 281, 358

Allison A. C., Dalgarno A., Spin Change in Collisions of Hydrogen Atoms, 1969, ApJ, 158, 423

Basse T., Eggers Bjælde O., Wong Y. Y. Y., Spherical collapse of dark energy with an arbitrary sound speed, 2011, JCAP, 10, 038

Bennett C. L. et al., First-Year Wilkinson Microwave Anisotropy Probe (WMAP) Observations: Preliminary Maps and Basic Results, 2003, ApJS, 148, 1

Beutler F. et al., The 6dF Galaxy Survey: baryon acoustic oscillations and the local Hubble constant, 2011, MNRAS, 416, 3017

Bharadwaj S., Nath B. B., Sethi S. K., Using HI to Probe Large Scale Structures at z ~3, 2001, Journal of Astrophysics and Astronomy, 22, 21

Biswas R., Alizadeh E., Wandelt B. D., Voids as a precision probe of dark energy, 2010, Phys. Rev. D, 82, 023002

Blanton M. R. et al., New York University Value-Added Galaxy Catalog: A Galaxy Catalog Based on New Public Surveys, 2005, AJ, 129, 2562

Blumenthal G. R., da Costa L. N., Goldwirth D. S., Lecar M., Piran T., The largest possible voids, 1992, ApJ, 388, 234

Bond J. R., Cole S., Efstathiou G., Kaiser N., Excursion set mass functions for hierarchical Gaussian fluctuations, 1991, ApJ, 379, 440

Bos E. G. P., van de Weygaert R., Dolag K., Pettorino V., The darkness that shaped the void: dark energy and cosmic voids, 2012, MNRAS, 426, 440

Chiba T., Sugiyama N., Nakamura T., Observational tests of x-matter models, 1998, MNRAS, 301, 72

Clampitt J., Cai Y.-C., Li B., Voids in modified gravity: excursion set predictions, 2013, MNRAS, 431, 749

Colless M., First results from the 2dF Galaxy Redshift Survey., 1998, Anglo-Australian Observatory Epping Newsletter, 85, 4

Cuesta A. J. et al., The clustering of galaxies in the SDSS-III Baryon Oscillation Spectroscopic Survey: baryon acoustic oscillations in the correlation function of LOWZ and CMASS galaxies in Data Release 12, 2016, MNRAS, 457, 1770

Dawson K. S. et al., The Baryon Oscillation Spectroscopic Survey of SDSS-III, 2013, AJ, 145, 10

de Lapparent V., Geller M. J., Huchra J. P., A slice of the universe, 1986, ApJL, 302, L1

DESI Collaboration et al., The DESI Experiment Part I: Science,Targeting, and Survey Design, 2016, arXiv e-prints, arXiv:1611.00036

Eisenstein D., 2015, in APS Meeting Abstracts, Vol. 2015, APS April Meeting Abstracts, p. Z2.001

Eisenstein D. J., Hu W., Baryonic Features in the Matter Transfer Function, 1998, ApJ, 496, 605

Eisenstein D. J. et al., Detection of the Baryon Acoustic Peak in the Large-Scale Correlation Function of SDSS Luminous Red Galaxies, 2005, ApJ, 633, 560

Endo T., Nishizawa A. J., Ichiki K., Effect of dark energy perturbation on cosmic voids formation, 2018, MNRAS, 478, 5230

Field G. B., Excitation of the Hydrogen 21-CM Line, 1958, Proceedings of the IRE, 46, 240

Foreman-Mackey D., Hogg D. W., Lang D., Goodman J., emcee: The MCMC Hammer, 2013, PASP, 125, 306

Furlanetto S. R., Oh S. P., Briggs F. H., Cosmology at low frequencies: The 21 cm transition and the high-redshift Universe, 2006, Phys.Rep., 433, 181

Geller M. J., Huchra J. P., de Lapparent V., 1987, in IAU Symposium, Vol. 124, Observational Cosmology, Hewitt A., Burbidge G., Fang L. Z., eds., pp. 301–312

Gregory S. A., Thompson L. A., The Coma/A1367 supercluster and its environs, 1978, ApJ, 222, 784

Groth E. J., Peebles P. J. E., Statistical analysis of catalogs of extragalactic objects. VII. Two- and three-point correlation functions for the high-resolution Shane-Wirtanen catalog of galaxies., 1977, ApJ, 217, 385

Hamaus N., Pisani A., Sutter P. M., Lavaux G., Escoffier S., Wandelt B. D., Weller J., Constraints on Cosmology and Gravity from the Dynamics of Voids, 2016, Physical Review Letters, 117, 091302

Horii T., Asaba S., Hasegawa K., Tashiro H., Can HI 21-cm lines trace the missing baryons in the filamentary structures?, 2017, PASJ, 69, 73

Hu W., Sugiyama N., Small-Scale Cosmological Perturbations: an Analytic Approach, 1996, ApJ, 471, 542

Hubble E., A Relation between Distance and Radial Velocity among Extra-Galactic Nebulae, 1929, Proceedings of the National Academy of Science, 15, 168

Hubble E. P., Extragalactic nebulae., 1926, ApJ, 64, 321

Jõeveer M., Einasto J., Tago E., Spatial distribution of galaxies and of clusters of galaxies in the southern galactic hemisphere, 1978, MNRAS, 185, 357

Kaiser N., Clustering in real space and in redshift space, 1987, MNRAS, 227, 1

Komatsu E. et al., Seven-year Wilkinson Microwave Anisotropy Probe (WMAP) Observations: Cosmological Interpretation, 2011, ApJS, 192, 18

Kruk J., 2019, in American Astronomical Society Meeting Abstracts, Vol. 233, American Astronomical Society Meeting Abstracts #233, p. 171.07

Kuhlen M., Madau P., Montgomery R., The Spin Temperature and 21 cm Brightness of the Intergalactic Medium in the Pre-Reionization era, 2006, ApJL, 637, L1

Lavaux G., Wandelt B. D., Precision cosmology with voids: definition, methods, dynamics, 2010, MNRAS, 403, 1392

Lavaux G., Wandelt B. D., Precision Cosmography with Stacked Voids, 2012, ApJ, 754, 109

Lewis A., Challinor A., Lasenby A., Efficient Computation of Cosmic Microwave Background Anisotropies in Closed Friedmann-Robertson-Walker Models, 2000, ApJ, 538, 473

Lima J. A. S., Zanchin V., Brandenberger R., On the Newtonian cosmology equations with pressure, 1997, MNRAS, 291, L1

Liszt H., The spin temperature of warm interstellar H I, 2001, Astronomy & Astrophysics, 371, 698

Mao Q., Berlind A. A., Scherrer R. J., Neyrinck M. C., Scoccimarro R., Tinker J. L., McBride C. K., Schneider D. P., Cosmic Voids in the SDSS DR12 BOSS Galaxy Sample: The Alcock-Paczynski Test, 2017a, ApJ, 835, 160

Mao Q., Berlind A. A., Scherrer R. J., Neyrinck M. C., Scoccimarro R., Tinker J. L., McBride C. K., Schneider D. P., Cosmic Voids in the SDSS DR12 BOSS Galaxy Sample: The Alcock-Paczynski Test, 2017b, ApJ, 835, 160

Mao Q. et al., A Cosmic Void Catalog of SDSS DR12 BOSS Galaxies, 2017c, ApJ, 835, 161

Marinacci F. et al., First results from the IllustrisTNG simulations: radio haloes and magnetic fields, 2018, MNRAS, 480, 5113

Mesinger A., Furlanetto S., Cen R., 21CMFAST: a fast, seminumerical simulation of the high-redshift 21-cm signal, 2011, MNRAS, 411, 955

Naiman J. P. et al., First results from the IllustrisTNG simulations: a tale of two elements - chemical evolution of magnesium and europium, 2018, MNRAS, 477, 1206

Nelson D. et al., First results from the IllustrisTNG simulations: the galaxy colour bimodality, 2018, MNRAS, 475, 624

Nelson D. et al., The IllustrisTNG simulations: public data release, 2019, Computational Astrophysics and Cosmology, 6, 2

Neyrinck M. C., ZOBOV: a parameter-free void-finding algorithm, 2008, MNRAS, 386, 2101

Novosyadlyj B., Tsizh M., Kulinich Y., Evolution of density and velocity profiles of dark matter and dark energy in spherical voids, 2016, ArXiv e-prints

Park D., Lee J., Void Ellipticity Distribution as a Probe of Cosmology, 2007, Physical Review Letters, 98, 081301

Perlmutter S. et al., Measurements of Ω and Λ from 42 High-Redshift Supernovae, 1999, ApJ, 517, 565

Pillepich A. et al., First results from the IllustrisTNG simulations: the stellar mass content of groups and clusters of galaxies, 2018, MNRAS, 475, 648

Pisani A., Sutter P. M., Hamaus N., Alizadeh E., Biswas R., Wandelt B. D., Hirata C. M., Counting voids to probe dark energy, 2015, Phys. Rev. D, 92, 083531

Planck Collaboration et al., Planck 2018 results. VI. Cosmological parameters, 2018, ArXiv e-prints

Platen E., van de Weygaert R., Jones B. J. T., A cosmic watershed: the WVF void detection technique, 2007, MNRAS, 380, 551

Platen E., van de Weygaert R., Jones B. J. T., Alignment of voids in the cosmic web, 2008, MNRAS, 387, 128

Press W. H., Schechter P., Formation of Galaxies and Clusters of Galaxies by Self-Similar Gravitational Condensation, 1974, ApJ, 187, 425

Racca G. D. et al., 2016, Society of Photo-Optical Instrumentation Engineers (SPIE) Conference Series, Vol. 9904, The Euclid mission design, p. 99040O

Riess A. G. et al., Observational Evidence from Supernovae for an Accelerating Universe and a Cosmological Constant, 1998, AJ, 116, 1009

Ryden B. S., Measuring Q 0 from the Distortion of Voids in Redshift Space, 1995, ApJ, 452, 25

Sachs R. K., Wolfe A. M., Perturbations of a Cosmological Model and Angular Variations of the Microwave Background, 1967, ApJ, 147, 73

Santos M. et al., Cosmology from a SKA HI intensity mapping survey, 2015, Advancing Astrophysics with the Square Kilometre Array (AASKA14), 19

Scolnic D. M. et al., The Complete Light-curve Sample of Spectroscopically Confirmed SNe Ia from Pan-STARRS1 and Cosmological Constraints from the Combined Pantheon Sample, 2018, ApJ, 859, 101

Seldner M., Siebers B., Groth E. J., Peebles P. J. E., New reduction of the Lick catalog of galaxies, 1977, AJ, 82, 249

Sheth R. K., Tormen G., An excursion set model of hierarchical clustering: ellipsoidal collapse and the moving barrier, 2002, MNRAS, 329, 61

Sheth R. K., van de Weygaert R., A hierarchy of voids: much ado about nothing, 2004, MNRAS, 350, 517

Smith F. J., Hydrogen atom spin-change collisions, 1966, P&SS, 14, 929

Springel V. et al., First results from the IllustrisTNG simulations: matter and galaxy clustering, 2018, MNRAS, 475, 676

Square Kilometre Array Cosmology Science Working Group et al., Cosmology with Phase 1 of the Square Kilometre Array; Red Book 2018: Technical specifications and performance forecasts, 2018, arXiv e-prints, arXiv:1811.02743

Sutter P. M., Lavaux G., Wandelt B. D., Weinberg D. H., A First Application of the Alcock-Paczynski Test to Stacked Cosmic Voids, 2012a, ApJ, 761, 187

Sutter P. M., Lavaux G., Wandelt B. D., Weinberg D. H., A First Application of the Alcock-Paczynski Test to Stacked Cosmic Voids, 2012b, ApJ, 761, 187

Sutter P. M., Lavaux G., Wandelt B. D., Weinberg D. H., A Public Void Catalog from the SDSS DR7 Galaxy Redshift Surveys Based on the Watershed Transform, 2012c, ApJ, 761, 44

Sutter P. M., Pisani A., Wandelt B. D., Weinberg D. H., A measurement of the Alcock-Paczyński effect using cosmic voids in the SDSS, 2014, MNRAS, 443, 2983

Suzuki N. et al., The Hubble Space Telescope Cluster Supernova Survey. V. Improving the Dark-energy Constraints above z ¿ 1 and Building an Early-type-hosted Supernova Sample, 2012, ApJ, 746, 85

Tinker J., Kravtsov A. V., Klypin A., Abazajian K., Warren M., Yepes G., Gottlöber S., Holz D. E., Toward a Halo Mass Function for Precision Cosmology: The Limits of Universality, 2008, ApJ, 688, 709

Totsuji H., Kihara T., The Correlation Function for the Distribution of Galaxies, 1969, PASJ, 21, 221

van de Weygaert R., 2016, in IAU Symposium, Vol. 308, The Zeldovich Universe: Genesis and Growth of the Cosmic Web, van de Weygaert R., Shandarin S., Saar E., Einasto J., eds., pp. 493–523

van de Weygaert R., Schaap W., 2009, The Cosmic Web: Geometric Analysis, Martínez V. J., Saar E., Martínez-González E., Pons-Bordería M. J., eds., Vol. 665, pp. 291–413

Verza G., Pisani A., Carbone C., Hamaus N., Guzzo L., The Void Size Function in Dynamical Dark Energy Cosmologies, 2019, arXiv e-prints, arXiv:1906.00409

Weinberg D. H., Mortonson M. J., Eisenstein D. J., Hirata C., Riess A. G., Rozo E., Observational probes of cosmic acceleration, 2013, Phys.Rep., 530, 87

Wouthuysen S. A., On the excitation mechanism of the 21-cm (radio-frequency) interstellar hydrogen emission line., 1952, AJ, 57, 31

Yoo J., Watanabe Y., Theoretical Models of Dark Energy, 2012, International Journal of Modern Physics D, 21, 1230002

York D. G. et al., The Sloan Digital Sky Survey: Technical Summary, 2000, AJ, 120, 1579

Zentner A. R., The Excursion Set Theory of Halo Mass Functions, Halo Clustering, and Halo Growth, 2007, International Journal of Modern Physics D, 16, 763

Zivick P., Sutter P. M., 2016, in IAU Symposium, Vol. 308, The Zeldovich Universe: Genesis and Growth of the Cosmic Web, van de Weygaert R., Shandarin S., Saar E., Einasto J., eds., pp. 589–590

Zygelman B., Hyperfine Level-changing Collisions of Hydrogen Atoms and Tomography of the Dark Age Universe, 2005, ApJ, 622, 1356